Spring 2018

Synthesis of Metal Oxide Nanoparticles and Mesocrystals in an Interphase Droplet Reactor

Brian Zukas
University of New Hampshire, Durham

SYNTHESIS OF METAL OXIDE NANOPARTICLES AND MESOCRYSTALS IN AN INTERPHASE DROPLET REACTOR

BY

BRIAN G. ZUKAS

B.S. Chemical Engineering, University of New Hampshire, 2012

M.S. Chemical Engineering, University of New Hampshire, 2014

DISSERTATION

Submitted to the University of New Hampshire

in Partial Fulfillment of

the Requirements for the Degree of

Doctor of Philosophy

in

Chemical Engineering

May, 2018

This dissertation has been examined and approved in partial fulfillment of the requirements for the degree of Doctor of Philosophy in Chemical Engineering by:

Dissertation Director, Nivedita Gupta, Professor of Chemical Engineering

Dale P. Barkey, Professor of Chemical Engineering

Xiaowei Teng, Associate Professor of Chemical Engineering

Nan Yi, Assistant Professor of Chemical Engineering

Gonghu Li, Associate Professor of Chemistry

On April 4, 2018

Original approval signatures are on file with the University of New Hampshire Graduate School.

Acknowledgments

I would like to thank my advisor, Dr. Gupta, for all her help and guidance during my time as her graduate student. Your commitment to my success and the care you display has been unwavering since I first worked in your lab my sophomore year. I have truly appreciated this opportunity to be your graduate student. I would also like to thank the members of my dissertation committee, Dr. Dale Barkey, Dr. Xiaowei Teng, Dr. Nan Yi, and Dr. Gonghu Li for giving their time to serve on my committee.

I greatly appreciated the help that Ana Lidia Dos Santos, Jessica Lindes Foncesca, Kate Estep, and Chris Reilly provided during my research. I would also like to thank Dan Charles for the many helpful conversations we had.

I would like to thank Nancy Cherim at the University Instrumentation Center for her assistance with the use of the SEM and with the EDS measurements. I would also like to thank Dr. James Krzanowski of UNH and Dr. Shao-Liang Zheng of the Harvard X-ray Laboratory for their assistance with XRD data collection.

I would especially like thank my wife, Annie, for her continuous support during my time in graduate school. Your never flagging encouragement, understanding of the weekends spent working and the late nights in the lab have been invaluable to me.

I would also like to acknowledge the financial support of the 2017 UNH Summer Teaching Assistant Fellowship.

Table of Contents

List of Figures

List of Tables

ABSTRACT

SYNTHESIS OF METAL OXIDE NANOPARTICLES AND MESOSCRYSTALS IN AN INTERPHASE DROPLET REACTOR

By Brian G. Zukas

University of New Hampshire, May 2018

The attractive properties of nanoparticles and nanostructures has driven their integration into a wide range of modern technologies. Synthesis of nanoparticles in droplet flow reactors offers a solution to the shortcomings of batch reactors. The interphase droplet reactor presented in this work maintains the advantages of a droplet flow reactor while accomplishing reagent addition through mass transfer from the continuous phase to the droplet phase. In this work, sodium hydroxide in a continuous phase of 1-octanol diffuses into aqueous droplets containing a metal salt, initiating nanoparticle synthesis. An acid-base titration confirmed that increasing the total flow rate increased the rate of mass transfer. Addition of Triton X-100 surfactant increased the rate of mass transfer while sodium dodecyl sulfate did not. Zinc oxide nanoparticles with controllable sizes between 41 to 62 nm were produced by changing reaction temperature, reagent concentration, droplet volume, and adding surfactants. Operating the interphase droplet reactor at 25˚C produced large ZnO sheets and increasing the reaction temperature to 40˚C and above produced spherical nanoparticles. Higher inlet sodium hydroxide concentrations transitioned the particle morphology from spherical particles to plates. Decreasing the reactor diameter decreased the mean particle size from 54 nm to 43 nm. The interphase droplet reactor also produced a narrower particle size distribution than a single phase aqueous batch reactor. Low reagent concentrations produced ellipsoidal zinc oxide mesocrystals through oriented attachment. A reaction temperature of 40˚C

was adequate for mesocrystal production. The presence of Triton X-100 did not prevent oriented attachment while the addition of sodium dodecyl sulfate did. The ability of the interphase droplet reactor to synthesize other metal oxides was demonstrated by the synthesis of copper (II) oxide. Copper oxide sheet mesocrystals were formed in the absence of acetic acid. The presence of acetic acid in the droplet phase inhibited oriented attachment and produced copper oxide nanowires.

Chapter 1: Introduction

The incorporation of nanoparticles into many aspects of modern technology has been driven by the unique properties nanoscale materials possess. When compared to a bulk material, nanoparticles of the same material can show enhanced catalytic, anti-microbial, electronic, hardness, and magnetic properties [143]. Nanoparticles also offer an ease of processing that bulk materials often do not, such as easy dispersion or colloidal stability [28]. These properties make nanoparticles ideal for improving existing technology and necessary for emerging technology.

In the medical field, nanoparticles have been applied to challenging issues in drug delivery and treatment of diseases such as cancer. Drug delivery is used to overcome solubility, uptake, or stability issues of a desired drug [24]. This can be accomplished by binding drug molecules directly to the surface of a nanoparticle. The hydrophobicity of a drug can be decreased by binding the hydrophobic tail to the nanoparticle surface, leaving a more hydrophilic head exposed to the biological environment [34]. Nanoparticles can also enhance drug uptake by the ability of nanoparticles to penetrate biological barriers such as the skin [110]. Cellular uptake of nanoparticles can be promoted through surface modification as well [56]. As well as being carriers for drugs, nanoparticles themselves can be used as a treatment. Gold nanoparticles can be modified to promote uptake into tumors. Once the nanoparticles have accumulated in the tumor, exposure to near-infrared light causes the nanoparticles to generate heat, locally killing tumor cells [47].

Nanoparticles have been used in electronic applications from LEDs and photodetectors to solar cell components [149]. The material properties that make nanoparticles ideal for these applications, such as band gap or emission spectrum, can be tuned by changing particle size and

morphology [121]. Performance of electronic devices such as solar cells and electrochemical sensors is enhanced by the rapid electron transfer observed in nanoparticles [50]. Mesocrystals formed from ordered assemblies of nanoparticles can allow for better electron transfer than unstructured nanoparticle deposits due to the increase in passages available in the mesocrystal structure [189]. The growing field of flexible electronics also makes use of nanoparticles. Coatings of nanoparticles, such as zinc oxide, are visually transparent and allow for the formation of transistors on flexible substrates [164]. Optimized performance of nanoparticle based technology is often dependent on the ability to control nanoparticle size and morphology during synthesis.

1.1 Zinc Oxide Nanoparticles

Zinc oxide is a semiconductor material with a wide range of modern applications [70]. The properties of zinc oxide nanoparticles have made them an ideal material for a wide range of applications. The strong UV light absorbance of zinc oxide nanoparticles is an often-cited positive property of the material [70,102,143]. Depositions of 40 nm zinc oxide nanoparticles can be used to make UV filters that are transparent to visible light [45]. The optical properties of zinc oxide can be exploited to create Bragg mirrors with tunable stop bands that are dependent on zinc oxide nanoparticle size [123]. Zinc oxide can also be used as a photocatalyst to break down aqueous organic contaminants [57]. Since zinc oxide has a wide light absorption spectrum, can generate electron/hole pairs, and is a low cost material, it is ideal for use in both UV and solar irradiated water treatment systems [129]. The optical and electronic properties of zinc oxide nanoparticles have been successfully used to make UV photodetectors from ZnO nanoparticles in the 70 to 100 nm size range [40,60]. Zinc oxide mesocrystals have also been successfully used as ethanol and glucose sensors [182,189]. The wide range of synthesis methods that exist for zinc oxide include: solid state, vapor, aqueous, and organic solvent based methods. Out of these methods, many

different morphologies of nano-sized zinc oxide has been reported: quantum dots, spherical, ellipsoids, needles/rods, hexagons, and many others [2,46,50,87]. The work presented in this dissertation is focused solely on the aqueous synthesis of zinc oxide through the reaction of a zinc salt and a base.

1.2 Synthesis of Nanoparticles

Synthesis methods for nanoparticles range from mechanical to chemical methods. Nanoparticles can be produced mechanically by the milling of a bulk material until nano-sized particles are formed [143]. This method, however typically produces a wide particle size distribution. Nanoparticles can also be produced using pyrometallurgical methods where a metal is vaporized, the vapor is brought into contact with oxygen, cooled, and then the resulting particles are collected [102]. These methods cannot, however, offer the control over particle morphology and size that solution based precipitation does. The work presented in this dissertation is focused solely on the solution based precipitation of nanoparticles.

Precipitation of nanoparticles occurs in multiple steps. First a reaction, such as the reduction of a metal ion, forms monomers of the precipitating species [104]. The concentration of the monomers in solution then increases into the range of supersaturation. The monomers in the supersaturated solution begin to aggregate and form nuclei [151]. Nuclei must reach a critical radius in order to precipitate. The critical radius is a particle size large enough to exist as a stable solid phase, resisting dissolution [35]. Rapid nucleation of the nuclei then occurs, forming nanoparticles. These particles can then grow due to diffusion of monomers to the nanoparticle surfaces. Further growth can occur through aggregation and Ostwald ripening [151] .

Control over nanoparticle morphology and size can be accomplished through the use of surfactant or ligand molecules [104,138]. When these molecules bond to the surface of the

nanoparticle, they inhibit the growth of the surface they are bonded to. When the molecules uniformly cover the surface of a nanoparticle, they act as a capping layer and inhibit further growth. When the molecules preferentially bond to specific crystal planes, the formation of anisotropic particles can occur through directed growth. Anisotropic structures can also form through the ordered aggregation of nanoparticles into mesocrystals [105].

1.3 Choice of Reactor

Nanoparticle synthesis has been conducted in every category of reactor design, batch, semi-batch, and continuous [101,104,187]. Each reactor type has positive and negative attributes for conducting nanoparticle synthesis, similar to any chemical reaction. The choice of a reactor type for nanoparticle synthesis must weigh the tradeoffs and constraints associated with each reactor type.

Batch reactors for nanoparticle synthesis range from simple stirred vessels to hydrothermal reactors using a pressurized headspace. Minimal equipment is required for a batch reactor and reagent addition can be accomplished by the direct addition of a solution from a flask to the reactor. Since the reaction solution is in contact with the walls of the reactor, fouling of the reactor can occur. Batch reactors also suffer from poor scale up behavior due to the changes in mixing that occur as the reaction volume is increased [108]. Since a batch reactor is non-continuous, the entire reaction volume must be emptied from the reactor at the end of the reaction. Semi-batch reactors are used in nanoparticle synthesis to control the rate of reagent addition [101]. These reactors, however, still have the shortcomings of conventional batch reactors.

Tubular flow reactors (TFRs) on both the milli- and microfluidic scale have been used for nanoparticle synthesis [54,90,187]. TFRs are continuous reactors and the reaction time in the reactor is controlled by the residence time. Scale up of TFRs can be accomplished by either

increasing the flow rate of the reagents into the reactor or by scaling out the number of reactors used [116]. Due to the dimensions and flow rates used, these reactors typically operate in the laminar regime. The parabolic flow profile of the laminar regime can create a residence time distribution, leading to wider particle size distributions [187]. Single phase tubular flow reactors used for nanoparticle synthesis are also prone to fouling, which can lead to clogging [96].

Droplet flow reactors take advantage of the ability to form monodisperse droplets in laminar flow and use the droplets as self-contained reaction volumes [111]. Conducting nanoparticle synthesis within the droplet volume prevents fouling since the droplet is separated from the reactor wall by a film of the continuous liquid phase [108]. Heat transfer [39] and mixing [152] are also enhanced due to the recirculating flow patterns that develop in both the droplet and continuous phase. Reagent combination in droplet flow reactors requires either the mixing of inlets into a single stream, which could be prone to fouling, or a method of droplet merging. Droplet merging often requires a specialized channel design, precise flow rate control, and can be impeded if surfactants were used [7].

Interphase mass transfer can be used to overcome the issue of reagent combination in droplet reactors while maintaining the desirable traits of this reactor design. In an interphase droplet reactor, one reagent is initially dissolved in the continuous phase while the other reagent is present in the droplet phase. The concentration difference between the two phases drives the mass transfer of the reagent in the continuous phase to the droplet phase. This method greatly simplifies the reactor design and eliminates the issues associated with reagent combination in droplets. The recirculating flow patterns of droplet flow and the smaller length scales present in these reactors enhances the mass transfer between the phases [27,174]. Intensification of reaction rates has also been observed in interphase droplet reactors [11]. The rate of mass transfer can be

controlled by changing the flow rates [175], droplet volumes [29], droplet spacing [44], or adding surfactants to the system [1,72]. Use of an interphase droplet reactor does, however, place constraints on the fluids and reagents that can be used. One of the reagents must be soluble in both the continuous phase liquid and the droplet phase liquid, while the other reagent can only be soluble in the droplet phase. The continuous phase and droplet phase must also be immiscible.

While the published work on nanoparticle synthesis in droplet flow reactors is extensive [106,108,111], nanoparticle synthesis using interphase droplet reactors has been much more limited. $BaSO_4$ nanoparticles have been produced in a two phase system using sulfuric acid dissolved in a continuous alcohol phase and a droplet phase containing aqueous $BaCl_2$ [82]. Silver nanoparticles have been synthesized in an interphase droplet reactor using a weak acid dissolved in the continuous phase and a droplet phase formed from an aqueous chloroauric acid solution [74]. A coaxial flow reactor has been used to synthesize TiO_2 nanoparticles in a stable annular flow [148]. I have established that zinc oxide nanoparticles can be synthesize using a continuous phase consisting of sodium hydroxide dissolved in 1-octanol and aqueous droplets containing zinc acetate [192].

1.4 Objectives

Interphase droplet flow reactors provide numerous advantages over the more common methods of nanoparticle synthesis. The objectives of the work presented in this dissertation are:

- Design and characterize an interphase droplet reactor for the synthesis of metal oxide nanoparticles
- Study the effect of reaction parameters such as reaction temperature, flow rate, residence time, droplet volume, and reagent concentration on zinc oxide nanoparticle size and morphology

- Investigate the effect of surfactants on mass transfer and nanoparticle size and morphology
- Study the effect of reactor scale on zinc oxide nanoparticle size and morphology
- Demonstrate the interphase droplet reactor's capability to synthesize other metal oxides by synthesizing copper oxide nanoparticles

In Chapter 2, I will present background information on nanoparticle applications and synthesis methods. In Chapter 3, I will describe the materials and methods used for the experiments in this dissertation. In Chapter 4, I will discuss the design of the interphase droplet reactor and its characteristics. Chapter 5 will cover the results of zinc oxide nanoparticle synthesis at higher reagent concentrations. In Chapter 6, I will discuss the synthesis of ellipsoidal mesocrystals formed through oriented aggregation and how surfactants affect this process. Chapter 7 will contain the results of conducting synthesis in reactors with smaller diameters. Chapter 8 will cover the synthesis of copper oxide nanoparticles and Chapter 9 will summarize the work presented and discuss future work.

Chapter 2: Background

The unique chemical and electrical properties that arise in nanoscale materials has been applied to a wide field of technologies. Nanoparticles have been successfully incorporated into energy storage, energy production, sensing, and catalysis. The wide range of applications for nanoparticles has been made possible by an increasing variety of synthesis methods for these materials. Both batch and continuous synthesis methods have been used to produce nanoparticles of many different types and morphologies. Droplet reactors for nanoparticle synthesis have been shown to offer many benefits over batch reactors and single phase continuous reactors. A subset of droplet reactors, interphase droplet reactors, has been limited in its applications for nanoparticle synthesis, despite the advantages it offers.

2.1 Nanoparticle Applications

2.1.1 Energy Storage

The increasing use of renewable energy sources and battery based technologies has driven research into the use of nanoparticles to improve the performance of energy storage methods. A limitation of solar energy is the inability to produce energy at night [14]. To overcome this issue, solar energy in the form of heat can be stored and then recovered at night. Solar heat collection can also augment solar energy production since the majority of solar energy is typically lost as heat. Nanoparticle suspensions have been found to enhance the thermal conductivity of heat storage fluids, improving heat transfer and therefore energy storage [28]. Selvakumar and Suresh used CuO nanoparticles to produce a nanofluid for improved heat transfer [135]. The authors demonstrated that an aqueous nanofluid containing 0.2 vol. % nanoparticles increased the convective heat transfer coefficient by 30%. The authors attributed the enhancement to the

presence of Brownian particle motion and the increased contact occurring between the CuO nanoparticles and the channel wall. Suresh et al. compared the thermal performance of CuO nanofluids and Al_2O_3 nanofluids [147]. The authors found that CuO nanofluids had better heat transfer than the Al_2O_3 nanofluids. They partially attributed this to the higher thermal conductivity of CuO. They also noted that the CuO nanoparticles had an average size of 30 nm compared to the 43 nm Al_2O_3 nanoparticles, which increased the surface area of the CuO nanoparticles also improving the heat transfer of the CuO nanofluid.

Nanoparticle mesocrystals have been used as both anode and cathode materials in lithium ion batteries and have shown good stability, fast kinetics, and safe operation [94,158]. Xu et al. demonstrated the use of CuO leaflike mesocrystals as an anode material for lithium ion batteries [176]. The authors showed that the CuO mesocrystals had good cycle performance compared to thicker CuO flake structures. The authors attributed the better performance of the leaflike mesocrystals to ability of the mesocrystal to undergo the volume change caused by lithium ion insertion. Cao et al. used V_2O_5 mesocrystals as the cathode material for lithium ion batteries [12]. The authors were able to construct hollow microspheres consisting of assembled V_2O_5 nanorods. They attributed the good electrochemical performance of these structures to more efficient lithium ion intercalation.

2.1.2 Catalysis

Nanoparticles have found wide use in the field of catalyst research. Catalytic nanoparticles have been synthesized from materials such as gold, platinum, palladium, titanium dioxide, and zinc oxide [59,73]. Metals such as gold, have been found to only have catalytic properties at the nanoscale [21]. Haruta et al. demonstrated the catalytic oxidation of CO using gold nanoparticles [52]. The authors showed that the oxidation of CO only occurred with gold nanoparticles sized

smaller than 4 nm. Size effects have also been observed in the use of Pd catalysts in the Suzuki cross coupling reaction. Li et al. investigated the effect of the size of Pd catalysts by producing nanoparticles ranging from 3 to 7 nm [84]. The authors showed that catalytic activity peaked for a nanoparticle size of 3.9 nm. They attributed this to exposure of edge and vertex atoms on the nanoparticle surface and the higher catalytic activity possible with these atoms as compared to rest of the particle surface. Metal oxide nanoparticles such as TiO_2 and ZnO are well known for their photocatalytic activity [73]. Photocatalytic materials show a strong adsorption of light and an ability to readily form electron-hole pairs. Han et al. fabricated TiO_2 nanosheets with exposed (001) surfaces due the high photoactivity of this plane [51]. The authors where able to produce sheets with 89% the surface consisting of (001) facets, and demonstrated higher photocatalytic activity than a commercial TiO_2 photocatalyst. Pourrahimi et al. investigated the use of ZnO spheres formed from aggregated nanosheets as photocatalysts [117]. The authors observed high photocatalytic activity and where able to increase the catalytic behavior through heat treatment. The authors attributed the high photocatalytic activity of these structures, as compared to ZnO nanoparticles, to the high oxygen content of the exposed $(2\bar{1}0)$ planes of the nanosheets.

2.1.3 Electronics

Nanoparticles offer many attractive and tunable properties that make them useful materials in electronic applications. Many different nanoparticle materials have a luminescent property which has driven research into using nanoparticles in light sources [149]. Anikeeva et al. demonstrated the fabrication of Quantum Dot Light Emitting Devices with color emissions covering the entire visible spectrum [4]. Control over the light emitted from the devices was controlled by the composition of the nanoparticles. The emissions in the blue range were produced by ZnCdS/ZnS particles, emissions in the yellow range were produced by CdSe/ZnS particles, and

emissions in the red range were produced by CdZnSe particles. Nanoparticles can also be used to improve the light emitting properties of bulk materials. Lin et al. demonstrated the improved light emitting properties of crystalline silicon with the deposition of a SiO_2 nanoparticle layer [85]. The nanoparticles acted to localize the electron-hole pairs, improving light emission behavior. The light sensitive behavior of metal oxide nanoparticles that makes these materials ideal photocatalysts can also be used to make light sensors. Zheng et al. investigated the use of TiO_2 nanorods for use as a UV photodetector [190]. The authors demonstrated that by adding TiO_2 nanoparticles to the nanorod array the speed and level of response by the sensor was improved. The authors attributed the improvement to the increased surface area of the nanoparticles. Gas sensors are another area where the electronic properties and small size of nanoparticles has been beneficially exploited. The increase in surface area produced by the use of nanoparticles increases the area available for interaction with the gaseous species of interest [5]. Yang et al. studied the use of CuO nanostructures as gas sensors for the detection of ethanol and ethyl acetate [180]. The authors compared two different morphologies, nanosheets and nanoflowers. They demonstrated that the nanoflower morphology had better electrical response to the presence of gaseous species. The authors attributed the better performance of the nanoflower morphology to the enhanced connectivity of the sheets that comprise the flowers and to the more open structure of the flowers.

2.2 Zinc Oxide Nanoparticle Applications

2.2.1 Photovoltaics

Zinc oxide nanomaterials contain many properties that make them ideal components for fabricating photovoltaic cells. Zinc oxide has a wide band gap energy of 3.37 eV, high electron mobility, and it also has a strong ability to scatter light which can enhance the cell's ability to harvest light [137]. Commonly, ZnO is used in a dye sensitized solar cell (DSC) where a dye

molecule is adsorbed onto the surface of ZnO nanoparticles. The dye molecule absorbs incoming light and transfers the electrons generated to the ZnO nanoparticles. Shi et al. used ZnO ellipsoidal and spherical mesocrystals as photoelectrodes in a DSC [137]. The authors discovered that the performance of the DSC was dependent on the overall size of the mesocrystals. Optimal performance was observed when the size of the mesocrystals matched the adsorption spectrum of the dye molecule. They also noted that as the size of the mesocrystals increased, the light scattering decreased, degrading the performance of the DSC. Chang et al. used two different ZnO mesocrystal morphologies as well as spherical nanoparticles to compare the effect of morphology on the performance of a DSC cell [15]. The authors found that the nanoflower morphology performed better than the conical morphology and the nanoparticles. The proposed explanation for the increased performance of the nanoflowers was the increased branching of the nanoflower improved light scattering and electron transfer.

2.2.2 Sensors

The properties of zinc oxide nanomaterials have also been used to construct both light and molecular sensors. The strong interaction of zinc oxide with UV light has been used to construct UV photodetectors. Foo et al. produced a UV photodetector using a film of ZnO nanoparticles deposited onto silicon wafer [40]. Using ZnO nanoparticles between 50 and 100 nm the authors demonstrated the ability of the photodetector to sense differing UV light intensities. Khokhra et al. constructed UV photodetectors from three different ZnO nanoparticle morphologies, ~ 60 nm nanoparticles, nanosheets, and nanoflowers [67]. They compared the ability of all three morphologies to detect light in both the UV and visible light range. The authors found that while the nanoparticles and nanosheets both had good response across the light spectrum, the nanoparticles showed much slower signal decay.

Zinc oxide nanostructures have also been used as gas sensors. Kaneti et al. investigated the ability of ZnO plates and ZnO nanorods to detect ethanol vapor [63]. The authors found the ZnO plates had a higher sensitivity and response towards the presence of ethanol in a gas stream. Using molecular modelling, the authors confirmed this was due to the higher area of the (0001) surface on the ZnO plates and the preference for ethanol to adsorb on the (0001) plane. Yu et al. synthesized ellipsoidal zinc oxide mesocrystals and investigated their use as an ethanol sensing material as well [182]. The authors found that the ellipsoidal structures displayed good ethanol sensing characteristics. The authors reported that the ellipsoids had a higher sensitivity to ethanol than the ZnO plates investigated by Kaneti et al. The comparison between the two results is interesting since the ellipsoids would have formed to minimize the surface area of the (0001) surface, while the plates were formed to maximize the (0001) surface.

2.2.3 Photocatalyst

Zinc oxide nanostructures have also been widely investigated as photocatalysts for the degradation of organic contaminants. Kumar et al. compared the photocatalytic behavior of three different zinc oxide nanostructure morphologies, nanorods, nanoflowers, and nanospindles [75]. The authors found that the nanorod morphology had the highest photocatalytic activity when exposed to UV light. The better performance observed with the use of nanorods was explained by the increased ability of oxygen molecules to adsorb onto the nanorod as compared to the other structures, increasing the amount of oxygen radicals formed. Dong et al. investigated the photocatalytic activity zinc oxide mesocrystals formed from different concentrations of the additive Tris [33]. The concentration of Tris controlled the morphology of the mesocrystals, high concentrations of Tris aided in strong oriented attachment of ZnO nanoparticles. The authors found that the more porous mesocrystal formed at a mid-concentration of Tris had the highest

photocatalytic activity and was comparable to a commercial TiO_2 photocatalyst. Shafaei et al. also compared the difference between ZnO and TiO_2 nanoparticles photocatalysts [136]. The authors used 21 nm TiO_2 nanoparticles and 100 nm ZnO nanoparticles and compared their photocatalytic ability under UV light. The authors found that under the optimized conditions for both catalysts, ZnO showed better catalytic performance.

2.3 Zinc Oxide Synthesis and Morphologies

A wide range of synthesis methods conducted in batch, hydrothermal, and continuous reactors have been used to produce zinc oxide nanoparticles [70]. Many different zinc oxide nanoparticle morphologies have also been demonstrated, from isotropic to anisotropic [50]. Anisotropic zinc oxide nanostructures can form through anisotropic growth, directed growth, and oriented attachment. Two polar surfaces are present along the *c*-axis of zinc oxide, the (0001) and $(000\bar{1})$ surface. The (0001) surface is zinc terminated and the $(000\bar{1})$ surface is oxygen terminated. The polar nature of the zinc oxide wurtzite crystal structure is often exploited to produce anisotropic structures [93].

2.3.1 Spherical Nanoparticles

Spherical zinc oxide nanoparticles have been formed with sizes as small as a few nanometers [142]. The luminescent properties of ZnO particles in this size range has attracted much research interest. Hu et al. investigated the effect of the solvent used for the synthesis of colloidal ZnO particles on the size of the resulting nanoparticles. They used 5 different alcohols with increasing chain lengths at reaction temperatures between 30 and 65˚C in a batch synthesis. The alcohols used were ethanol, propanol, butanol, pentanol, and hexanol. While all solvents produced nanoparticles with approximately the same initial size, 1.5 nm, there was solvent dependent subsequent growth. Increasing the chain length of the alcohol used produced an increase

in the subsequent growth rate of the nanoparticles due to the increase in the solvent's viscosity and the surface energy of the nanoparticles in the solvent.

Small spherical ZnO nanoparticles have been successfully produced in microfluidic flow reactors. Schejn et al. synthesized ZnO quantum dots in a 500µm diameter tubular flow reactor [133]. The precursors used were ethanol solutions of zinc acetate and tetramethylammonium hydroxide. Carboxylic acid capping agents were added to restrict the particle growth. The authors successfully produced particles in the range of 5 nm and tuning of the particle's emission spectrum between 500 and 530 nm was possible by changing the reaction temperature. Kang et al. synthesized similar sized ZnO nanoparticles, 3-5 nm, by using zinc acetate and sodium hydroxide in a microfluidic channel [64]. The channel used had a square channel geometry with dimensions of 200 µm by 200µm, with a piezoelectric mixer integrated into the channel. No capping agents were used by the authors for their synthesis trials.

Larger spherical zinc oxide nanoparticles have also been produced. Moezzi et al. investigated the aqueous synthesis of zinc oxide nanoparticles and the effect of various reaction parameters on the size and morphology of the resulting particles [101]. Using aqueous zinc sulfate and sodium hydroxide as their reagents, they investigated the effect of reagent ratio, reaction temperature, and reagent combination order on the resulting particles. Using Zn^{2+}: OH^- ratios of 1:2 and 1:3 produced spherical particles with approximate sizes of 200 and 100 nm respectively. Increasing the ratio further in excess of OH^- produced a transition to the formation of plates. A similar transition was seen with different reaction temperatures. Reaction temperatures of 25 and 40˚C produced sheets while increasing the reaction temperature to 90˚C produced spherical particles approximately 100 nm in size. When the sodium hydroxide solution was added to zinc

sulfate solution, spherical particles were produced. When the zinc sulfate solution was added to the sodium hydroxide solution, anisotropic growth was seen in the form of star shaped particles.

Pourrahimi et al. investigated the effect of using different zinc salt precursors on the synthesis of zinc oxide nanoparticles in an aqueous batch reactor [118]. The authors used zinc acetate, zinc sulfate, zinc nitrate, and zinc chloride to determine how different anions impacted the size and morphology of the nanoparticles. The zinc sulfate and chloride salts produced non-homogenous sizes and morphologies. Both the sulfate and chloride zinc salts produced 10-30 nm nanoparticles as well as larger 80-100 nm particles. The trial conducted with zinc nitrate produced star shaped particles that formed through the oriented attachment of smaller zinc oxide nanoparticles. The use of zinc acetate yielded more homogenous 25 nm particles.

The use of miniemulsions in batch reactors has been a method explored for the synthesis of zinc oxide nanoparticles. Commonly in miniemulsion synthesis, the aqueous reagents are dispersed in an inert continuous phase. The reaction is initiated by the coalescence of droplets containing a zinc salt and an aqueous hydroxide source. The coalesced droplets then become the reaction volume, offering a method of control over the nanoparticle size. Lu and Yeh prepared a miniemulsion of aqueous zinc acetate in n-heptane and precipitated zinc oxide by the addition of NH_4OH to the emulsion [92]. The authors showed that the miniemulsion method produced smaller and less polydisperse particles than a single-phase aqueous batch reactor. They did not note though, if the presence of surfactants in the miniemulsion and the lack of surfactants in the single-phase batch reactor impacted their results. Winklemann et al. investigated the effect of the mechanical devices used to induce droplet coalescence in a miniemulsion reactor [172]. The authors found that the devices that induced the most coalescence produced smaller ZnO particles with narrower size distributions.

Hydrothermal synthesis of zinc oxide nanoparticles has also been investigated. A hydrothermal reactor uses a pressurized headspace to increase the boiling point of water, the solvent, allowing reaction temperatures above the normal boiling point of water to be used. Demoisson et al. [26] investigated a wide range of hydrothermal reaction temperatures and pressures and how these two parameters impacted the synthesis of zinc oxide. Using zinc nitrate and potassium hydroxide, the authors saw low temperatures and low to high pressures favored the production of anisotropic particles, whether through anisotropic growth or oriented attachment. This indicated that nucleation was slower under these conditions. Increasing both reaction temperature and pressure decreased the anisotropy of the particles. The ZnO particles transitioned from ellipsoids and rods to spherical particles at the highest temperatures and pressures used. Particles formed in super critical water were spherical with an approximate size of 25 nm, indicating that nucleation was the dominant factor under those conditions. Søjesen et al. investigated the hydrothermal flow synthesis of zinc oxide particles and the effect of reaction temperature and pH, at constant pressure, on the particle morphology [140]. Using zinc nitrate as well, but sodium hydroxide as the hydroxide source, the authors observed similar behavior to Demoisson et al., lower reaction temperatures favored anisotropic growth, producing double cone structures. Spherical 20-25 nm particles were produced at temperatures above 210˚C. The morphology transition was attributed to the decrease in water's dielectric constant as temperature increased, allowing for higher supersaturation and faster particle nucleation. Conducting the synthesis under acidic or basic conditions allowed for the formation of rod morphologies and plate morphologies respectively.

2.3.2 Nanorods

Zinc oxide's polar crystal structure makes it an ideal material for the formation of nanorods. The wurtzite structure contains two polar planes, the positive (0001) plane and the negative $(000\bar{1})$ plane [93]. From a surface energy perspective, growth in the [0001] direction is favored in order to minimize the surface area of the polar planes relative to the non-polar planes. Growth of nanorods in the [0001] direction increases the surface area of the non-polar planes. Many investigators have developed methods for the synthesis of zinc oxide nanorods and nanowires.

Verges et al. demonstrated the synthesis of nanorods from aqueous solutions of zinc nitrate and hexamethylenetetramine (HMTA) [163]. The authors showed the formation of rods occurred at higher concentrations of HMTA and lower concentrations of zinc nitrate. The complex behavior of HMTA is believed to aid in the formation of ZnO nanorods [49]. Zhang and Mu formed ZnO nanorods in a hydrothermal reactor operated at 120˚C using aqueous solutions of zinc acetate and sodium hydroxide. The authors found that by increasing the stoichiometric ratio of OH^-: Zn^{2+} above 11:1 they were able to form nanorods. Lower ratios produced flower structures formed from multiple rods aggregated together. Fan et al. investigated the role of the solvent in the formation of ZnO nanowires and nanorods. Zinc acetate and potassium hydroxide were used in either aqueous or ethanol solutions at 180˚C. When ethanol was used as the solvent, slender nanowires were formed. When water was used as the solvent, shorter and wider nanorods were formed. It was determined that both of these morphologies were formed through the order attachment of small nanoparticles. Monocrystalline wires and rods resulted from the Ostwald ripening and fusion of the nanoparticle assemblies. The authors proposed a few explanations for why wires formed in ethanol but not water. The solvated zinc hydroxide reaction intermediaries have a larger solvation radius in ethanol than in water, limiting the amount that can adsorb onto a growing ZnO particle.

Also, the attachment process for ZnO nanoparticles in ethanol is much slower and limited in ethanol than in water.

2.3.3 Mesocrystals

The polarity of the zinc oxide crystal structure also allows for complex 3D morphologies to form through the oriented attachment of small ZnO nanoparticles. Oriented attachment occurs when nanoparticles align with the same crystallographic orientation. For zinc oxide, the alignment typically occurs in the [0001] direction and is driven by the higher surface energy of the polar faces of the crystal structure. When nanoparticles aggregate in a highly ordered manner, the surface energy of the resulting nanostructure is reduced, since the surface consists of the lower energy non-polar planes. Structures that form in this manner are referred to as mesocrystals and there are many different synthesis methods used to produce a range of ZnO mesocrystal morphologies.

ZnO ellipsoidal mesocrystals have been produced in a variety of reactor systems. Pu et al. investigated the aqueous synthesis of ellipsoidal mesocrystals in a batch reactor using zinc nitrate and aqueous ammonia as reagents [120]. The authors demonstrated that the morphologies produced through oriented attachment were sensitive to the pH of the system. More spherical mesocrystals formed at pH = 6 while ellipsoidal shapes were prevalent at pH = 8. When the pH was increased to pH = 10 and 12, dissolution of the structures was observed. The authors also observed that the oriented attachment process was rapid, proto-structures were observed within 10 seconds of reaction initiation. Liu et al. investigated the aqueous synthesis of ZnO ellipsoidal structures with the assistance of polyethylene glycol (PEG) [88]. Zinc nitrate and aqueous ammonia were used as the reaction precursors. The authors observed that the mesocrystals were formed from the oriented attachment of ZnO nanorods and particles. At the reagent concentrations used for the synthesis, PEG appeared to stabilize the nanoparticles initially formed, preventing

random aggregation. When PEG was not used, no mesocrystals were formed. Other groups have used polymers such as Jeffamine [69] and chitosan [189] to stabilize primary ZnO nanoparticles to allow oriented attachment to form ellipsoidal mesocrystals. Li et al. used a droplet flow reactor to synthesize ellipsoidal mesocrystals in a droplet flow reactor [81]. Zinc acetate and sodium hydroxide in ethylene glycol were used to form droplets in an inert continuous flow of tetradecane. The ethylene glycol stream was also mixed with different amounts of water to determine how the water fraction in ethylene glycol affected the formation of the ellipsoidal mesocrystals. The authors found that high fractions of ethylene glycol inhibited the oriented attachment process. The size of the mesocrystals produced through oriented attachment increased with increasing water content.

Star shaped mesocrystals are another widely reported morphology that arises through oriented attachment. Kumar et al. investigated the aqueous synthesis of ZnO mesocrystals in three different reactor systems [75]. The authors used a batch reactor, a sonicator, and a hydrothermal reactor along with two different zinc salts, zinc nitrate and zinc acetate. Star shaped mesocrystals were formed with zinc nitrate in the aqueous batch reactor and sonicator. The use of zinc acetate only produced star shaped mesocrystals in the sonicator reactor. Both reagents formed sheets in the hydrothermal reactor. This demonstrated the sensitivity of the oriented attachment process to not only the zinc salt but the reactor as well. Li et al. produced star shaped mesocrystals in a droplet flow reactor operated at 150˚C [80]. Aqueous streams of zinc acetate and sodium hydroxide were used to form droplets in an inert continuous flow of tetradecane. The authors found that increasing the concentration of sodium hydroxide at a constant zinc acetate concentration allowed for control over the oriented attachment process. At low sodium hydroxide concentrations, only small spherical aggregates were formed. Increasing the sodium hydroxide concentration favored the formation of star shaped mesocrystals. Oliveria et al. used a semi-batch double jet reactor to

produce star shaped zinc oxide mesocrystals [109]. Using aqueous zinc nitrate as the zinc salt, the authors found that pH levels controlled whether star mesocrystals were formed or ellipsoids. A pH = 9.5 favored the formation of ellipsoids, while increasing the pH to 10.5 produced stars. When zinc sulfate was used instead of zinc nitrate, only ellipsoidal structures were formed.

Spherical mesocrystals consisting of aggregated zinc oxide sheets have also garnered research interest. Wang et al. used aqueous zinc nitrate with sodium hydroxide to form ZnO sheet mesocrystals [168]. The authors found that it was possible to form mesocrystals from ZnO sheets at room temperature with a Zn^{2+}: OH^- ratio of 1:4. The addition of NH_4F as a complexing agent was found to aid in the formation of spherical mesocrystals. However too low or high concentrations of NH_4F would form nanorods. Sun et al. produced spherical sheet mesocrystals using zinc nitrate and sodium hydroxide as well [146]. The authors investigated the effect of the presence of trisodium citrate on the morphology of the mesocrystals. The authors observed that the packing of the sheets in the mesocrystal became less dense with increasing trisodium citrate concentration, indicating a steric behavior of the citrate ion.

2.3.4 Surfactants

The ability of surfactant molecules to adsorb onto nanoparticles has been used to direct the growth of ZnO nanoparticles. Singh et al. investigated the adsorption behavior of three different surfactant molecules and how they impacted ZnO particle growth [138]. The authors used Triton X-100, a large non-polar surfactant, Tween 80, another large non-polar surfactant, and sodium dodecyl sulfate (SDS), a small anionic surfactant. The two non-polar surfactants did not show plane specific adsorption onto ZnO. The non-specific coverage of both Triton X-100 and Tween 80 acted to reduce the size of the nanoparticles. Due to the negative charge of SDS, it preferentially adsorbed onto the polar (0001) plane of ZnO, producing short and wide nanorods. Increasing the

SDS concentration, however, was observed to produce higher aspect ratio nanowires. The authors proposed that increasing the SDS concentration inhibited its ability to adsorb onto the (0001) plane, causing adsorption to occur on the non-polar planes and causing nanowires to form. Usui investigated the ability of SDS to direct the formation of ZnO nanorod clusters [162]. Using no SDS, single ZnO nanorods were formed in a hydrothermal reactor. Adding SDS to the system produced a spherical cluster of nanorods, with the nanorods pointing outward from a central point. Increasing the SDS concentration was observed to increase the density of the nanorods in the cluster. The author proposed that the presence of SDS caused micelles to form around the initial nanoparticles formed in the reactor. The micelles restricted the growth of the particles, causing defects to form. The defects then acted as nucleation sites for nanorods to grow out of. Ratkovich and Penn investigated the use of carboxylic acids as surfactants to inhibit the growth of zinc oxide nanoparticles [122]. Adamantane carboxylic acid was found to be the best molecule at inhibiting growth and particle aggregation. The authors attributed this to the molecule's strong adsorption onto ZnO and to steric effects produced by its bulky structure.

2.4 Nanoparticle Synthesis in Droplet Reactors

As seen in the previous discussion on zinc oxide nanoparticle synthesis, many published studies on nanoparticle synthesis use batch reactors. Batch reactions are simple to setup and can be conducted in commonly available laboratory glassware. For nanoparticle synthesis reactions, there are shortcomings to the use of batch reactors. When nanoparticle synthesis is conducted in a single-phase batch reactor the reaction solution is in contact with the walls of the reactor, which can lead to fouling. Batch reactors also suffer from poor scale up behavior. As the volume of a batch reactor is increased, the changes in mixing and heat transfer can impact nanoparticle synthesis [108]. Since batch reactors are a non-continuous reactor, ending a reaction requires the

removal of the entire solution volume from the reactor. Conducting nanoparticle synthesis in a flow reactor can offer a solution to the shortcomings of batch reactors. The residence time of a continuous flow reactor is easily controlled by either the length of the reactor or the flow rate. Increasing the output of continuous reactors can be accomplished through scaling out the number of reactors, maintaining the optimized parameters of a reactor design [116]. Many types of nanoparticles have been successful synthesized in single phase continuous flow reactors. Single phase reactors, however, still have shortcomings of their own. The parabolic laminar flow profile produces a residence time distribution in the reactor, which can lead to broadening of the nanoparticle size distribution [108]. The reaction solution in a single-phase flow reactor is still in contact with the walls of the reactor, which can lead to fouling. While fouling is not a desired condition in any reactor, in the small channel dimensions used in millifluidic and microfluidic reactors fouling can lead to clogging [116]. Conducting nanoparticle synthesis in droplet flow reactors has been presented as a solution to the issues present in the use of both batch reactors and single-phase continuous flow reactors.

The ability to form monodispersed droplets in a flow of immiscible fluid has been a widely exploited feature of laminar flow in millifluidic and microfluidic devices. Conducting reactions inside of droplets in laminar flow overcomes many of the limitations that are present in single phase laminar flow reactors. One key advantage is the reduction or elimination of fouling of the channel wall. When the diameter of the droplet is much smaller than the diameter of the channel, a layer of the continuous phase is present around the exterior of the droplet, preventing any interactions between the droplet and channel. Even if the droplets have the same radius as the channel, a thin film of the continuous phase will be present between the droplet and the channel

wall [48]. With the reaction products entirely contained in the droplet volume, contact with the channel wall is eliminated, preventing fouling.

Another advantage of using droplets as reactors is the enhancement of mixing when compared to single phase laminar flow. Mixing in laminar flow is diffusive in the radial direction, only axial convection is present. Therefore, rapid mixing in laminar flow can be challenging. When a droplet translates through a channel, however, shear on the droplet's interface creates flow within the droplet volume. Due to the confined volume of the droplet, the flow is established as recirculating flow patterns within the droplet [150]. The recirculating flow patterns allow for convective mixing to occur inside the droplet, which is a much higher rate of mixing compared to the purely diffusional mixing of single phase laminar flow [153]. Mixing in droplets can be further enhanced by flowing droplets through channels that force droplets to turn, inducing chaotic mixing [141].

Flowing droplets through a channel not only creates recirculating flow patterns inside the droplet, similar flow patterns are also established in the continuous phase fluid. When a single file train of droplets are flowing through a channel, a volume of the continuous phase fluid exists between each droplet. Due to the motion of the continuous phase relative to the walls of the channel and the droplets, recirculating flow patterns are also established in the continuous phase during droplet flow. The establishment of recirculating flow patterns in both the continuous phase and the droplet phase leads to the enhancement of heat transfer [39,160] when compared to single phase flow.

Researchers have capitalized on the advantages of droplet flow reactors and have demonstrated the synthesis of a wide range of metal and metal oxide nanoparticles in droplet flow reactors. Zhang et al. investigated the synthesis of silver nanoparticles in a droplet flow reactor

[184]. The synthesis was conducted in aqueous droplets, containing the reaction precursors, which flowed in a continuous phase of silicone oil. When the synthesis was conducted without the use of surfactants, the authors observed interfacial adsorption of the silver nanoparticles on the droplet interface. The interfacial adsorption lead to polydisperse nanoparticle sizes and non-homogenous morphologies. When the surfactant Triton X-100 was added to the droplet phase, interfacial adsorption was prevented and homogenous particles were synthesized. Kim et al. demonstrated the successful synthesis of palladium nanoparticles in a droplet flow reactor [68]. The synthesis required the use of three separate reagent streams to form the droplet reactors. To accomplish this, droplet formation occurred at the tips of three capillaries, where all three streams combined into one droplet. The authors demonstrated that inadequate mixing occurred in the droplets as they flowed through the reactor, resulting in a wide particle size distribution. By introducing constrictions at the beginning of the reactor, the changing channel diameter induced enhanced mixing in the droplets, producing a narrower particle size distribution. Yu et al. synthesized zeolites in a droplet flow reactor [181]. An aqueous alumina stream and an aqueous silica stream were combined to form droplets in a continuous flow of paraffin oil. The authors observed the optimal ratio for the two aqueous streams was 1:1, which produced the narrowest particle size distribution. When the diameter of the reactor was decreased, the mean particle size produced decreased and the particle size distribution narrowed. The authors attributed this to enhanced mixing in the droplets caused by decrease in diameter creating a homogenous reaction volume in the droplets more rapidly.

When reactions are being conducted in a droplet, usually two or more reagent streams must be combined into one droplet volume. While there are options for reagent stream combination, each has a limitation. A simple method is to combine the reagents into one single-

phase stream that is then broken into droplets in a continuous immiscible flow [153]. While a straightforward method, the section where the streams are combined can act as a single phase laminar flow reactor. No matter how short the combination section is, there will always be a stationary layer of fluid present on the channel wall. This layer of fluid would be highly prone to causing channel fouling. Instead of using a pre-mixing geometry, droplets can been formed from multiple capillaries, each capillary introducing a different reagent [68,107]. This can only work, however, if there is no wetting of the capillary tips by the reagents. Any wetting would allow the streams to react on the tips of the capillaries which could also lead to fouling.

Another method of reagent combination is the direct addition of a reagent stream to an already formed droplet. In this system, a droplet is initially formed containing only one reagent. As the droplet travels downstream, it approaches a T-junction that contains a stream of a second reagent. By setting the flow rate correctly, the stream in the T-junction will add directly into the already formed droplet [155]. This method, though, works only for a specific range of flow rates and is prone to contaminating the T-junction stream with the droplet fluid as the droplet passes unless specialized geometries are used [78]. A similar method is to form a train of alternating droplets, with each alternating droplet containing a different reagent. Two different droplets can then be merged using a channel designs that force the droplets into close contact [139]. This droplet merging method, though, requires a specialized channel design, precise flow rate control, and would be impeded if surfactants were used [7].

2.5 Interphase Droplet Reactors

The issues associated with reagent addition by droplet merging and stream mixing can be avoided by using interphase mass transfer for reagent combination. Interphase mass transfer can be accomplished by initially separating reagents into the separate fluid phases of the droplet flow

reactor. A reagent initially located in the continuous phase will diffuse into the droplet phase, driven by the concentration difference that exists between the two phases. This provides a simple mechanism for reagent combination, does not depend on specialized geometries or narrow flow rate ranges. While the study of interphase mass transfer in droplet flow liquid-liquid extractors is an active area of research [174], the application of this reactor design to nanoparticle synthesis has been limited [111,116].

The synthesis of $BaSO_4$ nanoparticles in an interphase droplet reactor was demonstrated by Li et al [82]. The authors formed aqueous droplets containing $BaCl_2$ in a continuous long chain alcohol stream containing dissolved sulfuric acid. The authors found that as the droplet volume increased, the nanoparticle size decreased. Once the droplet radius was equal to channel radius, the nanoparticle size rapidly increased. After this transition, further increase in the droplet radius produced a decrease in the nanoparticle size. Kulkarni and Cabeza demonstrated the synthesis of silver nanoparticles in an interphase droplet reactor [74]. The authors formed aqueous droplets containing chloroauric acid in a continuous phase of toluene which contained an organic reducing agent. The authors used two different reactor types, one with hydrophobic walls and one with hydrophilic walls. The authors observed more homogenous nanoparticles when the hydrophilic reactor was used, which caused the aqueous phase to be the continuous phase. However, the operating conditions of the hydrophobic reactor were later optimized to produce homogeneous nanoparticles as well. The authors also noted that decreasing the channel size produced a decrease in nanoparticle size. While not conducted in using a droplet reactor, the continuous flow interphase synthesis of TiO_2 has also been shown. Takagi et al. used an annular flow of either hexanol, octanol, or decanol containing dissolved titanium tetraisopropoxide (TTIP) inside of an outer flow of isopropanol and water [148]. The synthesis of TiO_2 nanoparticles was initiated by the mass

transfer of the water from the isopropanol stream to the inner stream, where it reacted with the TTIP.

As discussed in Section 2.3, zinc oxide nanoparticles have been synthesized in both single phase continuous flow reactors and in droplet flow reactors. Published work on the interphase synthesis of zinc oxide nanoparticles has been limited to batch reactors. Vorobyova et al. synthesized zinc oxide nanoparticles by a using an interphase batch reactor [165]. A layer of decane containing zinc oleate was poured over a bottom layer of water or ethanol containing sodium hydroxide. The immiscibility of the two fluids created a stable interface and the reactor was stirred gently as to not break up the interface. The authors demonstrated that the reaction temperature determined which liquid phase the zinc oxide formed in. They were also able to demonstrate the formation of different particle morphologies. High reaction temperature and large excess of sodium hydroxide produced needle shaped particles. Frike et al. also used interphase mass transfer to synthesis zinc oxide nanoparticles, but in a miniemulsion reactor [41]. The authors used triethylamine dissolved in n-decane and aqueous droplets containing zinc acetate in the reactor. The mass transfer of triethylamine into the droplets initiated the reaction. The authors produced hexagonal zinc oxide nanoparticles with aspect ratios controlled by the reagent concentrations used. The work presented in this dissertation is the first investigation on the interphase droplet flow reactor synthesis of zinc oxide nanoparticles.

Chapter 3: Experimental Materials and Methods

3.1 Reagents

Zinc acetate dihydrate (Certified, Fisher Scientific), sodium hydroxide (ACS grade, Fisher Scientific), copper acetate (ACS grade, Acros Organics), 1-octanol (99% pure, Acros Organics), and 190 proof ethanol (ACS grade, Pharmco-Aaper), Triton X-100 (Alfa Aesar), sodium dodecyl sulfate (EMD), methyl orange (ACS grade, Acros Organics), and 0.1 M hydrochloric acid (Certified, Fisher) were used as received without further purification.

3.2 Solution Preparation

The required mass of zinc acetate or copper acetate was dissolved in 100 mL of ultrapure water (Milli-Q, 18.2 MΩ cm) at room temperature. For trials that used either sodium dodecyl sulfate or Triton X-100, the required mass of surfactants was added to the 100 mL of ultra-pure water. The required mass of zinc acetate was then added to the surfactant solution. The required mass of sodium hydroxide was dissolved in 100 mL of 1-octanol. The sodium hydroxide solution was agitated with a magnetic stir bar for 24 h at room temperature to fully dissolve the sodium hydroxide pellets. 0.05 M hydrochloric acid solutions were prepared by diluting a volume of stock 0.1 M hydrochloric acid solution. The required volume of ultra-pure water and 0.05 wt.% methyl orange solution were added to a volume of 0.1 M hydrochloric acid to make a final solution of 0.05 M HCl and $2x10^{-3}$ wt.% methyl orange. The concentration of $2x10^{-3}$ wt.% methyl orange was the approximate minimum concentration of the indicator that allowed for visual determination of the indicator's color change.

3.3 Reactor Designs and Construction

3.3.1 Millifluidic Reactor

The reactor used for the two-phase flow synthesis of zinc oxide nanoparticles was comprised of four parts, as shown in Figure 3.1. First, a co-flow drop formation apparatus was used to form droplets of aqueous zinc acetate solution in a flow of pure 1-octanol. Aqueous zinc acetate was pumped by a syringe pump through a 27-gauge stainless steel needle and droplets formed at the tip of the needle and entered the 1-octanol stream. The stream of droplets exited the drop formation setup through a PTFE tube and entered a T-junction. The second inlet stream of the T-junction was a stream of sodium hydroxide dissolved in 1-octanol which mixed with the 1-octanol of the droplet stream.

Third, the PTFE tubing containing the droplet reactors continued into a hot water bath where zinc oxide nanoparticles were synthesized at a set temperature between 25 and 80 °C. Different tubing lengths were used to control the residence time of the reactor while keeping the total flow rate constant. Finally, the reactor products were collected in an ice-cooled round-bottom flask containing 50 mL of 190 proof ethanol. For each trial at the set reaction conditions, the reactor products were collected for 30 min in the flask before they were prepared for analysis.

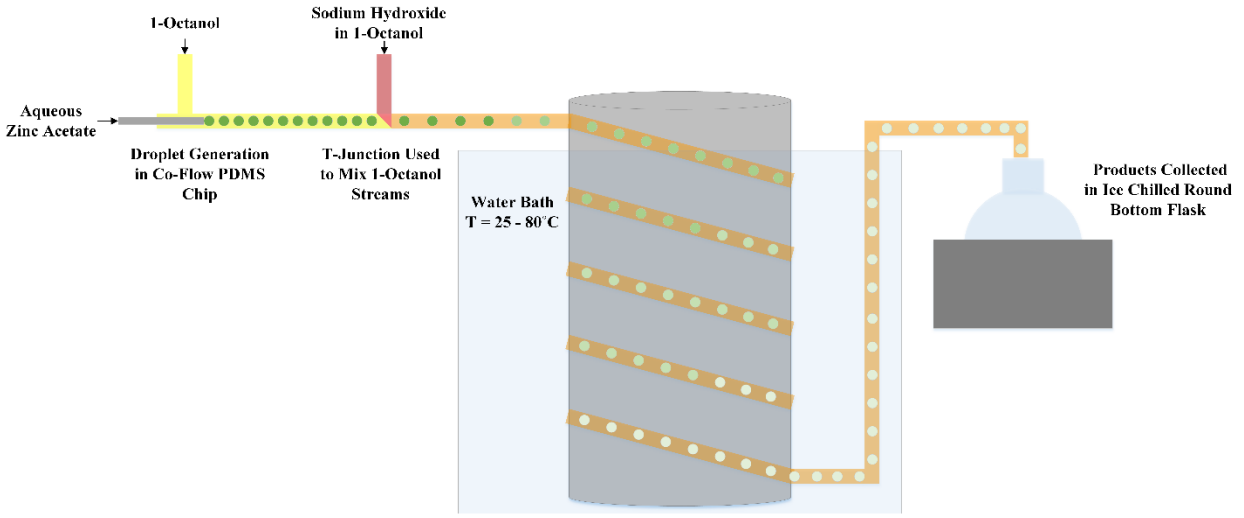

Figure 3.1: Experimental setup for the two-phase droplet flow synthesis of zinc oxide nanoparticles.

3.3.2 Millifluidic Chip Fabrication

The droplet formation portion of droplet reactor was fabricated by casting millimeter scale channels in polydimethylsiloxane (PDMS). First, two blunt tip dispensing needles were arranged perpendicular to each other in a petri dish to form a T-junction, seen in Figure 3.2(a). The needles were held in place by small pieces of modelling clay placed on the bottom of the needle hubs. The gauge of the needle was used to control the final channel diameter, 21-gauge needles produced channel diameters of approximately 0.8 mm, while 27-gauge needles produced channel diameters of approximately 0.4 mm. With the needles properly positioned, degassed, liquid PDMS was poured into the petri dish to a depth adequate to fully cover the needles. The petri dish was then placed in a 95˚C oven for 2 hours to allow the PDMS to fully cure. Once cured, the portion of PDMS containing the needles was cut out of the petri dish. The needles were then pulled out of the PDMS, leaving behind cylindrical channels, seen in Figure 3.2(d). To connect the PDMS chip to the syringe pumps, tubing with outer diameters slightly larger than the channel diameters was

inserted into the PDMS channels. Due to the flexibility of PDMS, a tight seal was formed around the tubing without the use of adhesive.

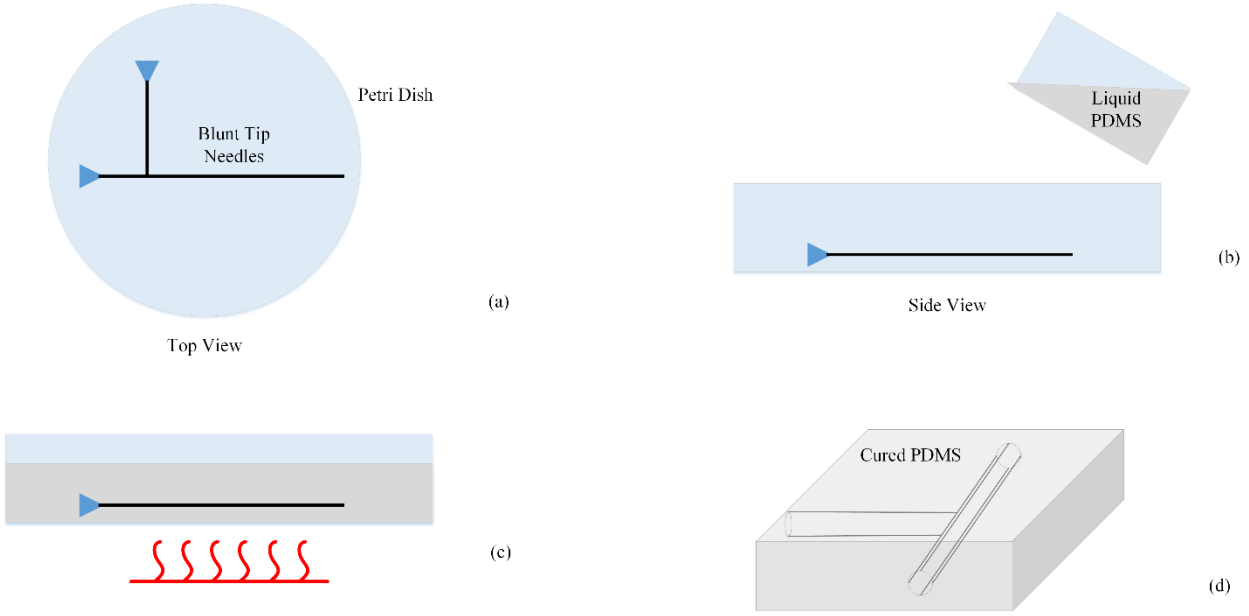

Figure 3.2: Steps of millifluidic chip fabrication in PDMS

3.3.3 Batch Reactor Synthesis

Batch reactor synthesis of nanoparticles was conducted in a 100 mL round bottom flask. Reaction temperature was maintained by placing the flask in a hot water bath and the flask was continuously stirred by a magnetic stir bar. The required volume of zinc acetate solution was added to the flask first and allowed to come up to the reaction temperature. The required volume of sodium hydroxide solution was initially held in a separate flask and was preheated to the reaction temperature as well. Once both solutions were at the appropriate temperature, the sodium hydroxide solution was added to the round bottom flask. The reaction was then allowed to proceed for the desired time. Once the reaction time had elapsed, the contents of the flask were emptied into centrifuge tubes and were centrifuged.

3.3.4 Microfluidic Reactor Fabrication

Fabrication of the microfluidic channels was accomplished using well established photolithography and soft-lithography techniques. This was a multistep process that included designing the chip, fabricating the design on silicon wafers, fabricating the chips from the silicon wafer molds, and finally bonding the resulting chip.

3.3.5 Photomask Design

The desired design of the microfluidic reactor was created as a 2-D computer aided design (CAD) drawing using the AutoCAD software program (Autodesk). After the drawing was completed, the design was made into a closed polygon and the file was sent to a photomask printer (CAD Art Services). The photomask was printed on a plastic transparency at resolution of 10,000 dpi or higher. The SU-8 photoresist used for microchannel fabrication was a negative photoresist, requiring the channel design to be transparent while the remaining unused space was opaque black. The photomask was then used to create the silicon wafer master mold of the microfluidic chip design.

3.3.6 Silicon Wafer Preparation

To create the silicon wafer master molds, 4-inch diameter silicon wafers (WRS Materials) were used. The silicon wafers used in this process were at least single side polished, no other wafer specifications were pertinent to this process. The silicon wafer was first dehydrated by placing it on a 200˚C hot plate for 1 hour. After the wafer was dehydrated, it was then placed on the vacuum chuck of the spin coater (CHEMAT). The following steps required the use a light sensitive photoresist and were conducted in a blacked-out room and only red light was used as a light source. Approximately 3 mL of SU-8 2035 (Microchem) was poured onto the center of the wafer, the lid of the spin coater was placed on and the spin cycle was started. The spin coater used two cycles,

the first cycle spun at 75 rpm for 12 seconds to spread the photoresist across the surface of the wafer. The second cycle spun at 2000 rpm for 30 seconds, the rpm required to thin the photoresist layer to a thickness of approximately 60 μm [193]. The wafer was then removed from the spin coater and was placed in a 65˚C oven for 10 minutes. After the 10 minutes were finished, the wafer was then placed in a 95˚C oven for 30 minutes. The two heating steps were used to ramp the wafer's temperature in order to evaporate a portion of the solvents present in the photoresist without stressing the photoresist.

3.3.7 UV Exposure and Developing

After the wafer was in the 95˚C oven for 30 minutes, it was taken out and allowed to cool. The photomask was then sprayed with compressed air to remove any dust and was placed under the glass pane on the mask aligner (OAI Model 2000). The wafer was the exposed to the aligner's UV light source for 9 seconds with a flux of 25 mW/cm^2. After the exposure was over, the wafer was then placed in the 65˚C oven for 1 minute and then the 95˚C oven for 10 minutes to aid the crosslinking of the photoresist.

After the wafer was removed from the 95˚C oven and had cooled, it was then immersed in SU-8 developer (Microchem). The wafer was gently agitated for 8 minutes, allowing the features to develop. Over the course of the 8 minutes, the crosslinked regions of the photoresist remained and the un-crosslinked regions dissolved in the developer. After 8 minutes, the developer was replaced with fresh developer and the wafer was agitated for 2 more minutes. After the 2 minutes had ended, the wafer was removed from the developer, rinsed with isopropyl alcohol and dried with a compressed air gun. The wafer was then placed in the 95˚C oven for 30 minutes.

3.3.8 PDMS Soft Lithography

Microfluidic devices were cast using polydimethylsiloxane (Sylgard 184, Dow Corning). A two-part elastomer kit containing an uncured PDMS liquid and the curing agent is used to form solid PDMS. The uncured liquid was mixed in a 10:1 by weight ratio with the curing agent. To maintain the optical clarity of the cured PDMS, the liquid was degassed to remove any trapped air bubbles formed while the two parts were mixed. After the PDMS had been thoroughly degassed, it was poured over the silicon wafer master mold and the master mold was then placed in a 65˚C oven for 2 hours. After the two hours, the PDMS was cured into a solid elastomer and the chip was cut off the mold with an X-Acto knife.

3.3.9 PDMS Bonding

The microchannels cast into the cured PDMS were sealed by bonding the PDMS chip to a substrate. Plain microscope slides, cleaned in a Micro-90 (International Products) solution for 10 minutes and thoroughly rinsed, were used for bonding. The bottom of the PDMS chip was first covered with Scotch Tape and holes were punch through the pre-designed ports in the chip using an appropriately sized blunt tip needle. The tape was then peeled off to remove any dust or particles present on the bottom of the chip. The chip and the glass slide were then placed in the plasma cleaner (Harrick). The vacuum chamber of the plasma cleaner was first evacuated for 5 minutes, then a low flow rate of pure oxygen was bled into the chamber for 2 minutes. After the 2 minutes, the oxygen flow was turned off and the RF coil was turned on to the low power setting (6.8 W). Once the plasma ignited, it was kept on for 15 seconds. After the 15 seconds, the plasma was extinguished and the chamber was brought back to atmospheric pressure. Bonding was initiated by immediately placing the PDMS chip onto the glass slide, channel side down. Bonding was

further promoted by placing the sealed microchannel in a 65˚C oven. This same plasma bonding procedure was used for bonding two pieces of PDMS together as well.

3.3.10 Positive PDMS Mold Fabrication

Polyester and polyurethane microfluidic channels were made using similar soft lithography methods as PDMS microfluidic chip construction. The procedure was modified to account for the issue of the cured polyester and polyurethane bonding to the silicon wafer master mold. Instead, a positive mold constructed from PDMS was used to cast the microfluidic channels. The PDMS positive mold was created by using a PDMS microfluidic chip with the desired channel design as a negative mold. By casting a new layer of PDMS over the negative mold, a new positive mold was cast out of PDMS. To prevent the new layer of PDMS from bonding to the already cured layer, the cured layer was subjected to a surface treatment. The cured layer was first exposed to an oxygen plasma for 20 seconds and then immersed in a solution of 75 vol.% ethanol, 20 vol.% water, and 5% Micro-90 cleaning solution for 5 minutes [167]. After the 5 minutes of immersion, the PDMS was dried using compressed air and a box was constructed around the edge of the cured PDMS to contain the new layer of PDMS to be poured on top.

With the box in place on the edges of the negative mold, the mold was then set on a 150˚C hot plate. While the mold was heating, liquid PDMS was mixed with the curing agent in the suggested 10:1 weight ratio and subsequently degassed. Once the uncured PDMS was degassed, it was poured onto the hot negative mold. Due to the temperature of the negative mold, the uncured liquid PDMS cured in approximately 10 minutes. Once the PDMS was cured, the two layers were taken off the hot plate and allowed to cool to room temperature. Once cooled, the negative layer and positive layer were carefully peeled apart. The negative PDMS layer could be used again to make PDMS molds if needed.

3.3.11 Polyester Casting

Similar to the creation of the positive PDMS mold, a box was first made around the positive PDMS mold to contain the uncured liquid polyester. To make a hole in the cured polyester to access the inlet and outlet ports of the microfluidic channel, a 21-gauge needle inserted through a piece of 21-gauge PTFE tubing was used. The tip of the needle was left uncovered by the tubing and was pressed into the port feature of the PDMS mold. The cured polyester does not bond to PTFE tubing, which allowed a hole to form in the cured polyester. A similar box was made around a flat piece of PDMS to create a flat piece of polyester that was used as the bottom of the polyester chip to seal the microchannels. Polyester resin (Castin' Craft) was then mixed with catalyst in the manufacturer suggested ratio of 15 drops of catalyst to every 28 g of resin. These two parts were then stirred together and allowed to sit for 1 minute to allow large air bubbles to rise to the surface. The liquid polyester was then poured over the two PDMS molds and allowed to cure at room temperature for 1 hour.

3.3.12 Polyester Bonding

After 1 hour, the molds were placed in a 65˚C oven for 15 minutes and then allowed to cool for 10 minutes. Once cool, the needles were pulled out and the polyester layers were carefully peeled off the PDMS. The two polyester layers were then pressed together and cured at room temperature for 1 hour. After the 1 hour, the polyester chip was then placed in a 65˚C oven for 10 minutes and then placed in a 100˚C oven for 1 hour for a final cure [37].

3.3.13 Polyurethane Soft Lithography

The same positive mold setup used for polyester soft lithography in Section 3.3.12 was used for polyurethane soft lithography. The two Econ60 polyurethane prepolymers (Smooth-On)

were mixed together in a 1:1 weight ratio. After thoroughly stirring the two liquids together for 1 minute, the liquid polyurethane was then poured over the positive PDMS mold.

3.4 Droplet Measurements

3.4.1 Droplet Images

Images of droplets forming at the reactor inlet were taken with a CMOS camera (Pixelink PL-B741U, 1.3 MP resolution) perpendicular to the PDMS chip used for droplet formation. Images of the droplets at the reactor outlet were taken with the same camera. To minimize refraction and capture a clear image of the droplets in the PTFE tubing, the tubing was immersed in a rectangular petri dish containing 1-octanol. The images were then taken through the wall of the petri dish.

3.4.2 Droplet Volume Measurement

Images of the droplets in the PDMS droplet generation chip at the reactor inlet were used to calculated droplet volume. Due to inconsistencies in the background lighting of the images, the outline of the droplet interface had to be manually traced, allowing the interior of the droplet to be colored black. The image was then converted to a binary black and white image using the Threshold tool in ImageJ. The binary image was then imported into MATLAB and a custom script was used to first identify the droplet outline and then calculate the volume of the droplet using a volume of revolution. The volume of the droplet was calculated using Eqn. (3.1),

$$V = \sum_1^k \pi \left(\frac{y_{k+1}+y_k}{2}\right)^2 (x_{k+1} - x_k) \tag{3.1}$$

where V is the volume of the drop, y_k and y_{k+1} are the height of pixels k and k+1 at the droplet interface, and x_k and x_{k+1} are the horizontal position of pixels k and k+1 at the interface. The horizontal centerline of the droplet is adjusted to be at 0 in the MATLAB script and the summation

is continued for all values of y greater than 0. The y and x values are converted from pixel units to real world units by measuring the known width of the dispensing needle in each image used.

3.4.3 Droplet Sensor

Real time droplet length measurements were made using a droplet sensor. The sensor consisted of a photodiode and a blue, 470 nm, LED as a light source. The LED was set 180˚ from the photodiode and the reactor tubing passed between the two, perpendicular to both the LED and the photodiode as seen in Figure 3.3(a) [155]. Holes were drilled in a piece of black plastic to hold the LED, photodiode, and tubing to minimize noise in the light signal. When a droplet traveling through the tubing passed between the LED and the photodiode, the level of transmitted light changed which changed the current produced by the photodiode. The current produced by the photodiode created a voltage difference which was measured by the op-amp circuit in Figure 3.3(b) [86] . The voltage difference was amplified by the op-amp circuit and was output as a voltage level, read by an Arduino UNO and recorded using a custom MATLAB script.

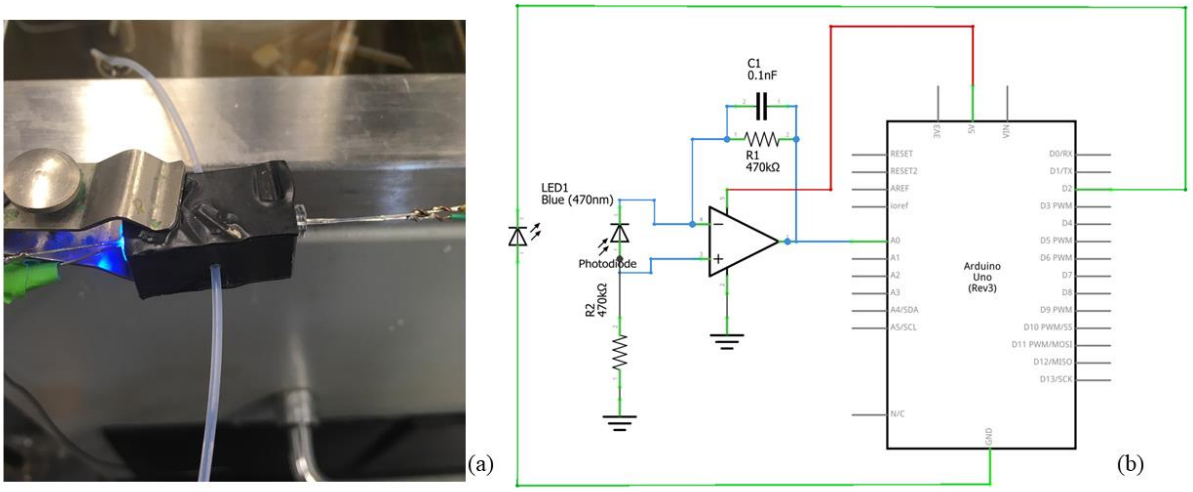

Figure 3.3: (a) Sensor device setup at the outlet of the millifluidic droplet reactor showing the blue LED light source on the left and the photodiode on the right. (b) Schematic of the wiring for the sensor circuit connected to an Arduino Uno.

3.5 Mass Transfer Measurements

The experimental setup used to analyze the mass transfer behavior of the interphase droplet reactor consisted of the same tubing connections of the droplet reactor prior to the water bath. An aqueous stream of 0.05 M hydrochloric acid and $2x10^{-3}$ wt.% methyl orange was used to form droplets in a continuous flow of 1-octanol. Methyl orange was used as an indicator because it is water soluble and it has an acidic pH end point, pH = 4.4 [61]. The droplet laden stream then entered a T-junction where it was mixed with a stream of sodium hydroxide in 1-octanol. As the droplets exited the T-junction, the sodium hydroxide in the continuous phase began to diffuse into the droplets. After enough sodium hydroxide had diffused into a droplet to bring the pH of the droplet to the end point of the methyl orange indicator, the color of the droplet changed from red to yellow. The length downstream from the T-junction where the color change occurred was measured. The measured distance was converted to the time required for color change to occur by Eqn. (3.2)

$$t = \frac{\pi r^2 L}{Q} \tag{3.2}$$

where t is the time required for the indicator color change to occur, r is the tubing radius, L is the measured length, and Q is the total volumetric flow rate. To ensure the setup was operating at steady state, the position where the color change occurred was measured every 2 minutes until the percent change in the position was less than 5%. Once steady state operation was verified, the length required for color change to occur was taken as the average of 3 steady state measurements.

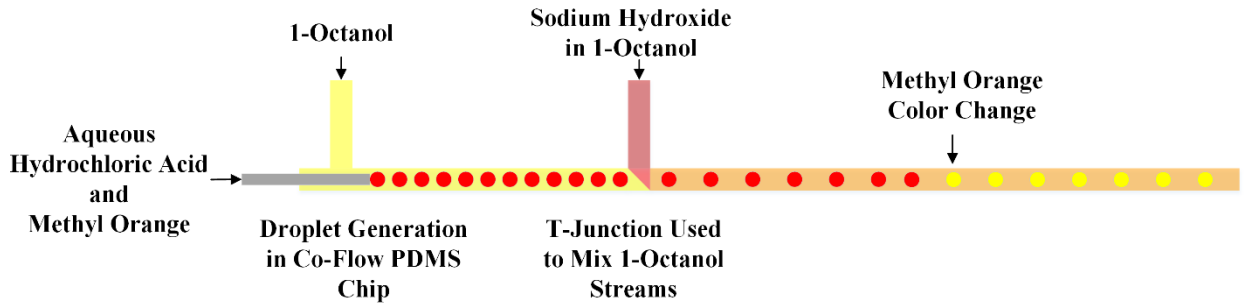

Figure 3.4: Experimental setup for conducting mass transfer measurements

3.6 Nanoparticle Washing

At the conclusion of a nanoparticle synthesis trial, the contents of the ice chilled round bottom flask were split into four 50 mL centrifuge tubes and were centrifuged at 4,000 rpm for 20 min in an Eppendorf 5702 centrifuge. The supernatant was decanted until approximately 1 mL remained. The zinc oxide nanoparticles were then dispersed into the remaining liquid and centrifuged at 13,000 rpm for 10 min in an Eppendorf Minispin Plus centrifuge. The supernatant was decanted and replaced with fresh ethanol. The zinc oxide nanoparticles were then dispersed into the ethanol using an ultrasonic bath. The centrifugation and washing steps were repeated four more times. After the last centrifugation, the supernatant was decanted and the tubes were placed in a 60 °C oven to evaporate any remaining liquid.

3.7 Nanoparticle Characterization

3.7.1 Scanning Electron Microscope

Images of the zinc oxide nanoparticles were taken using a Tescan Lyra3 scanning electron microscopy (SEM) instrument using the in-beam secondary electron detector at an accelerating voltage of 6.0 kV. The zinc oxide samples used in the SEM instrument were first dispersed in acetone using an ultrasonic bath and then deposited on silicon wafer squares. The silicon wafer squares were first placed on 50˚C hotplate in order to increase the acetone evaporation rate. Before

viewing in the SEM instrument, the samples were sputter-coated with a gold−palladium layer to improve conductivity.

3.7.2 Energy Dispersive Spectroscopy

Elemental analysis was conducted using Energy Dispersive Spectroscopy (EDS) an EDAX EDS system on the Lyra3 SEM. An acceleration voltage of 20 kV and a magnification of 211,000X was used for the analysis.

3.7.3 Nanoparticle Size

Size measurements were made only for samples with nearly spherical particles by importing the SEM micrographs into Microsoft Visio. Nanoparticles with clear edges were manually selected from different regions of the micrograph, and the longest axis of each particle was measured and recorded as the particle size. The particle size distribution, mean size, and the standard deviation for any sample for a collection of 200 nanoparticles is reported.

3.7.4 X-Ray Diffraction

X-ray diffraction was conducted on two systems, a Bruker D2 Phaser diffractometer and a Bruker AXS diffractometer with a general area detector. The D2 Phaser was equipped with a copper X-ray tube and CuKα1 X-rays were used for the analysis, $\lambda = 1.5406$ Å. The tube was operated at a voltage of 30 kV and a current of 10 mA. Due to the limited mass of the nanoparticle samples used, a silicon wafer zero background plate (MTI Corporation) was used to support the samples in the diffractometer. The Bruker AXS diffractometer was equipped with a cobalt X-ray tube and CoKα X-rays were used for the analysis, $\lambda = 1.79026$ Å. Samples were deposited onto a piece of glass glued to a SEM stub. The SEM stub was then placed in the path of the X-ray beam for analysis.

3.7.5 Thermal Gravimetric Analysis

Thermal gravimetric analysis (TGA) of the nanoparticle samples was conducted on a Mettler-Toledo TGA/DSC 1 STAR^{e} system using temperature range of 30˚C to 600˚C with a 5˚C/min ramp rate in an argon atmosphere. The gas flow was set at least 12 hours before any measurements were made to stabilize the atmosphere in the TGA furnace. Alumina crucibles were used for the measurements and taring of the crucibles and measurement of the initial sample mass were done using the system's internal scale.

Due to sample sizes of 5-10 mg being used for these measurements, the buoyancy effect of the furnace atmosphere had to be accounted for in order to accurately capture a sample's mass loss [42]. To account for this behavior, the mass of a blank crucible was measured through the whole temperature range. This was repeated 5 times and the average net mass increase was used to construct a blank curve that was then subtracted from any future experimental data.

Chapter 4: Design and Characteristics of Interphase Droplet Flow Reactor

The interphase droplet flow reactor accomplishes reagent addition through the mass transfer of sodium hydroxide from the continuous phase to the dispersed aqueous droplet phase. This maintains the benefits of using a droplet flow reactor for nanoparticle synthesis while simplifying the reagent addition process. The work presented in this chapter discusses the design of the reactor, droplet merging behavior in the reactor, and the mass transfer characteristics of the reactor. The effect of reaction temperature, reagent concentration, surfactants, and droplet volume on droplet merging was measured using the droplet photosensor described in Chapter 3. The effect of total flow rate, droplet volume, and surfactants on the rate of mass transfer was measured using an acid-base titration.

4.1 Reactor Design

The schematic of the interphase droplet reactor is shown in Figure 4.1 and details of the highlighted reactor sections are shown in Figure 4.2. Droplet formation in the interphase droplet reactor occurred in a cylindrical PDMS channel as described in Chapter 3. A stream of aqueous zinc acetate was introduced into stream of pure 1-octanol through a 27-gauge blunt tipped needle placed concentrically in the PDMS channel. As the aqueous stream was introduced into the immiscible 1-octanol stream, the viscous force of the flowing 1-octanol pinched off the aqueous stream into droplets. The droplet formation area of the reactor is highlighted by box (a) in Figure 4.1 and Figure 4.2(a) shows a still image from video of droplet formation occurring in the PDMS chip. Due to the needle being positioned in a co-flow arrangement, the gauge of the needle, and the flow rates of both the continuous phase and droplet phase, droplets were formed with a diameter approximately the same as the channel's, $\kappa \sim 1$. In trials where it was desired to have a

larger droplet volume, a PDMS channel with a larger channel size and smaller needle gauge were used instead. The elasticity of the PDMS channel made it easy to connect and disconnect channels to the PTFE tubing that comprised the rest of the reactor.

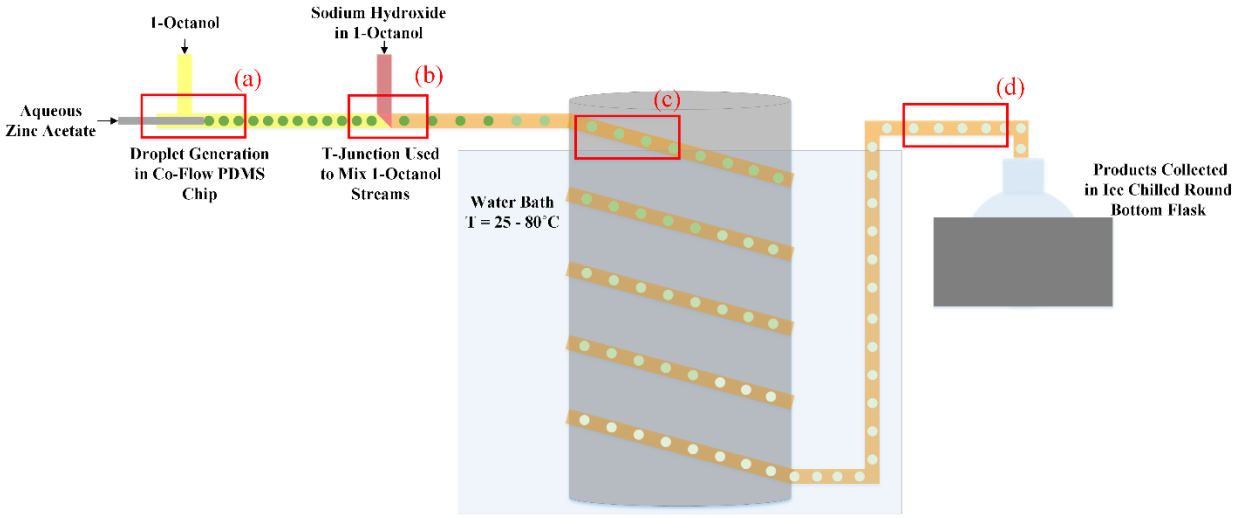

Figure 4.1: Schematic of the interphase droplet reactor with boxes highlighting key aspects of the design. (a) Droplet generation in the PDMS chip at reactor inlet, (b) introduction of sodium hydroxide in 1-octanol stream into T-junction, (c) reactor downstream, (d) reactor outlet.

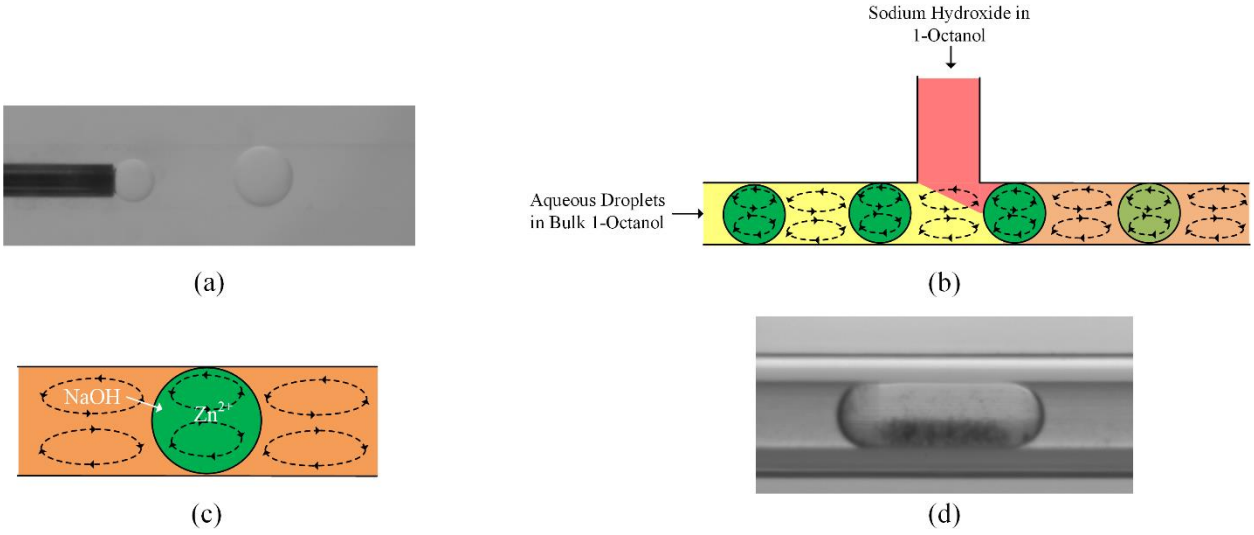

Figure 4.2: Images and schematics corresponding to the highlighted boxes in Figure 4.1. (a) Droplet formation in a stream of 1-octanol, (b) schematic of stream mixing occurring in the T-junction, (c) schematic of mass transfer of sodium hydroxide from the continuous phase to the droplet, (d) droplet at reactor outlet.

Since the formation of the aqueous zinc acetate droplets was done in a stream of pure 1-octanol, the addition of a hydroxide source was needed to initiate the zinc oxide synthesis reaction. This was accomplished by the introduction of a sodium hydroxide in 1-octanol stream through a T-junction downstream of the PDMS droplet chip, highlighted in box (b) in Figure 4.1. As diagramed in Figure 4.2(b), the 1-octanol stream containing sodium hydroxide was mixed with the 1-octanol continuous phase that carried the aqueous droplets. The presence of the droplets enhanced the mixing of the two 1-octanol streams due to the creation of recirculating flow patterns [7]. These recirculating patterns introduce flow in the radial direction, enhancing convection driven mixing. The increase in convection in both the continuous and droplet phase also served to increase the heat transfer from the walls of tubing immersed in the hot water bath to the fluid that the tubing contains [160]. The recirculating flow in both phases also helps to eliminate any temperature gradients, creating a uniform temperature field in the fluids.

Once sodium hydroxide was introduced into the continuous phase flow, the sodium hydroxide was able to enter the droplets through convective and diffusive mass transfer. Diagrammed in Figure 4.2(c), the transfer of sodium hydroxide from the continuous phase to the droplet phase was driven by the sodium hydroxide concentration gradient that existed between these two phases. As the sodium hydroxide entered the droplets, the hydroxide ions reacted with the zinc ions already present in the droplets, beginning the synthesis of zinc oxide nanoparticles. Figure 4.2(d) shows a droplet containing free flowing clusters of nanoparticles, entirely contained within the droplet volume. This picture was taken near the outlet of the reactor, corresponding to box (d) in Figure 4.1.

The separation of the formation of droplets from the addition of the 1-octanol containing sodium hydroxide was a necessary design aspect of the reactor. A simpler design would have been

to use the sodium hydroxide in 1-octanol stream to form the aqueous droplets in the PDMS chip, instead of the pure 1-octanol stream. This would have eliminated the need for the T-junction to mix the two streams together. Figure 4.3, though, shows that when the aqueous zinc acetate droplets were formed in a continuous flow of 1-octanol containing sodium hydroxide solids formed at the tip of the needle. The growth of the solids in the red circle in Figure 4.3 interfered with the ability to consistently form the spherical droplets seen in Figure 4.2(a), instead long slugs were formed. By separating the droplet formation step and the addition of the 1-octanol stream containing sodium hydroxide, fouling was prevented on the needle tip.

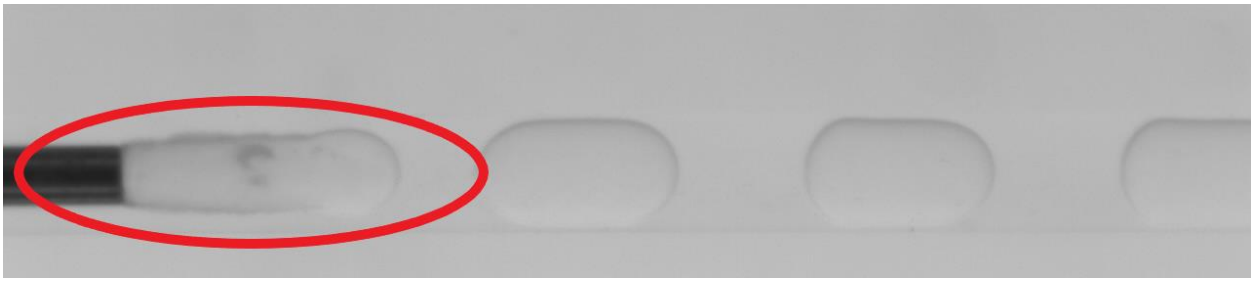

Figure 4.3: Image showing the growth of solid precipitate on the needle tip when a stream of sodium hydroxide in 1-octanol was used as a continuous phase for droplet formation, instead of pure 1-octanol.

4.2 Droplet Behavior

Ideally, the monodispersed droplets formed in the PDMS chip at the reactor inlet would remain as individual droplets through the length of the reactor. Maintaining a uniform droplet volume through the entire length of the reactor would produce an identical reaction environment within each droplet. Comparing the spherical droplets in Figure 4.2(a) to the more slug shaped droplets at the reactor outlet, in Figure 4.2(d), it is obvious that droplet coalescence occurs within the reactor. Due to immersion of the reactor in the hot water bath, it was not possible to observe past approximately the first 0.5 m of the reactor tubing, which prevented visual observation of

where exactly the coalescence occurred. Qualitatively, visual observation of the first 0.5 m of tubing did not show droplet coalescence occurring.

The droplet sensor described in Chapter 3 was used at the reactor outlet to determine if any reaction conditions were causing the observed droplet coalescence. The droplet coefficient of variation was used as a measure for the observed droplet coalescence. The coefficient of variation (CV) is defined as

$$CV = \frac{\sigma}{\mu} \tag{4.1}$$

where σ is the sample standard deviation of 25 measured droplet lengths and μ is the average length of 25 measured droplets. A CV less than 0.1 is considered to be the measure of a monodisperse distribution. The CV of the droplets at the reactor inlet, immediately downstream of the T-junction, was 0.04.

Figure 4.4(a) and (b) shows the how reaction temperature and reagent concentration affected the amount of droplet coalescence in the reactor. Droplet coalescence tended to increase with increasing reaction temperature, the CV of the trials conducted at 60 and 80˚C were greater than twice the CV of the trials conducted at 25 and 40˚C. While the lower temperature trials had a lower CV, these trials were above the CV measured at the reactor inlet. Figure 4.4(b) shows that for the trials with different initial zinc acetate concentrations, all had droplet coalescence occurring. The trial conducted using a zinc acetate concentration of 0.033 M produced the highest CV value of the three trials.

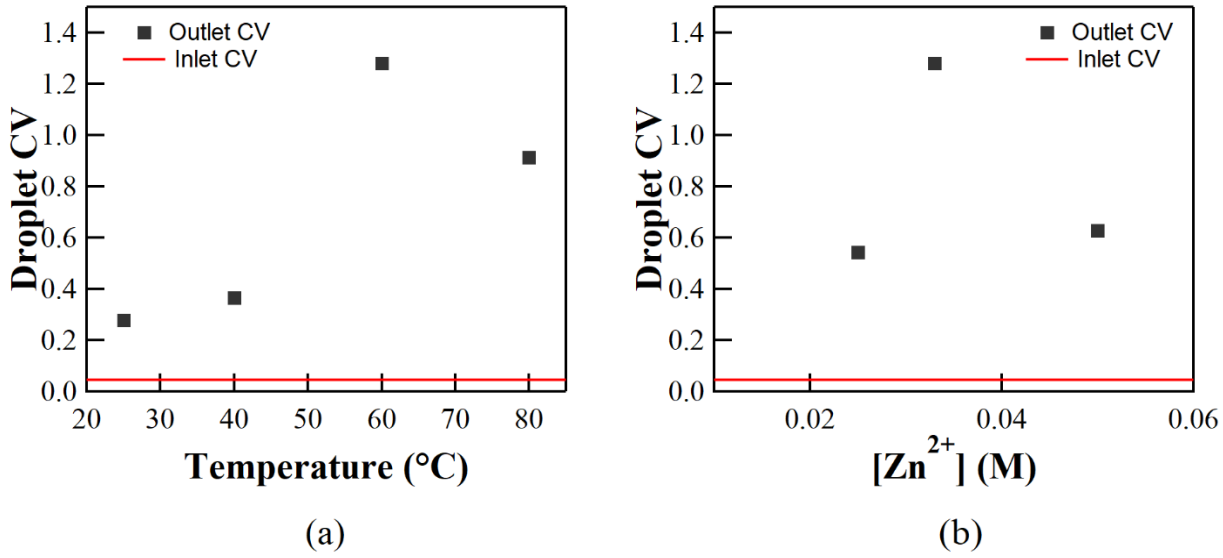

Figure 4.4: (a) Effect of reactor temperature on droplet CV at reactor outlet. Reaction conditions: $[Zn^{2+}]$ = 0.033 M $[OH^-]$ = 0.1 M, τ = 10 min. (b) Effect of inlet zinc concentration on the measured droplet CV. Reaction conditions: $[OH^-]$ = 0.1 M, T = 60˚C, τ = 10 min. Inlet CV line =0.04.

While droplet coalescence occurred for the trials where spherical droplets were used, Figure 4.5 shows that when the droplet volume was increased to produce slug-like droplets, coalescence was prevented. When droplet volumes 0.98 and 1.7 µL were used, the measured droplet CV at the reactor outlet was monodispersed. The droplet volume of 0.21 µL was still prone to coalescence, as shown by the CV of 0.95. The prevention of droplet coalescence when larger droplet volumes were used is most likely due to the larger spacing between droplets that occurred as the larger droplets were formed. A constant flow rate was used for all three trials shown in Figure 4.5. Maintaining a constant inlet aqueous flow rate required a longer time to form larger droplets, decreasing droplet frequency. The decrease in droplet frequency produced an increase in the length between individual droplets, making it more difficult for individual droplets to get close enough to coalesce.

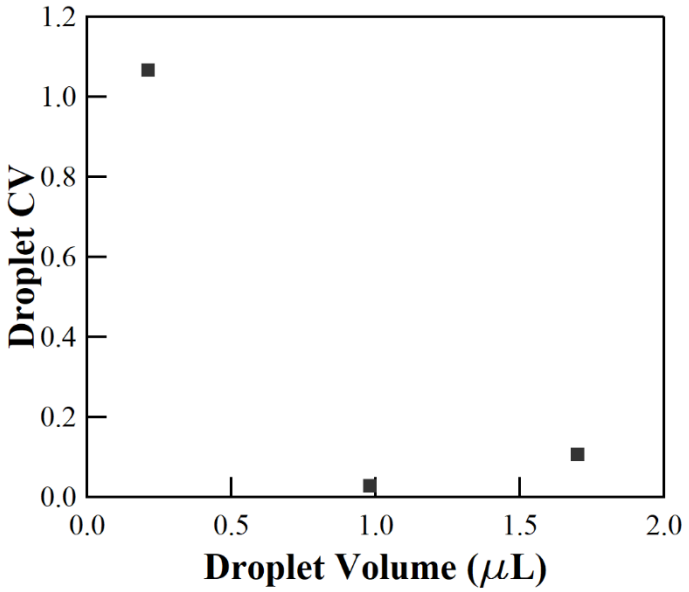

Figure 4.5: Effect of droplet volume on droplet CV at reactor outlet. Reaction conditions: $[Zn^{2+}]$ = 6.3 mM, $[OH^-]$ = 0.025 M, T = 60˚C, τ = 10 min.

As Table 4.1 shows, when the CV of DI water droplets, 0.21 µL droplets at 60˚C, was measured at the reactor outlet the droplet sizes were monodisperse. When a water and 1-octanol interface is formed, as in the case of water droplets in a continuous flow of 1-octanol, the 1-octanol molecules closest to the interface are capable of strong hydrogen bonding. Due to the hydrogen bonding, the hydroxy groups of the 1-octanol molecules become oriented towards the water phase and the alkane chain of the molecules point away from the water phase [9]. The next layer of 1-octanol molecules orients themselves in the opposite direction, forming a bi-layer [171]. The bi-layer of 1-octanol molecules around the water droplet interface may act to inhibit droplet coalescence, similar to the behavior of surfactants.

When a stream of 0.05 M NaOH in 1-octanol was introduced through the reactor's T-junction instead of pure 1-octanol, the droplet CV at the outlet increased to 0.580. Mass transfer to the droplet phase occurred due to the sodium hydroxide concentration difference between the continuous phase and droplet phase. When droplets are in close proximity to each other, coalescence can only occur if the thin film of the continuous phase between the two droplets drains

away [188]. Once the thickness of the film becomes thin enough, van der Waals forces between the two interfaces becomes strong enough to rupture the film [10]. When the film ruptures, the two interfaces join and the droplets merge. Droplet coalescence has been observed in a millifluidic interphase droplet reactor used for the sulfonation of naphthalene [119]. The observed droplet coalescence was attributed to the droplets losing kinetic energy as they translated through the reactor, causing the faster upstream droplets to collide with the slower downstream droplets. The authors stated this behavior would be exacerbated if there was no thin film between the droplet and the tubing wall. In the systems studied in Table 4.1, the addition of sodium hydroxide to the system would need to increase the drag on the droplets for this proposed mechanism to be applicable.

Another possible explanation for the coalescence seen when sodium hydroxide was added to the system is that the mass transfer process induced the droplet coalescence. The effect of mass transfer on droplet coalescence has been studied with moving and stationary droplets [6,17] and also with droplets in extraction columns [157]. When mass transfer into or out of the droplets is occurring as the thin film is draining, the rate of draining can be enhanced or inhibited [31]. Enhancement of the drainage rate occurs when interfacial tension in the thin film region decreases due to the mass transfer of a solute. This creates an interfacial tension gradient which drives fluid flow away from the thin film region, increasing the rate of film drainage. If the opposite situation occurs and high interfacial tension is created in the thin film region due to mass transfer, then the interfacial tension gradient drives flow into the thin film region. This acts to slow or even prevent film drainage. In stationary and moving systems using pairs of droplets, coalescence is enhanced when mass transfer occurs from the droplet to the continuous phase because of the decrease in interfacial tension that occurs [6,17]. The coalescence in these same systems can be greatly reduced

or inhibited when mass transfer occurs from the continuous phase to the droplet phase because of the increase in interfacial tension that occurs [17].

In the cases investigated in Table 4.1, mass transfer occurred from the continuous phase to the droplet phase and an increase in the CV was observed, indicating an increase in droplet coalescence. This may indicate that the mass transfer of sodium hydroxide to the droplet phase produced a decrease in interfacial tension, which drove the coalescence of droplets if they came into close proximity with each other. In systems where the interfacial tension between water and an organic phase has been measured, increasing pH decreases the system's interfacial tension [125–127]. More investigation into the behavior of the interfacial tension of water and 1-octanol while mass transfer of sodium hydroxide is occurring is needed to confirm if that behavior extends to this system.

Table 4.1: Droplet CV at the reactor outlet for system with no mass transfer occurring and with the presence of mass transfer. Droplet volume of 0.21 µL and temperature of 60˚C.

System	Droplet CV
DI water droplets in pure 1-octanol	0.054
DI water droplets with inlet of 0.05 M NaOH in 1-octanol	0.580

Surfactants are often used in droplet-based systems to prevent droplet coalescence. Surfactant molecules will preferentially orient themselves at the droplet interface, with the hydrophilic head positioned in the aqueous phase and the hydrophobic tail in the organic phase. The presence of these molecules on the droplet interface prevents the coalescence with another droplet interface. In order to prevent coalescence, a surfactant interface surface coverage of approximately 90% is needed [124]. Surfactants are also commonly used as capping agents in nanoparticle synthesis to inhibit growth or to induce preferential growth. In the work to be presented later in this dissertation, I investigated the effect of two different surfactant molecules

on zinc oxide nanoparticle synthesis in the interphase droplet reactor. Since it would also be expected that the presence of surfactants would impact the degree of droplet coalescence occurring in the reactor, that data is presented here. The two surfactants used were Triton X-100 and sodium dodecyl sulfate (SDS). Triton X-100 is a large non-polar surfactant molecule while SDS is a smaller anionic surfactant molecule.

As seen in Figure 4.6, the presence of neither Triton X-100 nor SDS in the droplets prevented droplet coalescence from occurring. In both trials where SDS was used, the measured droplet lengths showed increased coalescence compared to the clean trial. When Triton X-100 was used as the surfactant, coalescence was inhibited compared to the clean trial, but was still above the CV value measured at the reactor inlet. Trials using surfactant concentrations higher than 1 mM were not attempted for either surfactant. When higher concentrations were used, it appeared that the surfactants precipitated at the droplet interface, interfering with the ability of the droplet to translate through the reactor. This has been seen when 10 mM Triton X-100 was added to water droplets in 1-octanol, where the Triton X-100 formed a viscous third phase at the interface of the droplet [113]. In droplet rise experiments using a water and 1-octanol system, a 1 mM concentration of SDS was found to produce interfacial coverage approaching 100% while a 1 mM concentration of TX-100 produced coverage approaching 1% [115]. However, despite the tendency of SDS to produce higher interfacial coverage, the observed CV at the reactor outlet was higher when SDS was used. More investigation into the interactions between the surfactant molecules, nanoparticles, and the droplet interfaces is required to determine what is causing this observed behavior.

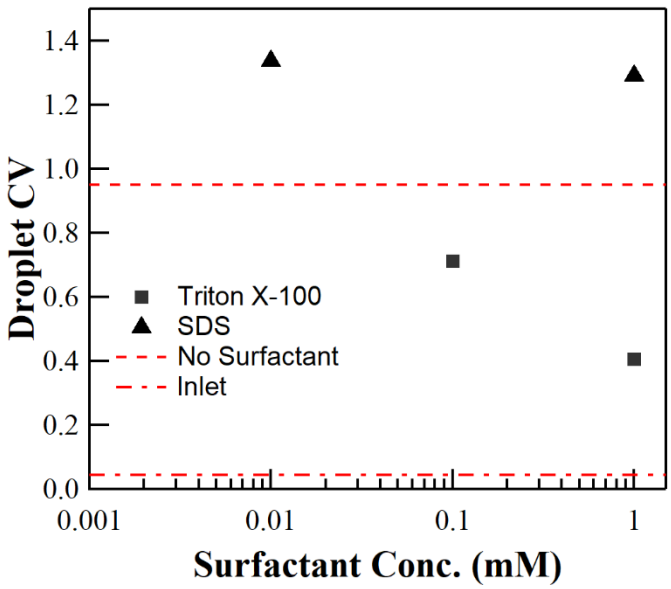

Figure 4.6: Effect of surfactant concentration on droplet CV at reactor outlet using Triton X-100 and SDS. Reaction conditions: $[Zn^{2+}]$ = 6.3 mM, $[OH^-]$ = 0.025 M, T = 60˚C, τ = 10 min.

4.3 Mass Transfer in the Interphase Droplet Reactor

Reagent combination in the interphase droplet reactor is done by the mass transfer of sodium hydroxide from the continuous phase to the droplet phase. The rate of mass transfer into the droplet phase can be affected by the total flow rate, interfacial area, and the presence of surfactants. The rate of reagent addition during batch synthesis of zinc oxide nanoparticles has been observed to affect both particle size and morphology [101]. Determining how different process variables affect the rate of mass transfer is necessary for determining how sensitive the nanoparticle synthesis is to the rate of mass transfer into the droplet. To quantify changes in the rate of mass transfer, the titration method described in Chapter 3 was used. Aqueous droplets containing 0.05 M hydrochloric acid were formed in a flow of 1-octanol. An inlet concentration of 0.1 M sodium hydroxide in octanol was used for all trials. Methyl orange was used as an indicator to track the transfer of sodium hydroxide to the droplets, the color change from red/orange to yellow was assumed to occur at a pH of 4.4 [61].

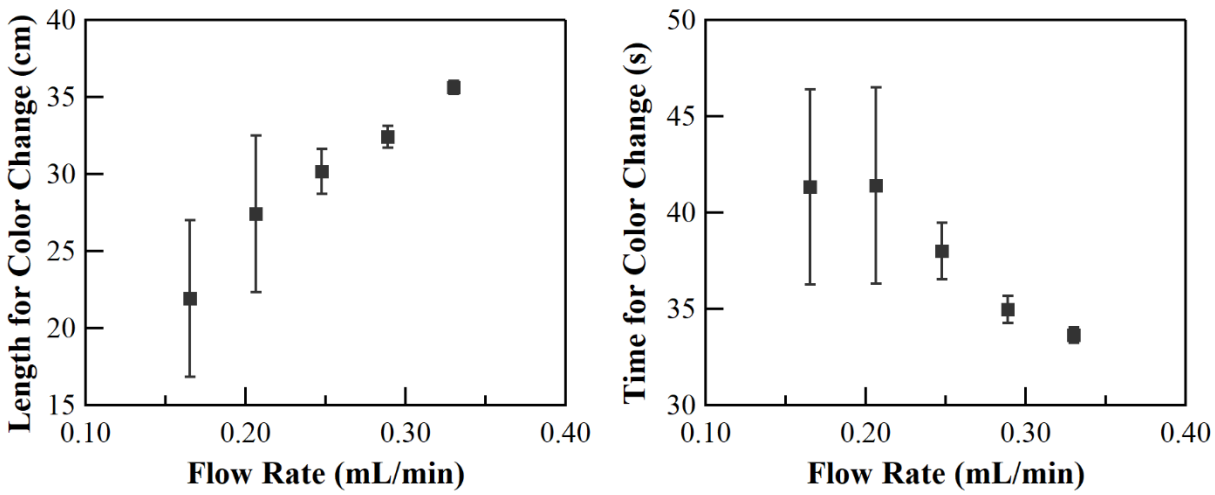

Figure 4.7: (a) Effect of total flow rate on the reactor length required for the indicator color change to occur. (b) Effect of total flow rate on the time required for the indicator color change to occur.

Figure 4.7(a) and (b) shows the effect of total flow rate on the length and time needed for the indicator color change to occur. For all 5 trials, the ratio between the aqueous flow rate and the 1-octanol flow rate was kept constant. As the flow rate was increased, the droplets travelled a longer length through the tubing before the indicator color changed occurred. As expected, when the total flow rate was increased the time required for the indicator color change to occur decreased [27,30,175]. The rate of mass transfer is dependent on the convection present in the system. When droplets are flowing in a continuous phase through a channel, the shear on the droplet interface produces recirculating flow patterns inside the droplet. The presence of droplets in the continuous phase creates similar recirculating flow patterns in the continuous phase as well, as demonstrated in Figure 4.8. As the total flow rate is increased, the convection produced by these flow patterns is increased, producing an increase in the rate of mass transfer [29].

The results shown in Figure 4.7 were for droplets with a volume of approximately 0.27 µL. This droplet volume has a radius equal to the channel radius, yielding a spherical droplet shape. As seen in Figure 4.8, increasing the volume further causes the spherical shape to transition to a

cylindrical slug shape due to the confinement of channel walls. The interface of the spherical droplet is completely exposed to the continuous phase and is available for mass transfer to occur through. The slug shape only has the end caps fully exposed to the continuous phase and a thin film of the continuous phase is present between the aqueous slug and the tubing wall. At low fluid velocities, the thin film becomes depleted and does not significantly contribute to the mass transfer of the system [43,76]. This causes the slugs to have a lower active interfacial area to volume ratio than the spherical droplet. The shape of the slug, though, has a greater contact area with the tube wall which produces shear on the slug interface. The increase in shear relative to the spherical droplet can create an increase in the internal convection of slug, leading to higher rates of mass transfer [29].

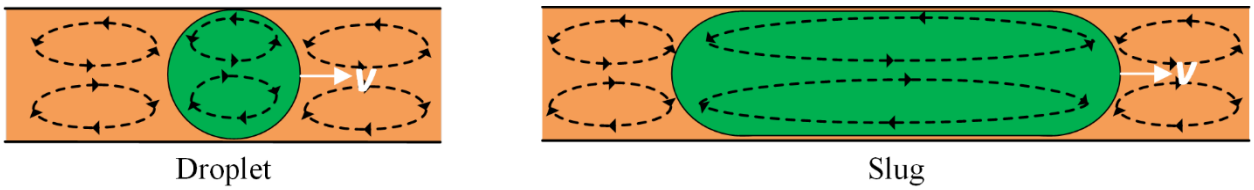

Figure 4.8: Schematic of the shape of droplet versus the shape of slug translating through tubing with a velocity, *v*, along with approximations of fluid flow patterns.

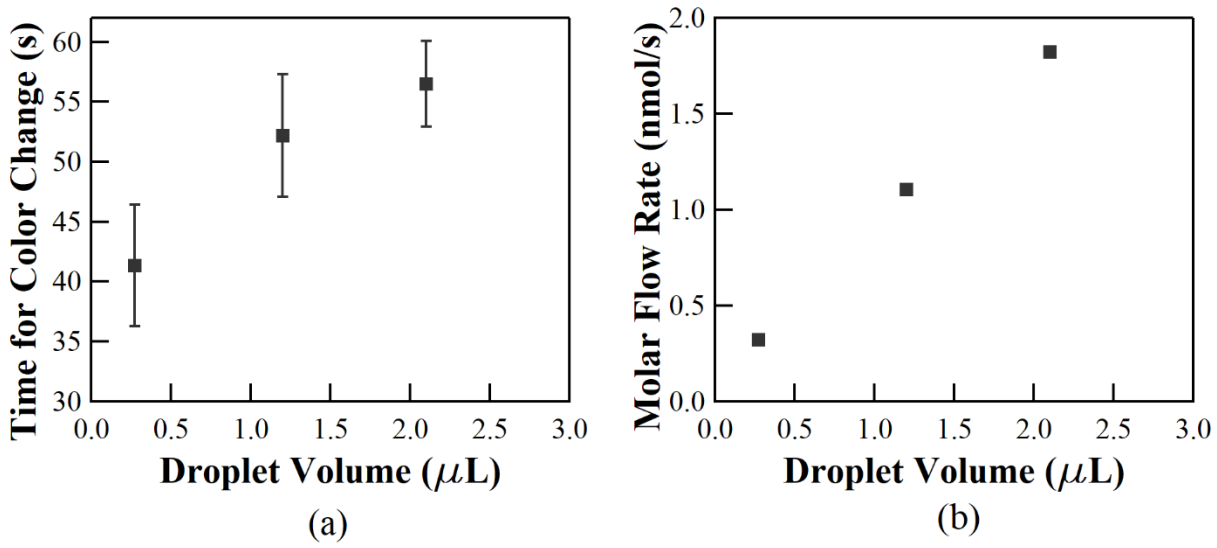

Figure 4.9: (a) Effect of droplet volume on the time required for indicator color change to occur. (b) Effect of droplet volume on the molar flow rate of sodium hydroxide into the droplet phase.

Figure 4.9(a) and (b) show the effects of droplet volume on the time for indicator color change and molar flow rate into the droplet, respectively. Since the H^+ reacts instantaneously with OH^- and with a stoichiometric ratio of 1:1, the rate of the consumption of H^+ inside the droplet was equal to the flow of OH^- into the droplet. The molar flow rate into the droplet used in Figure 4.9(b) was found using Eqn. (4.1),

$$Molar\ Flow\ Rate = \frac{V_d\,\Delta[H^+]}{t} \tag{4.1}$$

where V_d is the droplet volume, $\Delta[H^+]$ is the change in concentration of hydrogen ions from the inlet to the time of the indicator color change, and t is the time for the indicator color change to occur. The $[H^+]$ at the inlet was 0.05 M and $[H^+]$ at the point of indicator color change was assumed to be equal to the pH at which methyl orange transitions from orange to yellow, pH = 4.4 [61].

Figure 4.9(a) shows as the droplet volume was increased, the time required for the indicator color change to occur increased. Figure 4.9(b) shows the molar flow rate of sodium hydroxide into the droplet also increased. The increase in the molar flow of sodium hydroxide into the droplet with increasing droplet volume can be attributed to the greater internal circulation a slug

experiences compared to a spherical droplet. Since the slug was travelling through the tubing at 5 mm/s, the thin film most likely became depleted and did not contribute significantly to the mass transfer [43]. The increase in the molar flow rate of sodium hydroxide, however, did not fully compensate for the increase in moles of H^+ present in the larger volumes of the slug.

The presence of surfactants in a droplet system with interphase mass transfer occurring has typically been associated with a reduction in the rate of mass transfer. The key behavior of surfactant molecules is their tendency to adsorb at the interface of two immiscible liquids. In a droplet interphase mass transfer system, the presence of surfactant molecules at the interface is believed to create a layer of resistance to mass transfer, referred to as the physiochemical effect [77]. For high surfactant concentrations, it is also possible to produce a viscous third phase at the interface which can sharply reduce mass transfer [113].

The ability for surfactants at the interface to modify the circulation within droplets can also decrease mass transfer. When surfactants are present at the interface of a moving droplet, the motion of the interface sweeps the molecules to rear of the droplet. This creates a surfactant concentration gradient across the droplet interface which also creates a gradient in the interfacial tension. The rear high concentration region will have a lower interfacial tension than the front, low concentration region. This creates a Marangoni stress across the droplet interface and can greatly reduce or stop the motion of the interface, preventing internal droplet circulation [13,115]. The presence of the rigid droplet interface reduces the rate of mass transfer due to the decrease in convection [77].

Figure 4.10 shows the mass transfer behavior when different concentrations of either Triton X-100 or SDS where present in the aqueous droplet. A concentration of 0.1 mM SDS was found to inhibit the rate of mass transfer as compared to the clean system. Increasing the concentration

further to 1 mM was found to produce no difference in mass transfer when compared to the clean system. Published experiments studying the effect of SDS on mass transfer in droplet systems show conflicting results. When the mass transfer of acetic acid in carbon tetrachloride droplets falling though a column of water was studied, the presence of 0.1 mM to 1 mM SDS was found to decrease the rate of mass transfer [77]. Similar behavior was observed with the addition of SDS during the transfer of acetone from toluene drops to a column of water [170]. Conversely, when mass transfer into aqueous slugs in a microchannel was studied, the addition of SDS was found to enhance mass transfer compared to a surfactant free system [132]. In this system, trichloroacetic acid was extracted from a continuous phase of hexane into aqueous slugs containing a sodium hydroxide solution, the addition of SDS enhanced mass transfer and increasing the SDS concentration continued to enhance mass transfer. The authors attributed this behavior to Marangoni stress driven flows which enhanced internal droplet mixing. Possibly the behavior seen in Figure 4.10 is a combination of the previously reported observations of the effects of SDS on mass transfer. The 0.1 mM SDS trial experienced the expected inhibited mass transfer due to the presence of SDS. When the concentration was increased to 1 mM, the enhancement of the internal droplet convection countered a portion of the inhibitory effect of SDS.

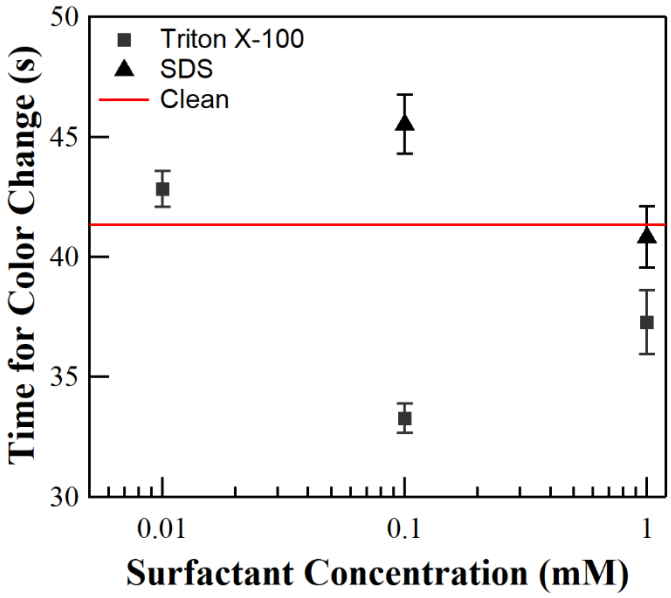

Figure 4.10: Effect of surfactant concentration on the time required for indicator color change to occur for Triton X-100 and SDS.

When Triton X-100 was introduced to the droplet phase, the 0.01 mM trial produced a slight decrease in the rate of mass transfer. Both 0.1 mM and 1 mM trials had an increase in the rate of mass transfer compared to the clean system. The 1 mM TX-100 trials did induce some precipitation of the sodium hydroxide out of the continuous phase. Care was taken, however, to ensure that the tubing walls were not fouled when the distance at which the indicator color change occurred was measured. The precipitation behavior was not observed with the two lower concentrations. The enhancement of mass transfer versus the clean system is in contrast to the published work on mass transfer in droplet rising/falling experiments that used TX-100. The addition of Triton X-100 in these mass transfer experiments was found to inhibit mass transfer [77,114,128]. Triton X-100's ability to inhibit mass transfer in droplets can be slightly diminished at concentrations above 0.04 mM due to surface remobilization, but the rate of mass transfer is still slower than that of a clean system [77]. The interface of a water droplet in a continuous phase of 1-octanol is a complex system. When only water and 1-octanol are present, the 1-octanol tends to form a bi-layer structure. When concentrations of TX-100 between 1 and 10 mM are used in an

aqueous droplet phase, it is possible to form a viscous third phase at the interface consisting of TX-100 micelles, which would produce a decrease in the rate of mass transfer [113,114].

Most of the published work on how surfactants affect mass transfer in droplet systems has been conducted with either stationary droplets or with droplets undergoing buoyancy driven motion. Limited work has been done with confined droplets in pressure driven systems. The internal flow patterns and surfactant behavior that develop in droplets are different for buoyancy driven motion and confined pressure driven motion. When surfactants are present in droplets experiencing buoyancy driven motion, the surfactants will accumulate at the rear of the droplet [23]. When surfactants are present in droplets experiencing pressure driven motion, the surfactants will accumulate at the rear of the droplet but also at flow stagnation points at the front of the droplet and along the sides of the interface [13].

In the microfluidic mass transfer system mentioned previously, the addition of SDS was observed to enhance mass transfer as compared to a clean system [132]. Surfactant enhancement of mass transfer was also seen in a microfluidic system using CTAB as a surfactant [65]. For both the SDS system and the CTAB system, the increase in mass transfer was attributed to an increase in internal droplet convection caused by the Marangoni effect. For the CTAB system, the proposed mechanism stated that the Marangoni effect created smaller recirculatory patterns along the interface which were more efficient at mixing than the larger recirculatory flow patterns present in clean droplets. As described earlier, the Marangoni effect creates flow in the opposite direction of the shear induced flow at the droplet interface. The presence of flow occurring in opposite directions would have to be responsible for the establishment of the smaller, more efficient recirculatory flow patterns. In general, however, the Marangoni effect is associated with a decrease in internal droplet convection [13]. Ascribing the enhancement in mass transfer seen with the

addition of surfactants entirely to an increase in convection caused by the Marangoni effect appears to be counterintuitive. Despite these inconsistencies, it may be possible that the behavior of mass transfer with the addition of surfactants in the confined space of microfluidic and millifluidic droplet reactors differs from the unconfined droplet rise/fall experiments. Due to the complexities of the water/1-octanol interface, it may also be possible that the effects seen in Figure 4.10 are system specific. Further investigation is required to determine the mechanism behind the observed enhancement in mass transfer in Figure 4.10 when Triton X-100 was added to the droplet phase.

Chapter 5: Synthesis of Zinc Oxide Nanoparticles in an Interphase Droplet Reactor

Zinc oxide nanoparticles were synthesized using the interphase droplet reactor described in Chapters 3 and 4. Aqueous droplets of zinc acetate were formed in a continuous flow of 1-octanol. The downstream introduction of sodium hydroxide into the continuous phase supplied the source of hydroxide ions for the hydrolysis of zinc acetate. As the droplets translated through the reactor the mass transfer of the sodium hydroxide to the droplet phase initiated the synthesis of zinc oxide. In the following sections the effect of changing reaction temperature, reactant concentrations, and the residence time on the size, shape, and particle size distribution of the synthesized nanoparticles is discussed. In Chapter 4, the total flow rate of the system and the droplet size were shown to affect the rate of mass transfer into the droplet phase. The effect of changing these parameters on the nanoparticle synthesis is also discussed. Unless otherwise noted, the reaction parameters used were: zinc acetate concentration, $[Zn^{2+}]$ = 0.033 M, sodium hydroxide concentration, $[OH^-]$ = 0.1 M, total flow rate, Q = 0.165 ml/min, residence time, τ = 10 min, and temperature, T = 60˚C.

5.1 Effect of Reaction Temperature

The interphase synthesis of zinc oxide showed clear dependence on the reaction temperature. The reaction temperature directly affects both the rate of mass transfer from the continuous phase and the synthesis kinetics. Figure 5.1 shows the effects of reaction temperature on the nanoparticle morphology. A reaction temperature of 25˚C produced only plate-like particles with lengths that were over 500 nm. Increasing the temperature to 40˚C changed the morphology to primarily spherical particles, however, some plate like particles were still present in the collected

product. Reaction temperatures of 60˚C and 80˚C produced very similar morphologies and at both temperatures no plate-like particles were seen in the SEM micrographs. The increase in reaction temperature produced an increase in the reaction kinetics. Faster reaction kinetics favor faster nucleation, which tends to produce spherical nanoparticles. Figure 5.2 shows droplets at the end of the interphase droplet reactor with free-flowing clusters of solid particles visible. The volumes of the droplets were larger than the initial droplet volumes due to the merging behavior discussed in Chapter 4. Reaction temperatures 25-60˚C produced a film on the droplet interface which may have been a salt that precipitated. At 80˚C there is no film visible, perhaps indicating that the solubility of the solid producing the film had been increased by the higher reaction temperature. When the reaction temperature was increased from 40 to 60˚C, the image shows a visual increase in the apparent quantity of particles circulating in the droplets. The image of the droplet for the 40˚C trial shows a small circulating loop of particles at the front of the droplet while the droplet for the 60˚C trial appears to have a much larger fraction of its volume occupied by particles.

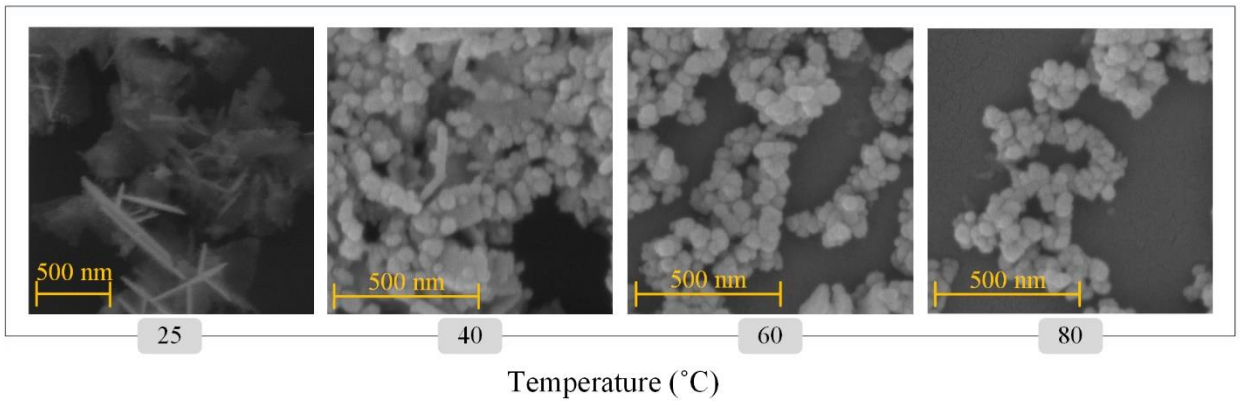

Figure 5.1: SEM micrographs showing the effect of temperature on the morphology of zinc oxide nanoparticles. Zinc acetate concentration was 0.033 M and sodium hydroxide concentration was 0.1 M.

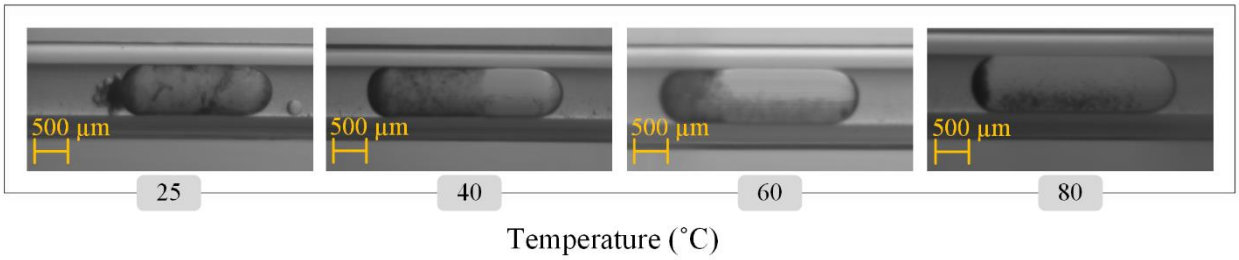

Figure 5.2: Images of droplets exiting the interphase droplet reactor for reaction temperatures 25 - 80˚C.

The size of the particles synthesized at 25˚C were not analyzed since the highly aggregated and overlapping placement of the plates made image analysis extremely difficult. Figure 5.3 shows the particle size distributions for the reaction temperatures 40˚C and above and Table 5.1 provides the size distribution statistics. The size measurements for the reaction temperature at 40˚C were not taken on any plate-like particles, only the more spherical particles were measured. Increasing the temperature from 40 to 60˚C produced an increase in the average particle diameter. The reaction kinetics would have been increased as the reaction temperature increased which promotes faster nucleation and the formation of spherical particles [101]. The plate-like morphology produced from reaction temperatures at 25˚C has been reported previously in various aqueous batch systems. Plate-like particles have been reported after a batch reaction time of 15 minutes using zinc nitrate as a precursor at a pH of 10.5 [109]. Reaction times of 2 hours converted the plate-like particles into star shapes. Using a pH of 11, zinc sulfate as a precursor, and a $[Zn^{2+}]$:$[OH^{-}]$ ratio of 1:4, another report still produced plate-like particles after a reaction time of 2 hours [101]. The morphology of the product produced at 25˚C appears to be very sensitive to the system used.

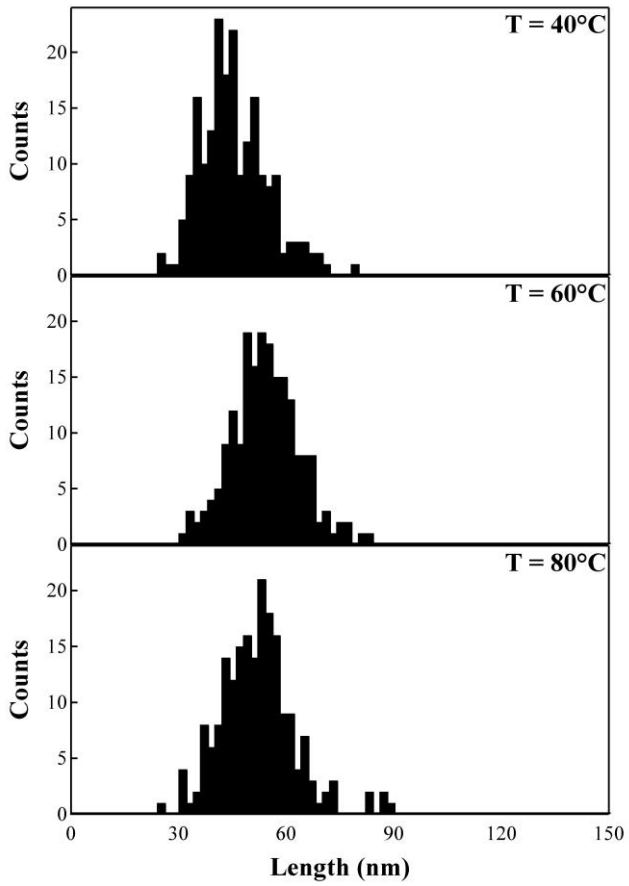

Figure 5.3: Particle size distributions for nanoparticles synthesized at 40, 60 and 80 °C, n = 200.

Table 5.1: Particle size distribution statistics for nanoparticles synthesized at 40, 60, and 80 °C, n = 200.

Temperature (°C)	Mean (nm)	Std. Dev. (nm)	CV
40	45	9	0.21
60	54	10	0.18
80	52	11	0.20

There are factors that favor the formation of the plate morphology at lower reaction temperatures. A lower reaction temperature produces a lower reaction and nucleation rate, which causes fewer zinc oxide nanoparticles to be initially precipitated. This leaves more $Zn(OH)_4^{2-}$ in solution to provide material for subsequent growth to occur [101,146]. Growth of the ZnO sheets has been reported to occur parallel and perpendicular to the *c*-axis of the wurtzite crystal structure

[168]. This creates sheets with an exposed, non-polar, $(10\bar{1}0)$ surface. Hierarchical growth can occur off a primary sheet, forming ordered sheet structures. Secondary sheets have been observed to grow off a primary sheet at a 60˚ angle, corresponding to the hexagonal crystal structure of zinc oxide [168]. Figure 5.4 shows an assembly of sheets formed at 25˚C that were aligned parallel to viewing angle of SEM. The angles highlighted in the SEM micrograph have an approximate angle of 60˚.

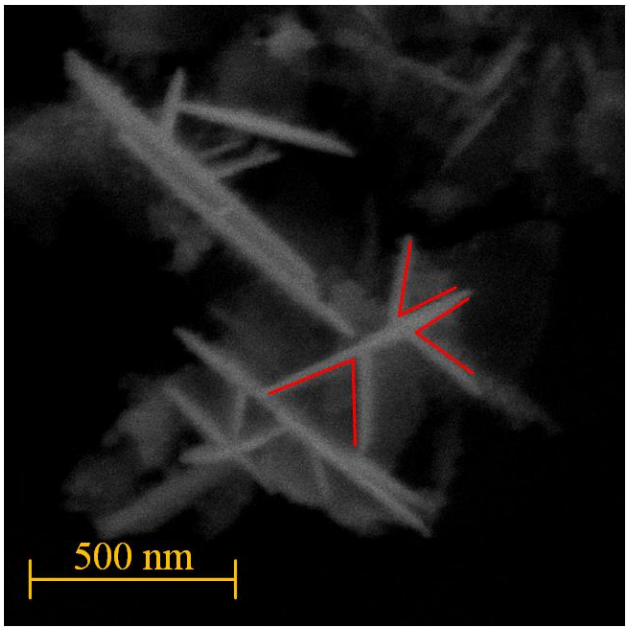

Figure 5.4: SEM micrograph of zinc oxide nanosheet formed from reaction temperature of 25˚C. Red lines highlight the 60˚growth angle of the secondary sheets.

To confirm that $Zn(OH)_2$ was not formed, thermogravimetric analysis was conducted on the products produced from the different reaction temperature trials. Figure 5.5(a) shows the thermogravimetric analysis of the zinc oxide nanoparticles synthesized at different reaction temperatures. As seen in Figure 5.5(a), mass loss that occurred between room temperature and approximately 120˚C can be attributed to the loss of unbounded water. Mass loss occurring between approximately 120 and 150˚C is typically attributed to the conversion of $Zn(OH)_2$ to ZnO

and additional mass loss at higher temperatures is due to the loss of surface hydroxyl groups [101]. The samples from all reaction temperatures showed no significant mass loss from 100 to 200˚C. This suggests that all the synthesized nanoparticles are predominantly ZnO. The XRD patterns of the nanoparticles synthesized at all four temperatures seen in Figure 5.5(b) also confirms this, all peaks are consistent with the wurtzite crystal structure for ZnO. No peaks that could be attributed to the presence of $Zn(OH)_2$ are seen in Figure 5.5(b). Figures 5.6(a) and (b) show the positions of the prominent peaks for the stable ε-$Zn(OH)_2$ phase and the metastable phase β-$Zn(OH)_2$. Figure 5.7(a) shows the EDS spectrum for the ZnO nanoparticles synthesized at 60˚C while Figure 5.7(b) shows the quantitative results for the particles analyzed at all four temperatures. The EDS X-ray spectrum shows that the product is composed of zinc and oxygen. The excess oxygen can be attributed to the presence of oxygen bearing surface species whose presence was seen in the thermogravimetric analysis as well.

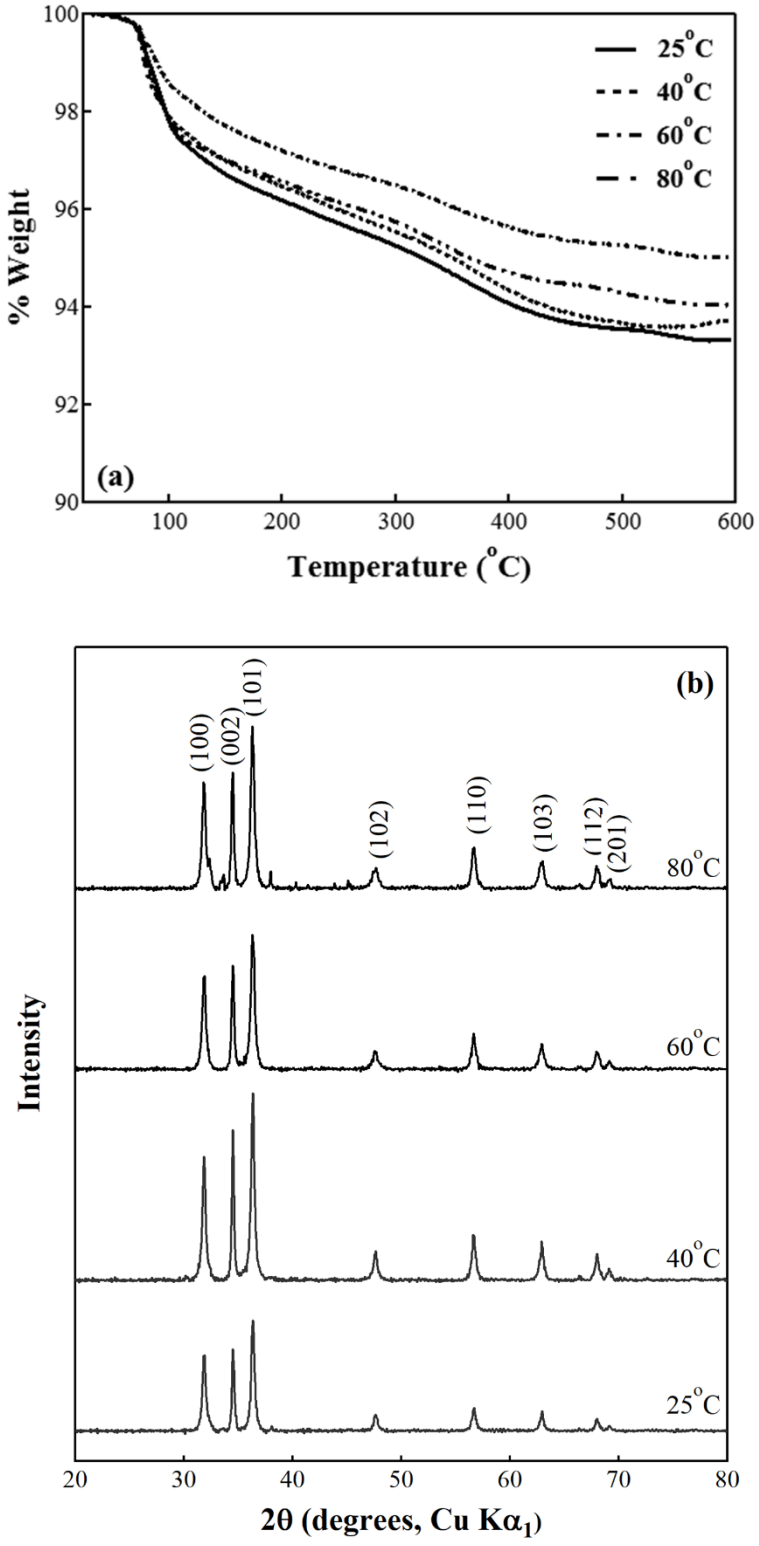

Figure 5.5: (a) Thermogravimetric and (b) XRD data for zinc oxide nanoparticles synthesized at different reaction temperatures 25, 40, 60, and 80˚C.

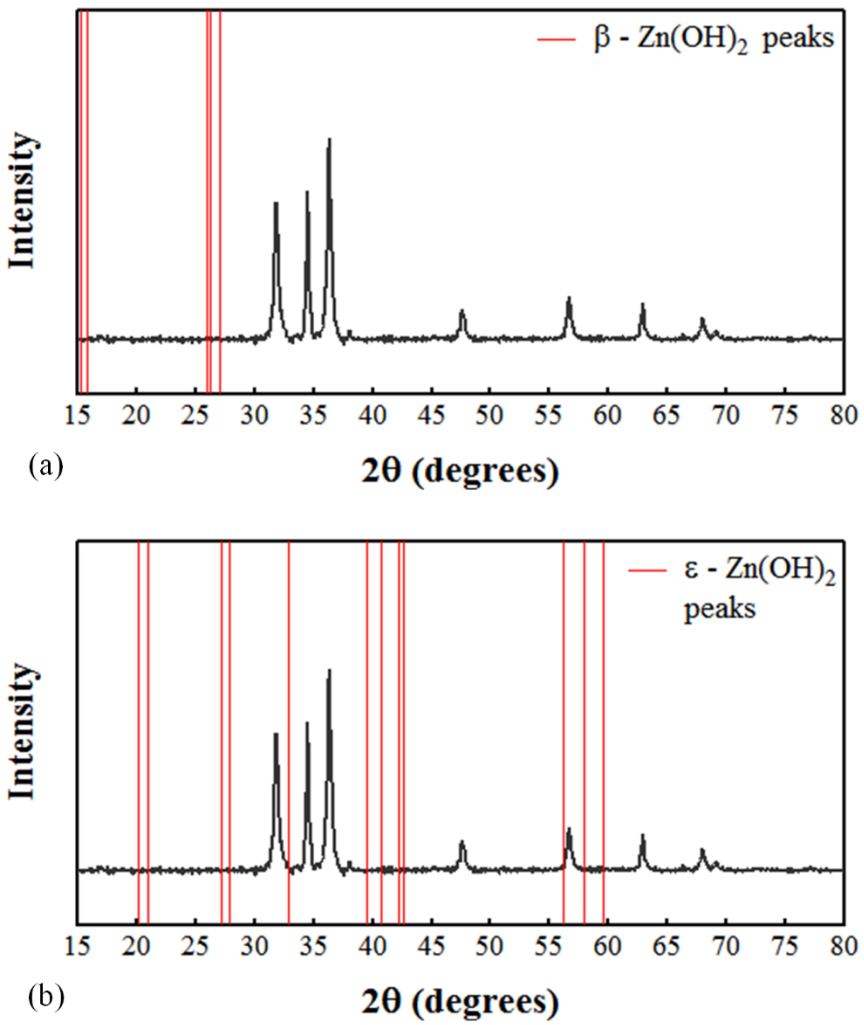

Figure 5.6: (a) XRD pattern for zinc oxide with the superimposed peak positions of β-$Zn(OH)_2$. (b) XRD pattern for zinc oxide with the superimposed peak positions of ε-$Zn(OH)_2$.

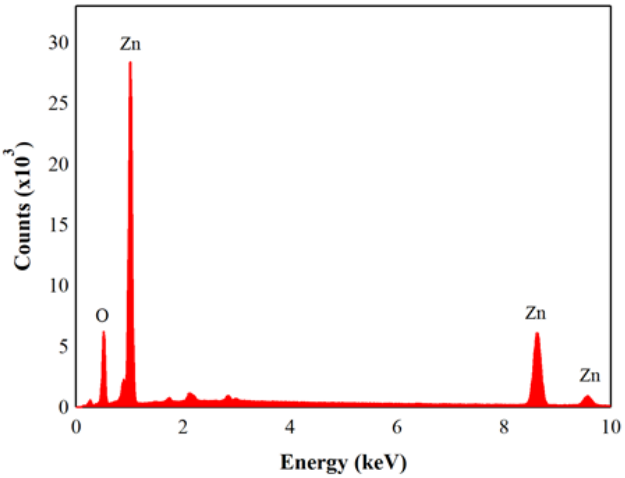

(a)

Temperature (˚C)	Zn (Atomic %)	O (Atomic %)
25	51.77	48.23
40	40.56	59.44
60	45.06	54.94
80	48.54	51.46

(b)

Figure 5.7: (a) EDS X-ray spectrum for zinc oxide synthesized at 60˚C and (b) elemental concentrations at different reaction temperatures 25, 40, 60, and 80˚C.

5.2 Effect of Zinc Acetate Concentration

The concentration of the zinc acetate solution in the droplet phase was changed from 0.025 M to 0.075 M at a reaction temperature of 60ºC and a continuous phase sodium hydroxide concentration of 0.1 M. The SEM micrographs for all the synthesized nanoparticles for the various zinc acetate concentrations in Figure 5.8 show spherically shaped particles. The corresponding particle size distribution statistics are shown in Table 5.2. A zinc acetate concentration of 0.025 M yielded smaller particles on average, 50 nm, while a concentration of 0.075 M yielded the largest particles, 62 nm, of all the trials conducted with a residence time of 10 minutes. While concentrations of 0.033 M and 0.050 M produced similarly sized particles, using 0.033 M zinc

acetate produced particles with a narrower size distribution. The small mean particle size obtained from the zinc acetate concentration of 0.025 M was most likely caused by the more rapid and complete consumption of the Zn^{2+} which would have limited the amount of subsequent growth occurring after nucleation [104]. A high ratio of OH^- : Zn^{2+} drives the reaction towards the formation of ZnO, the lower the ratio, the more favorable it is for $Zn(OH)_2$ to be produced [101]. Figure 5.9 shows the XRD data for the different zinc acetate concentrations studied. The XRD data for the 0.075 M trial only showed peaks that are consistent with the zinc oxide wurtzite structure. The increase in particle size that occurred as the zinc acetate concentration increased may be due to more growth species remaining in solution. The presence of additional $Zn(OH)_4^{2-}$ in solution would allow for subsequent growth to occur after nucleation, increasing the average nanoparticle size.

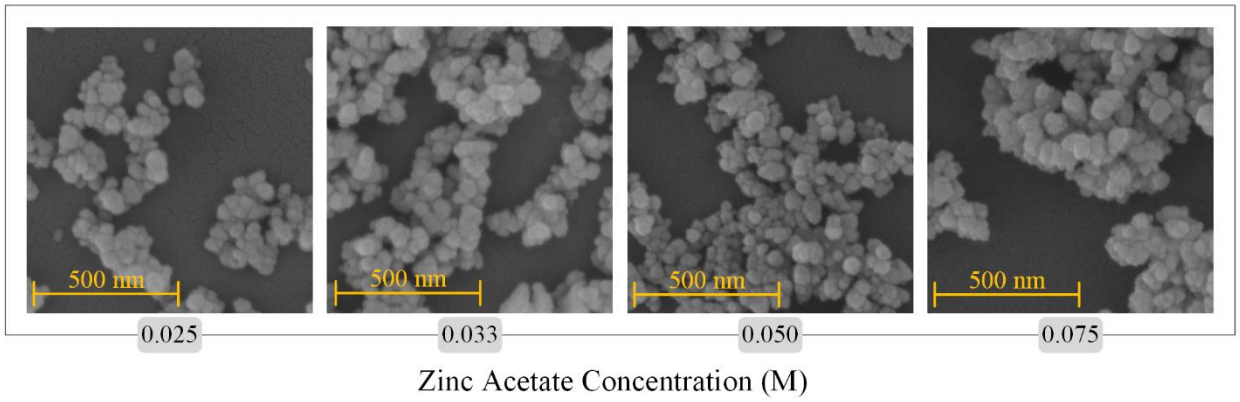

Figure 5.8: SEM micrographs showing the effect of zinc acetate concentration on nanoparticle morphology. The reaction temperature was 60˚C and the sodium hydroxide concentration was 0.1 M.

Table 5.2: Particle size distribution statistics for nanoparticles synthesized from zinc acetate concentrations of 0.025, 0.033, 0.050 and 0.075 M, n = 200.

$[Zn^{2+}]$ (M)	Mean (nm)	Std. Dev. (nm)	CV
0.025	50	10	0.20
0.033	54	10	0.18
0.050	55	11	0.20
0.075	62	16	0.26

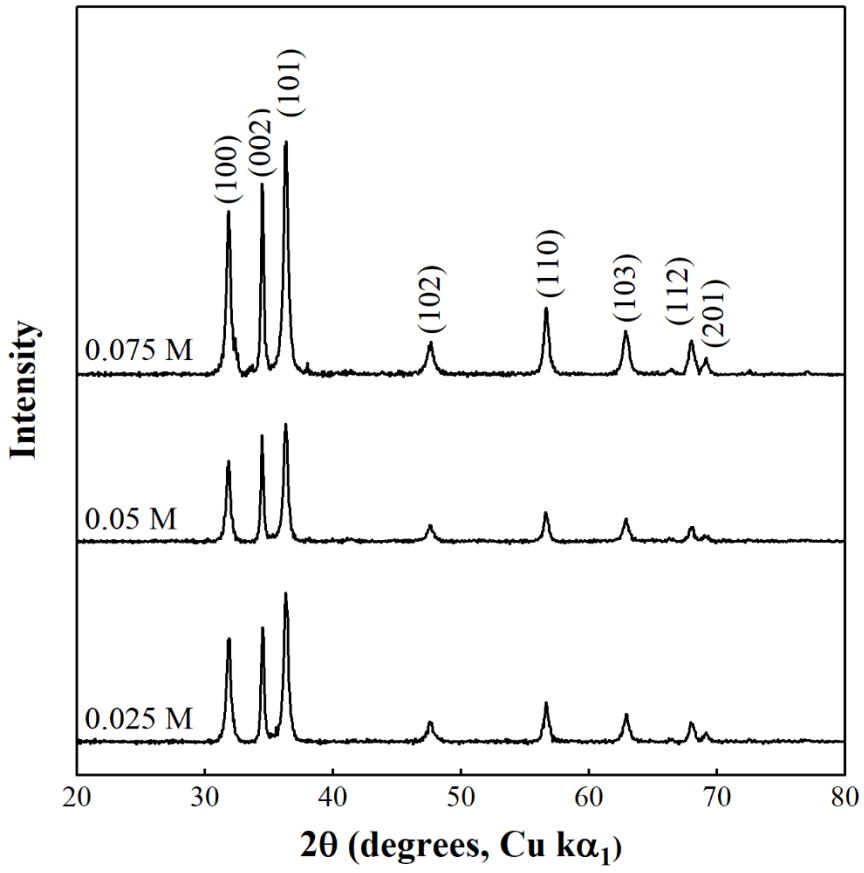

Figure 5.9: XRD data for trials conducted using an inlet sodium hydroxide concentration of 0.1 M and different zinc acetate concentrations. Reaction temperature was 60˚C and residence time was 10 minutes.

5.3 Effect of Hydroxide Concentration

Changing the sodium hydroxide concentration in the continuous flow of 1-octanol increased the mass transfer driving force between the continuous and droplet phase. Higher concentrations of hydroxide ions can have a catalytic effect on the synthesis of zinc oxide, promoting more rapid conversion of the reaction intermediaries [101]. Figure 5.10 shows the effect of increasing the sodium hydroxide concentration from 0.1 M to 0.5 M on the nanoparticles synthesized using a zinc acetate concentration of 0.05 M and a reaction temperature of 60˚C. Increasing the sodium hydroxide concentration had drastic effects on the morphology of the resulting particles. As shown in Table 5.1, a sodium hydroxide concentration of 0.1 M produced spherically-shaped particles with an average size of 55.0 nm. Increasing the sodium hydroxide to 0.3 M produced primarily plate-like particles, while some spherical-shaped particles are present. Figure 5.11 shows the XRD data for the 0.3 M trial, only peaks attributable to ZnO are present. Increasing the concentration further to 0.5 M produced primarily plate-like particles, however, these particles were smaller than those produced at 0.3 M.

Hydroxide ions can adsorb onto the surface of nanoparticle, encouraging anisotropic particle growth [177]. The plates seen in Figure 5.10 are also highly agglomerated, indicating that dissolution of the solid ZnO was possibly occurring. The solubility of ZnO increases with increasing pH [8]. Increasing the inlet sodium hydroxide concentration in the continuous phase would have served to increase the final pH of the droplet phase. When an inlet sodium hydroxide concentration of 0.3 M was used, the ratio between the zinc acetate concentration and the sodium hydroxide concentration was 1:6. Similar agglomeration behavior was observed when an inlet sodium hydroxide concentration of 0.1 M was used with a zinc acetate concentration of 0.0167 M, a $[Zn^{2+}]$: $[OH^{-}]$ ratio of 1:6. Figure 5.12 shows the agglomerated particles formed from that trial.

While sodium hydroxide is necessary for the formation of ZnO nanoparticles, and can even act as a catalyst for the reaction, a high excess can cause the dissolution of the synthesized nanoparticles.

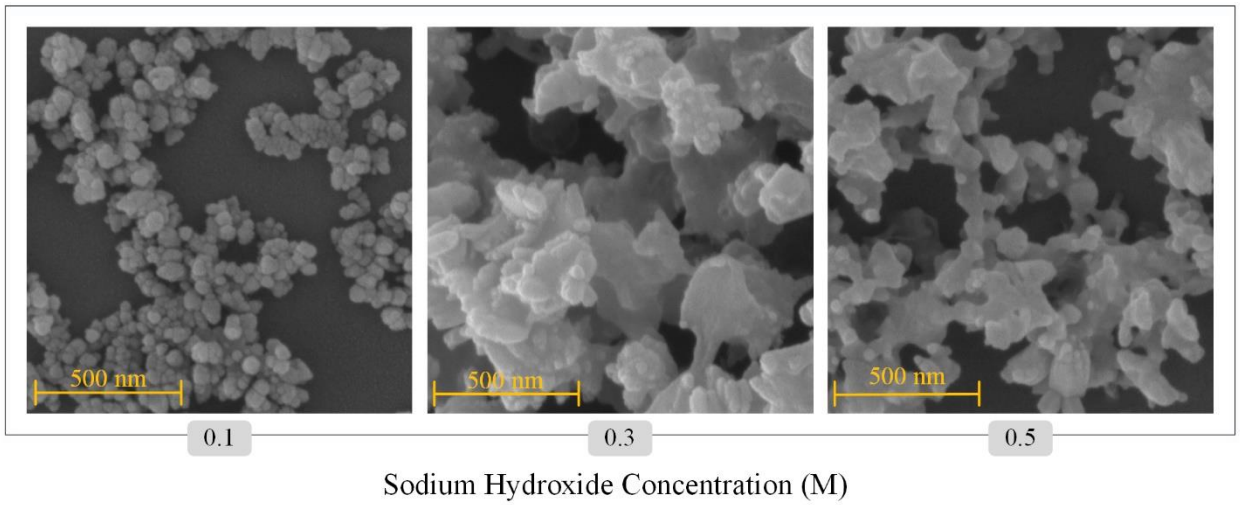

Figure 5.10: SEM micrographs showing the effect of sodium hydroxide concentration on zinc oxide nanoparticle morphology. The reaction temperature was 60˚C and the zinc acetate concentration was 0.05 M.

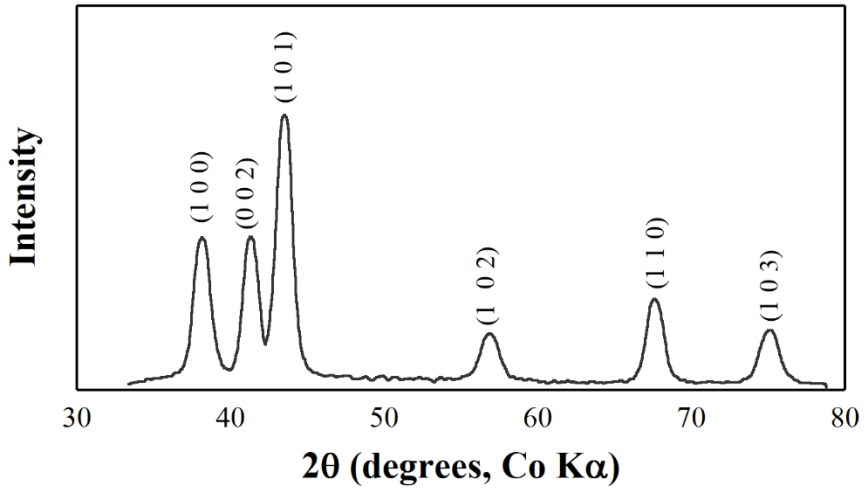

Figure 5.11: XRD data for the products produced from the use of an inlet sodium hydroxide concentration of 0.3 M.

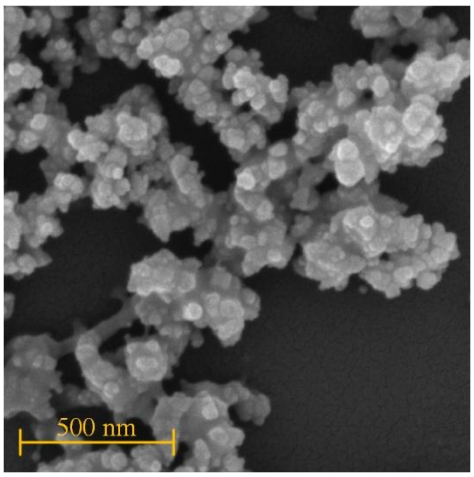

Figure 5.12: SEM micrograph for particles produced with a zinc acetate concentration of 0.0167 M and an inlet sodium hydroxide concentration of 0.1 M. Reaction temperature was 60˚C and residence time was 10 minutes.

5.4 Effect of Residence Time

The effect of residence time was investigated at a constant total flow rate of 0.165 mL/min by using three different reactor lengths. Figure 5.13 and Table 5.3 show the effect of changing residence time on the particle morphology and size distribution for a reaction temperature of 60˚C, zinc acetate concentration of 0.033 M, and sodium hydroxide concentration of 0.1 M. As the residence time was increased from 5 minutes to 10 minutes, the mean particle size increased from 42 nm to 54 nm due to increased time for particle growth. As the residence time was increased from 10 minutes to 20 minutes, the mean particle size decreased and the size distribution narrowed.

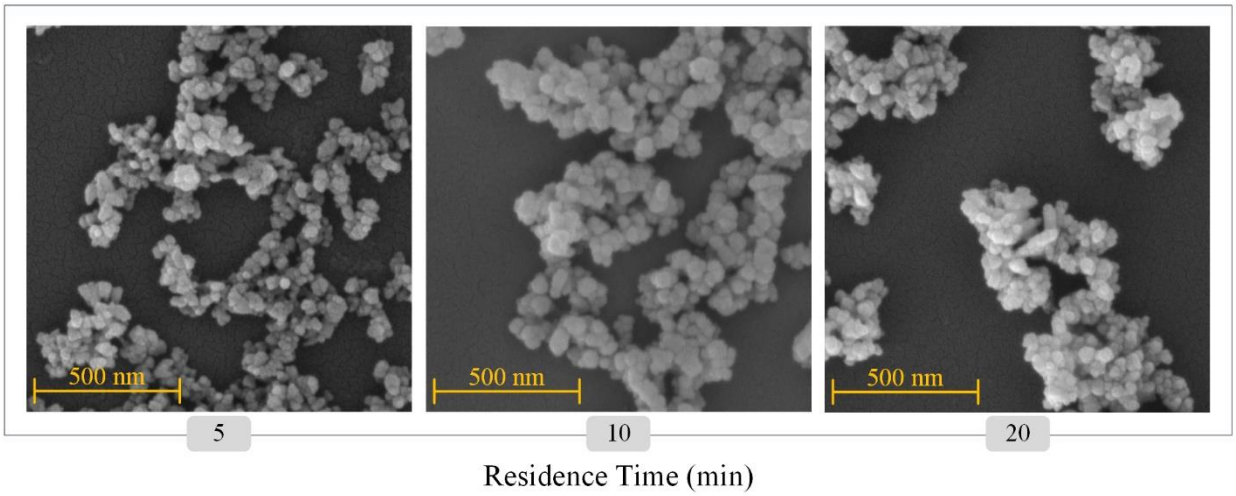

Figure 5.13: SEM micrographs showing the effect of reactor residence time on zinc oxide nanoparticle morphology. The reaction temperature was 60˚C and the zinc acetate concentration was 0.033 M, sodium hydroxide concentration was 0.1 M and the total flow rate was 0.165 mL/min.

Table 5.3: Particle size distribution statistics for nanoparticles synthesized in a reactor using either a 5minute, 10-minute, or a 20-minute residence time, n = 200.

τ (min)	**Mean (nm)**	**Std. Dev. (nm)**	**CV**
5	42	11	0.26
10	54	10	0.18
20	50	8	0.16

5.5 Effect of Total Flow Rate

The effect of total flow rate was investigated at a constant residence time of 10 minutes, accomplished by using two different reactor lengths. Figure 5.14 shows the SEM micrographs for zinc oxide nanoparticles synthesized at 0.165 mL/min and 0.330 mL/min with zinc acetate concentration of 0.033 M, sodium hydroxide concentration of 0.1 M, and a reaction temperature of 60˚C. The corresponding particle size statistics for the spherical particles are shown in Table 5.4. As seen in Figure 5.14, as the flow rate was increased, there was the appearance of plate and rod like particles mixed with spherical particles. Table 5.4 also shows that the polydispersity of the nanoparticle size increased with increasing flow rate. As the total flow rate increases, the

convection within the droplet also increases. The increased convection may lead to more particle collisions, creating aggregated structures. This behavior has been observed in single-phase laminar flow synthesis of zinc oxide nanoparticles when recirculating flow patterns, Dean vortices, were present [19]. Recirculating flow patterns also exist inside a translating droplet and as the total flow rate of the system was increased, the velocity of the circulatory flow also increased. This behavior may have led to a similar convection driven aggregation of zinc oxide nanoparticles in the droplets.

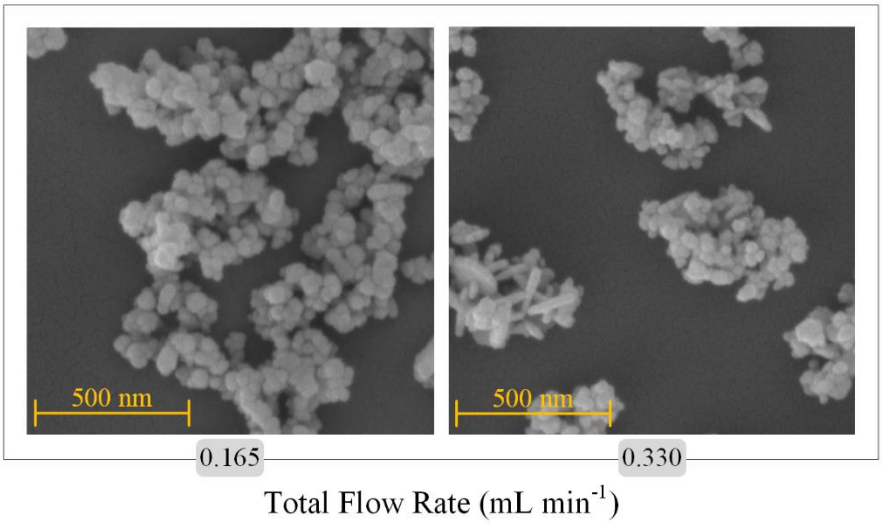

Figure 5.14: SEM micrographs showing the effect of total flow rate on zinc oxide nanoparticle morphology. The reaction temperature was 60˚C and the zinc acetate concentration was 0.033 M, sodium hydroxide concentration was 0.1 M.

Table 5.4: Particle size distribution statistics for nanoparticles synthesized using flow rates of 0.165 and 0.330 mL/min, n = 200.

Flow Rate (mL/min)	**Mean (nm)**	**Std. Dev. (nm)**	**CV**
0.165	54	10	0.18
0.330	52	12	0.23

Increasing the total flow was also shown in Chapter 4 to increase the rate of sodium hydroxide mass transfer into the droplet phase. A decrease of 18% in the time required for the indicator color change to occur was observed. The increase in the rate of mass transfer would have favored more rapid nucleation, which would have produced smaller nanoparticles. The particle size for the 0.330 mL/min trial showed a negligible decrease when the flow rate was increased. The particle size for synthesis using 0.033 M Zn and 0.1 M sodium hydroxide concentrations does not appear to be highly sensitive to the increase in convective driven mass transfer caused by doubling the flow rate.

5.6 Effect of Initial Droplet Volume

The effect of changing the initial droplet volume was investigated using three different droplet volumes. In order to maintain a constant total flow rate for all three trials, different drop formation geometries were used, as seen in Figure 5.15. The 0.044 µL droplets were formed by centering the dispensing needle in a 450 µm diameter channel, which created a flow focusing geometry. The 450 µm channel then expanded into an 800 µm channel and droplets with radii smaller than the channel radius were formed. Due to the greater density of water compared to 1-octanol, the 0.044 µL droplets settled to the bottom of the tubing. The 0.25 and 1.13 µL droplet volumes were formed using a co-flow geometry. The 1.13 µL droplets were formed by using a larger dispensing needle and channel diameter. The 1.13 µL then translated into the 800 µm diameter reactor tubing, forming elongated slugs.

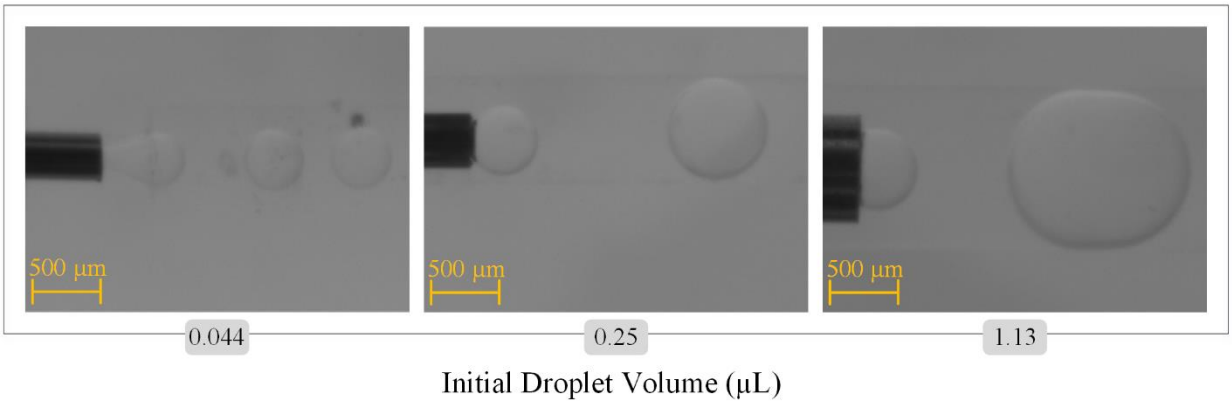

Figure 5.15: Formation of aqueous droplets of zinc acetate in a continuous flow of pure 1-octanol. Aqueous phase flow rate is 0.015 mL/min and the 1-octanol continuous phase flow rate is 0.075 mL/min for all three images.

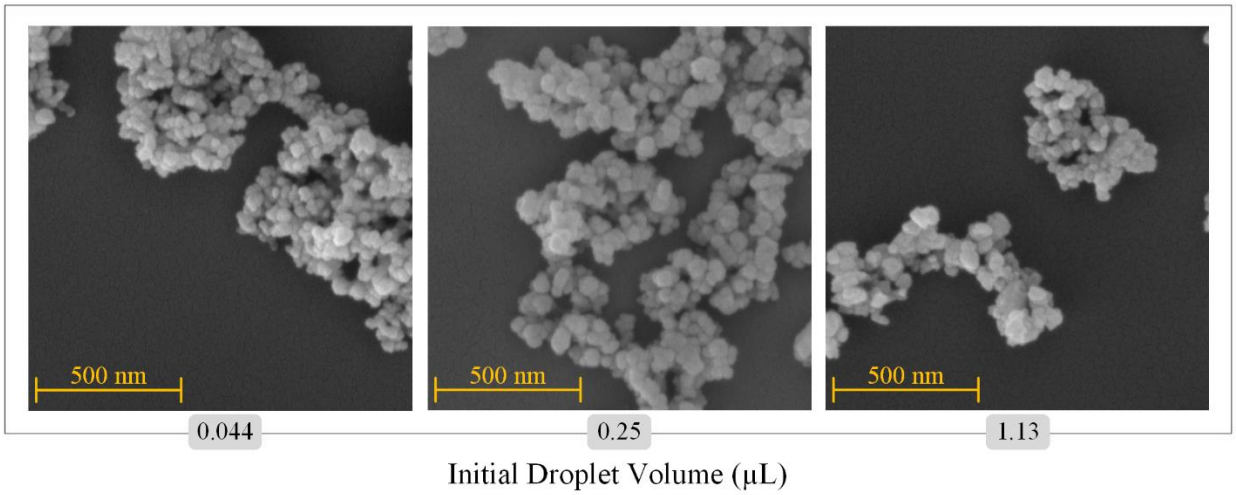

Figure 5.16: SEM micrographs showing the effect of initial droplet volume on zinc oxide nanoparticle morphology. The reaction temperature was 60˚C and the zinc acetate concentration was 0.033 M, sodium hydroxide concentration was 0.1 M and the total flow rate was 0.165 mL/min.

Table 5.5: Particle size distribution statistics for nanoparticles synthesized from droplets with initial volumes of 0.044, 0.25, and 1.13 µL, n = 200.

Vol. (µL)	Mean (nm)	Std. Dev. (nm)	CV
0.044	46	11	0.25
0.25	54	10	0.18
1.13	48	11	0.22

Changing the droplet diameter impacts every aspect of transport phenomena in the interphase droplet reactor. As discussed in Chapter 4, the mass transfer behavior changes as the droplet volume increases. Others have shown that droplet mixing and heat transfer are affected by changing the volume of translating droplets. It is expected that these factors would impact the synthesis of zinc oxide nanoparticles in the droplets. As seen in Table 5.5, the droplet volume of 0.25 µL produced the largest average nanoparticle size, 54 nm. The 0.044 and 1.13 uL droplets produced smaller average particle sizes. Figure 5.16 shows the SEM micrographs of the particles produced for these trials. Interestingly, changing the droplet volume produce a larger change in the mean nanoparticle size than increasing the total system convection did in Section 5.5. This may indicate that there is more than a change in the mass transfer rate affecting the size of the nanoparticles synthesized in the smaller droplet volume.

When the droplet volume was decreased, the surface area to volume ratio of the droplet was increased which would have increased the rate of mass transfer of sodium hydroxide to the droplet phase [175]. Faster mass transfer leads to faster reaction rates, causing faster nucleation and a smaller average particle size [169]. The larger CV for the nanoparticles produced in the 0.044 µL droplets may have been the result of a decrease in internal droplet mixing. A droplet with a radius less than the channel radius tends to have a lesser degree of mixing due to shear on the droplet interface being generated by the flow of the continuous phase, not the thin film near the channel wall [131]. The 0.25 µL droplet volume has a droplet radius approximately equal to the channel radius and is the transition from a droplet shape to a slug shape. This droplet size has also been shown in other interphase droplet reactors to produce a local maximum in the nanoparticle size [82]. Increasing the droplet volume beyond this point tends to decrease the mean nanoparticle size, as is also seen in Table 5.5. The mechanism behind the decreasing nanoparticle size with

increasing droplet volume is not understood yet, however the images in Figure 5.17 of droplets near the reactor's outlet indicate very different behavior occurring as droplet volume increases.

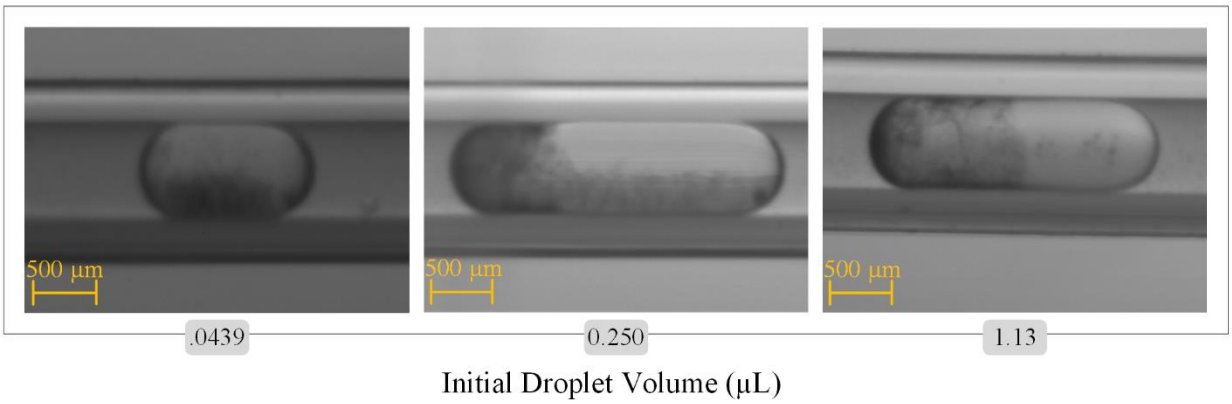

Figure 5.17: Droplets resulting from three different initial droplet volumes near the outlet of a 10-min. residence time reactor. Droplets formed from an initial 0.033 M zinc acetate solution, introduced into a stream of 0.1 M sodium hydroxide in octanol solution, total flow rate = 0.165 mL/min.

Figure 5.17 shows the nanoparticle laden aqueous droplets near the reactor outlet. The images for the droplets with initial volumes of 0.044 and 0.25 µL show larger droplet volumes at the outlet due to droplet merging that occurs through the length of the reactor. Due to the increased spacing between the 1.13 µL droplets, the largest droplet volumes did not experience droplet merging as discussed in Chapter 4. In the 0.044 and 0.25 µL droplets, freely flowing nanoparticle aggregates can be seen in the bottom portion of the droplets. The 1.13 µL droplets, however, produce very minimal amounts of visible nanoparticle aggregates. Under visual inspection, the yield of nanoparticles in the 1.13 µL droplets appears to have been lower than the smaller initial droplet volumes.

When the droplet volume is large enough to produce a slug shape, generally the internal droplet mixing is increased due to the shear produced by the thin film of the continuous phase between the droplet interface and the channel wall [131]. As the slug length increases, however, mixing between the upper and lower halves of the volume can be reduced to a point where only

diffusive mixing occurs [153]. The recirculation becomes localized in the separate halves of the slug. When heat transfer in droplet systems has been investigated, an increase in heat transfer occurs as the droplet shape transitions from spherical to slug [39]. This has been attributed to the increase in internal and external fluid recirculation caused by a slug translating through a channel.

When the mass transfer behavior of larger droplet volumes was investigated in Chapter 4, it was observed that the rate of sodium hydroxide into the droplet increased, but the total time required for the methyl orange indicator color change to occur increased as well. This shows that the 1.13 µL droplet would have required a longer time than the 0.25 µL droplet to fully react the zinc acetate contained in the volume. This behavior, however, would favor slower nucleation which would produce larger particle sizes. It is possible then that the changes in heat transfer and internal droplet convection counteracted the mass transfer behavior of the larger droplet. The decrease in internal convection and mass transfer may lead to production of nanoparticles in localized regions of the droplet. The improved heat transfer may have increased the zinc oxide reaction rate. The behavior of the nanoparticle synthesis in the 1.13 µL droplets is a good demonstration of how much the interphase synthesis of nanoparticles is a balance between momentum, heat, and mass transfer as well as reaction kinetics.

5.7 Effect of Surfactants

Surfactants are a common addition in both droplet based systems and nanoparticle synthesis reactions. In droplet based systems, surfactants are commonly used to prevent droplet coalescence [7]. The presence of surfactants in a nanoparticle synthesis can affect the growth and aggregation of nanoparticles due to the tendency of surfactant molecules to adsorb onto the surface of nanoparticles [138]. In this study, only the effect of sodium dodecyl sulfate (SDS) on the size and morphology of the ZnO nanoparticles was investigated. Sodium dodecyl sulfate is a small

anionic surfactant molecule that has been shown to influence zinc oxide particle growth [130,161]. Due to the polarity of SDS, it will preferentially adsorb onto the polar (0001) plane of zinc oxide, which can lead to anisotropic growth. It has also been proposed that SDS molecules can form as a micelle around zinc oxide nanoparticles, with the hydrophobic tail of the molecule pointing towards the solid zinc oxide [162]. The presence of the micelle inhibits further growth of the nanoparticles. The effect of the addition of 1 mM SDS to the droplet phase on the size of the ZnO nanoparticles was investigated using a zinc acetate concentration of 0.033 M and an inlet sodium hydroxide concentration of 0.1 M. Figure 5.18 shows the nanoparticles produced with no SDS added and the particles produced with 1 mM SDS added to the droplet phase. Higher concentrations of SDS were not used because the surfactant appeared to precipitate at the droplet interface and interfered with the droplets smoothly translating through the reactor. As seen in Table 5.6, the size of the nanoparticles produced with SDS added to the droplets was smaller than the clean trials. The presence of SDS did not produce anisotropic growth, but appeared to inhibit the overall growth of the nanoparticles.

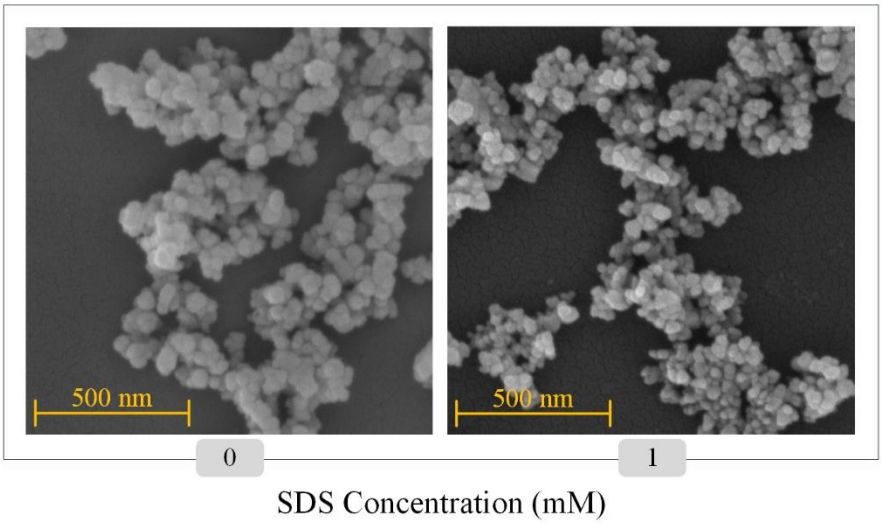

Figure 5.18: SEM micrographs showing the effect of the addition of SDS on particle size. The reaction temperature was 60˚C and the residence time was 10 minutes.

Table 5.6: Particle size distribution statistics for particles synthesized in clean droplets and droplets with 1 mM SDS.

[SDS]	Mean (nm)	Std. Dev. (nm)	CV
1 mM	43	10	0.22
0 mM	54	10	0.17

5.8 Batch Reactor Comparison

The zinc oxide nanoparticles synthesized using the interphase droplet flow reactor were compared with a single-phase batch reactor using a residence time of 10 minutes, sodium hydroxide concentration of 0.1 M, and various zinc acetate concentrations. A comparison of the particle morphology and size distributions is seen in Figures 5.19 and 5.20 and Table 5.7. When compared to the single phase aqueous batch synthesis of zinc oxide nanoparticles, the millifluidic synthesis displays a number of advantages. For the three different zinc acetate concentrations used, Figure 5.19 shows that the flow reactor produced nanoparticles with a more homogenous morphology. The flow reactor produced mostly spherical particles as opposed to the batch reactor which produced a mixture of spherical and plate-like particles, especially at higher zinc acetate concentrations. The flow reactor also produced particles with a narrower particle size distribution compared to the batch reactor as seen in Figure 5.20 and Table 5.7.

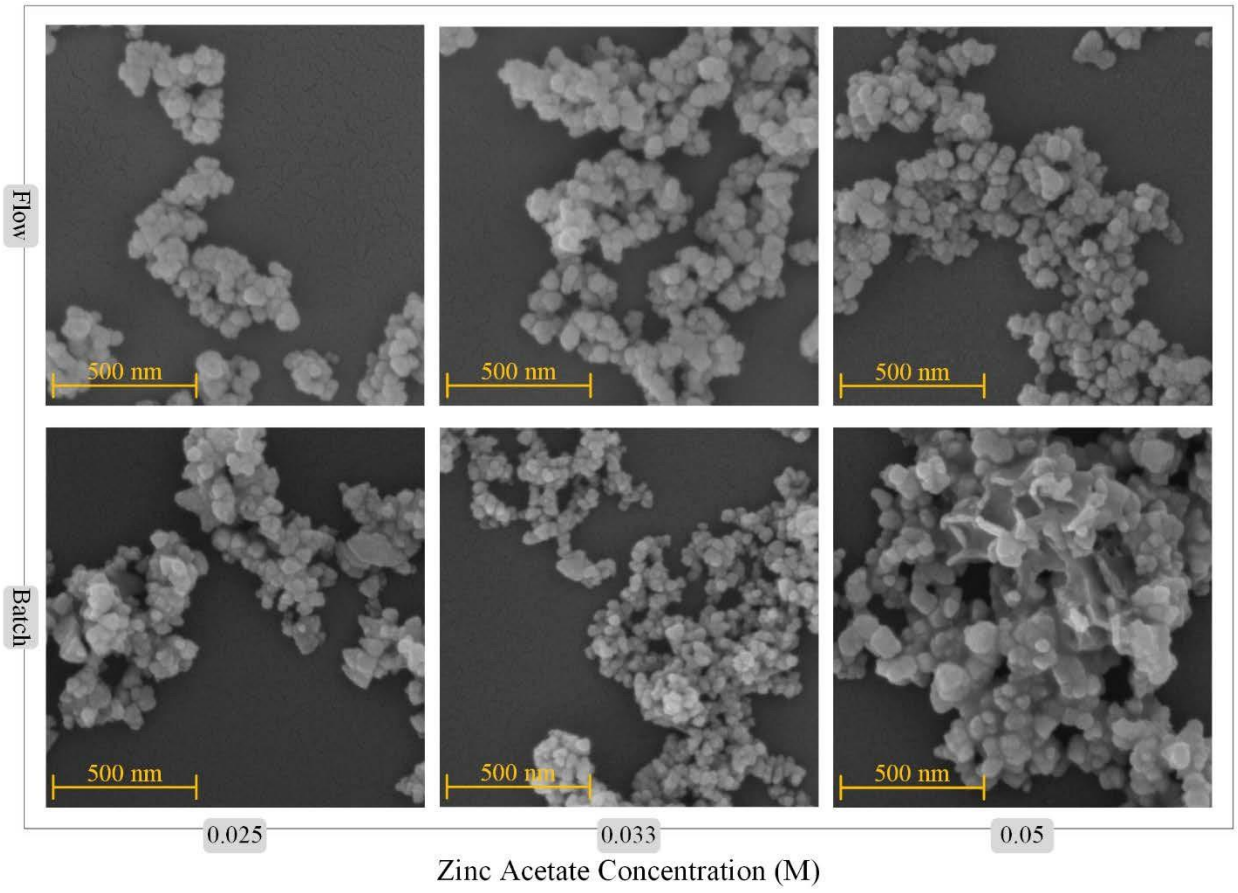

Figure 5.19: SEM micrographs comparing zinc oxide nanoparticles produced from the droplet flow reactor and a batch reactor at various zinc acetate concentrations. The reaction temperature was 60˚C and the sodium hydroxide concentration was 0.1 M.

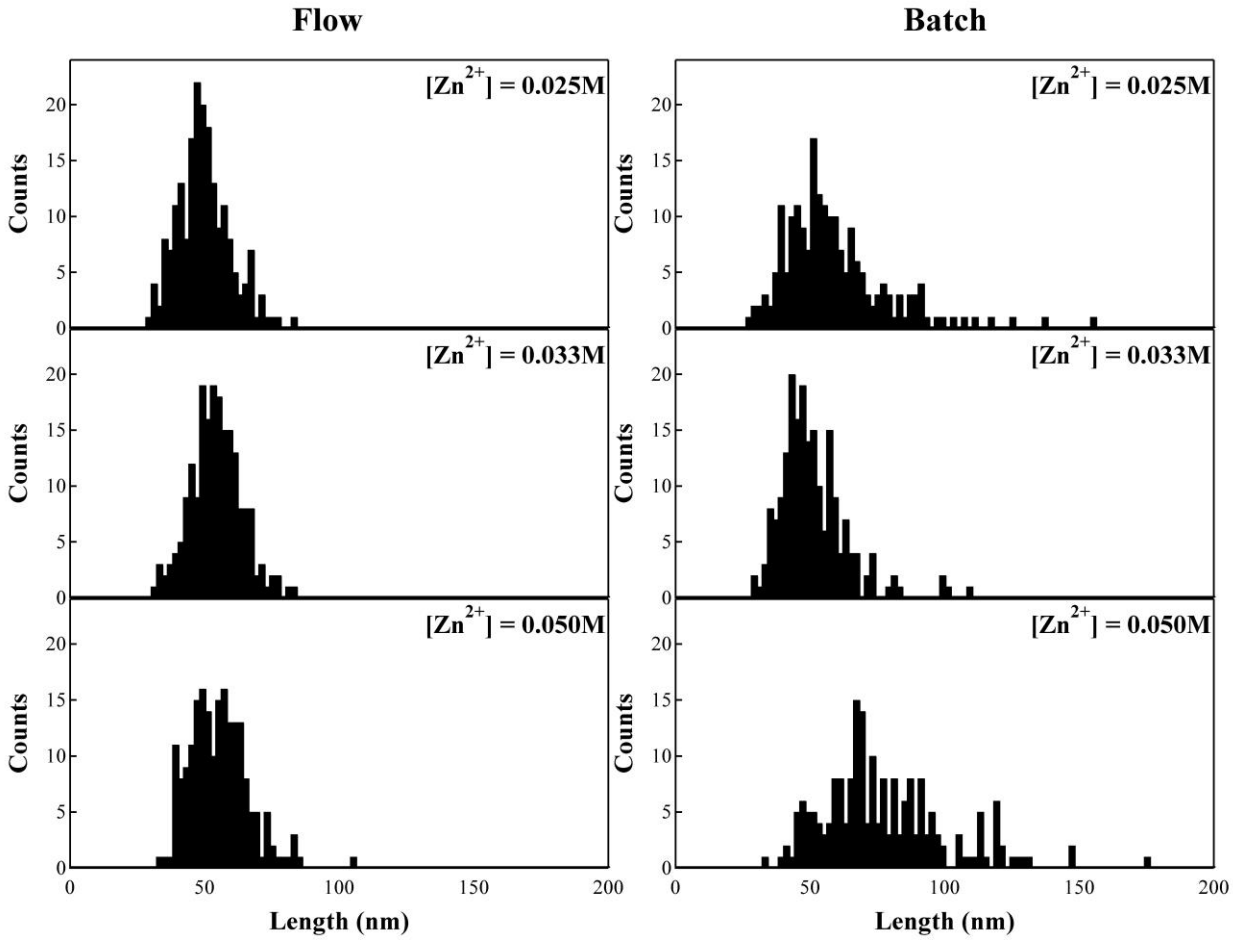

Figure 5.20: Particle size distributions for nanoparticles synthesized in either the batch reactor or the droplet flow reactor using various zinc acetate concentrations. The reaction temperature was 60˚C and the sodium hydroxide concentration was 0.1 M, n = 200.

Table 5.7: Particle size distribution statistics for nanoparticles synthesized in either the batch reactor or the droplet flow reactor using various zinc acetate concentrations. The reaction temperature was 60˚C and the sodium hydroxide concentration was 0.1 M, n = 200.

	Flow			Batch		
$[Zn^{2+}]$ (M)	**Mean (nm)**	**Std. Dev. (nm)**	**CV**	**Mean (nm)**	**Std. Dev. (nm)**	**CV**
0.025	50	10	0.20	59	20	0.33
0.033	54	10	0.18	51	13	0.25
0.050	55	11	0.20	78	25	0.33

The work presented in this chapter has demonstrated the synthesis of zinc oxide nanoparticles in an interphase droplet reactor. The reaction temperatures, reagent concentration, and residence time have been shown to affect particle size and morphology. While the size of the ZnO nanoparticles was also affected by the initial droplet size used in the reactor, the mean size was not as responsive to the total system flow rate. The addition of the surfactant SDS was shown to reduce the mean particle size as compared to a clean system. Finally, the interphase droplet reactor was shown to produce a narrower particle size distribution than a batch reactor and a more homogenous particle morphology.

Chapter 6: Conditions for Mesocrystal Formation

When the right conditions are present during zinc oxide nanoparticle synthesis, the resulting ZnO nanoparticles will aggregate in a highly ordered manner, known as oriented attachment. During oriented attachment, zinc oxide nanoparticles preferentially align along the *c*-axis of the wurtzite crystal structure, minimizing the charges present on the polar (0001) and $(000\bar{1})$ surfaces [93]. To a lesser degree, alignment also occurs along the *a*- and *b*-axis, resulting in complex 3-D mesocrystal structures [144].

In this chapter, the reaction parameters that allow for zinc oxide mesocrystals to form in the interphase droplet reactor are identified. As seen in Figure 6.1, as the sodium hydroxide and zinc acetate concentrations were decreased while keeping the ratio of the concentrations constant, large zinc oxide superstructures were formed. The following sections discuss the effect of: changing reaction temperature, reactant concentrations, droplet volume, residence time, and surfactant concentrations on the morphology of the synthesized nanoparticles. Unless otherwise noted, the reaction parameters used were: zinc acetate concentration, $[Zn^{2+}]$ = 6.3 mM, inlet sodium hydroxide concentration, $[OH^-]$ = 0.025 M, total flow rate, Q = 0.165 mL/min, residence time, τ = 10 min, and temperature, T = 60˚C.

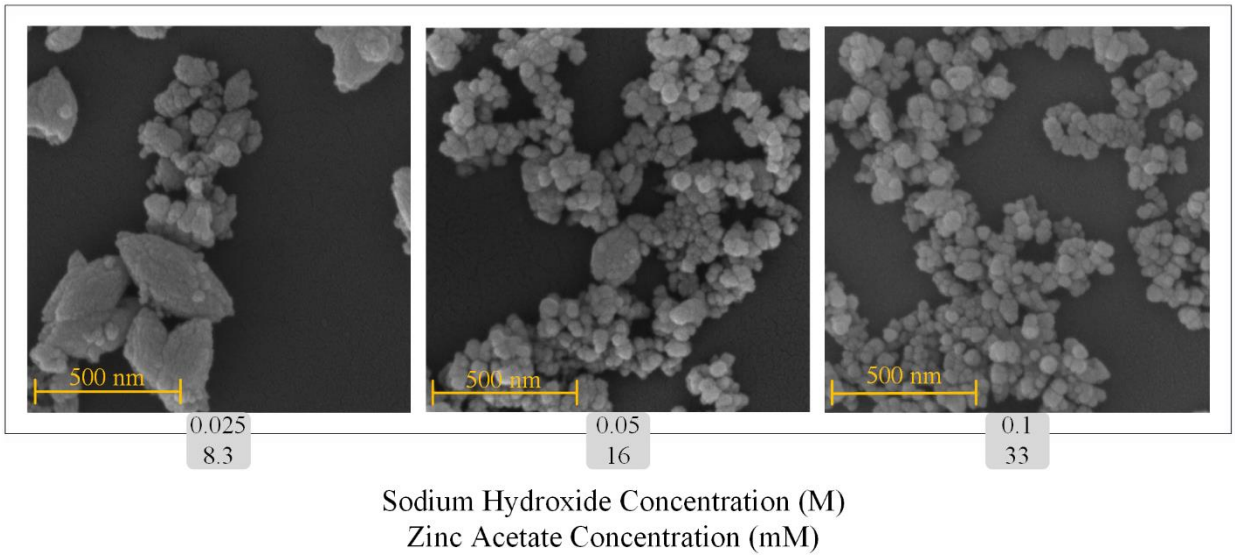

Figure 6.1: SEM micrographs showing the effect of total reagent concentration at a constant ratio between inlet sodium hydroxide and zinc acetate concentrations on mesocrystal formation. Reaction temperature was 60˚C and residence time was 10 min.

6.1 Effect of Zinc Acetate Concentration

When an inlet sodium hydroxide concentration of 0.025 M was used, low initial zinc acetate concentrations yielded well defined ellipsoidal or bi-cone structures. Figure 6.2 shows that zinc acetate concentrations of 6.3 and 8.3 mM were low enough for mesocrystals to form through the oriented attachment process. When the zinc acetate concentration was increased to 12.5 mM, the degree of oriented attachment occurring was reduced. The higher zinc acetate concentration began to interfere with the oriented attachment process, producing the less ordered aggregated structures that were seen along with the ellipsoidal mesocrystals. As the zinc acetate concentration was increased to 16.7 mM, no ellipsoidal mesocrystals developed, only aggregated clusters of particles with a rough spherical morphology were visible. The XRD data shown in Figure 6.3 confirms that all the trials shown in Figure 6.2 produced zinc oxide particles. As the zinc acetate concentration was increased, the concentration of the acetate anion in the droplets was also

increased. Acetate ions in solution have the tendency to coordinate with zinc atoms on the surface of a zinc oxide nanoparticle [100,134]. As the concentration of the acetate complexes on the surface of the zinc oxide nanoparticle increases, so does the stability of a single nanoparticle. Therefore, high concentrations of acetate complexes on the nanoparticle surface can act as a capping layer, inhibiting aggregation [75].

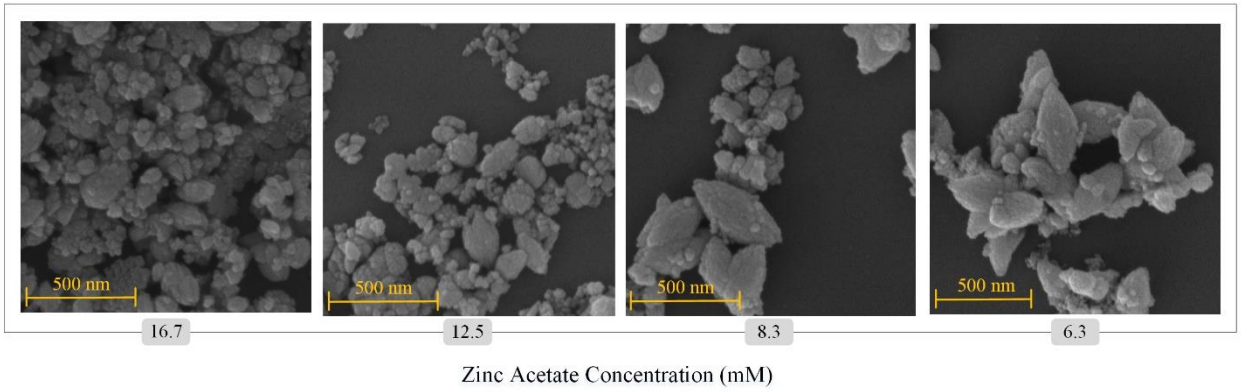

Figure 6.2: SEM micrographs showing the effect of zinc acetate concentration on mesocrystal formation. Inlet sodium hydroxide concentration was 0.025 M, reaction temperature was 60˚C and residence time was 10 min.

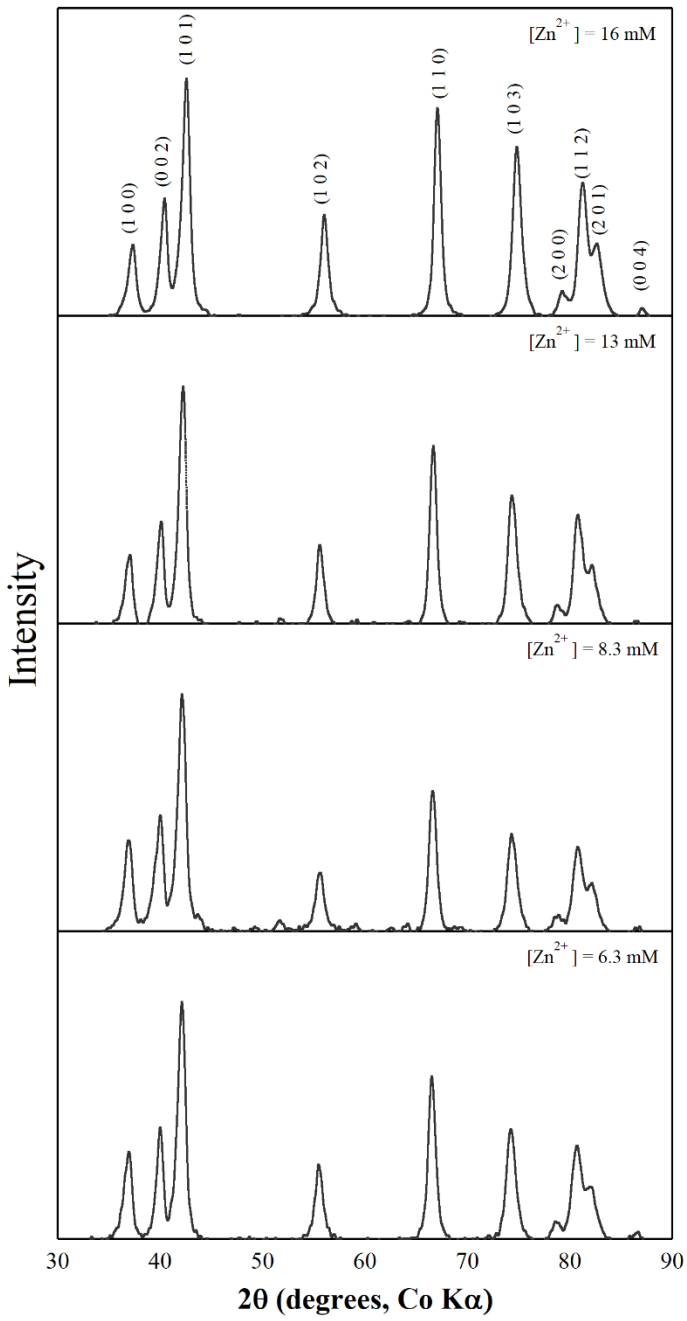

Figure 6.3: XRD data for zinc oxide particles synthesized using an inlet sodium hydroxide concentration of 0.025 M.

6.2 Effect of Sodium Hydroxide Concentration

The hydroxide ions play many roles during zinc oxide synthesis. Most importantly, it hydrolyzes the zinc ion to form zinc oxide. For the formation of zinc oxide to proceed, a stoichiometric excess of hydroxide ions is used to drive the reaction towards the formation of zinc oxide instead of forming zinc hydroxide species. Hydroxide ions can also adsorb onto the polar faces of zinc oxide nanocrystals, behaving as capping agents [177]. Also, if an excess of hydroxide ions increases the pH of the solution too high, zinc oxide begins to dissolve [98]. For the formation of zinc oxide mesocrystals in an interfacial droplet reactor, increasing the initial sodium hydroxide concentration is detrimental to the formation of well-defined ellipsoidal structures.

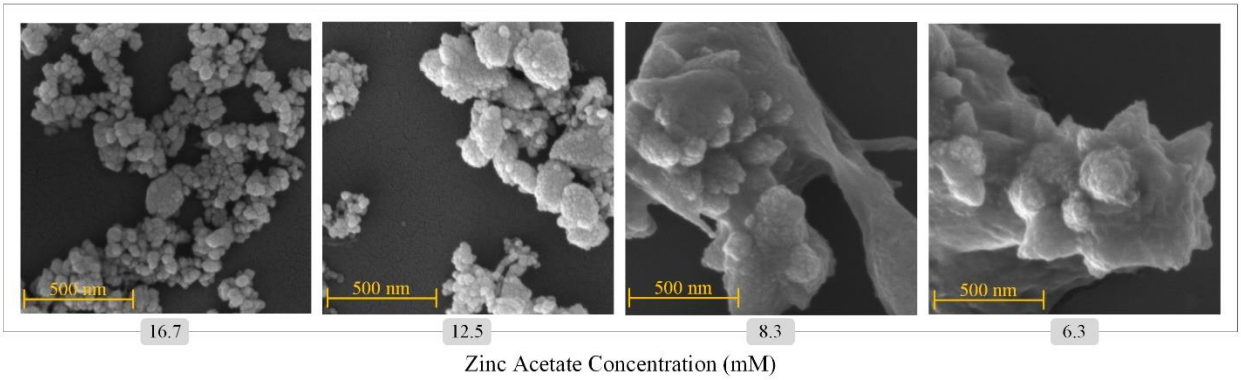

Figure 6.4: SEM micrographs showing the effect of zinc acetate concentration on mesocrystal formation. Inlet sodium hydroxide concentration was 0.05 M, reaction temperature was 60˚C and residence time was 10 min.

Figure 6.4 shows the particles formed when an initial sodium hydroxide concentration of 0.05 M was used. For the trial where a zinc acetate concentration of 16.7 mM was used, very few aggregated structures appeared, the primary product was small spherical nanoparticles. This is similar to the result seen in Figure 6.2 when a sodium hydroxide concentration of 0.025 M was used. When the zinc acetate concentration was decreased to 12.5 mM, ellipsoidal structures with

rough surfaces were produced. When the zinc acetate concentration was decreased even further to 8.3 and 6.3 mM, highly agglomerated clusters of ellipsoidal structures were formed. In Figure 6.2, these two zinc acetate concentrations produced well defined ellipsoidal morphologies when a sodium hydroxide concentration of 0.025 M was used. The morphology seen in these two trials suggests that ellipsoids were initially produced in the droplets. As the droplets translated through the reactor, mass transfer continued to increase the hydroxide ion concentration in the droplets. Due to the higher initial sodium hydroxide concentration in the continuous 1-octanol stream, a higher final pH was produced in the droplet. The higher pH in the droplet appears to have driven the agglomeration and partial dissolution of the ellipsoids [120]. The formation of the agglomerated structures in Figure 6.4 first occurred when a zinc acetate concentration of 8.3 mM was used, a ratio of $[Zn^{2+}]$: $[OH^-]$ = 1:6. This is consistent with agglomeration seen in Chapter 5 that occurred when the same concentration ratio of 1:6 was used.

6.3 Effect of Droplet Volume

For most of the work presented here, spherical droplets with an average initial volume 0.21 µL were used in the interphase droplet reactor. The droplet volume of 0.21 µL corresponds to a droplet diameter approximately the same as the reactor tubing, allowing mass transfer to occur through all of the droplet's interfacial area. As Figure 6.5 shows, when the droplet volume is increased while maintaining the same tubing diameter the spherical droplet shape transitions to a cylindrical slug shape. Due to the confinement of the walls of the tubing, the spherical caps are the only portion of the slug exposed to the continuous phase flow. While a thin film of the continuous phase does exist between the slug and the tube wall, at low fluid velocities the film becomes depleted and does not significantly contribute to the mass transfer from the continuous phase to the droplet phase [43,76]. Overall, the larger slug has a smaller active interfacial area to volume

ratio than the spherical droplet. The slug, though, has a greater contact area with the tube wall which produces shear on the slug interface. The increase in shear on the slug relative to the droplet increases the internal convection in the slug which can produce a higher rate of mass transfer compared to a spherical droplet [29].

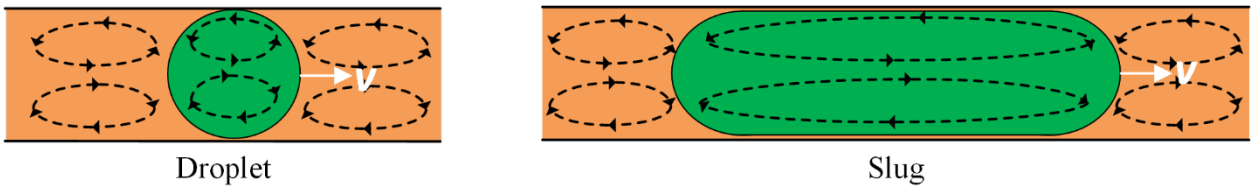

Figure 6.5: Schematic of the shape of droplet versus the shape of slug translating through tubing with a velocity, *v*, along with approximations of fluid flow patterns.

Figure 6.6 shows the morphology of the mesocrystals produced from three different initial droplet volumes, 0.21, 0.98, and 1.7 µL. As mentioned, a volume of 0.21 µL corresponded with a spherical droplet shape while volumes of 0.98 and 1.7 µL were slugs. A 21-guage needle, instead of a 27-guage, was used to produce the larger volumes, which allowed all three trials to be conducted at the same flow rates. As the initial volume was increased from 0.21 to 0.98 µL, there was no clear effect on the morphology of the mesocrystals. When the initial volume was increased further to 1.7 µL, smaller more spherical mesocrystals were produced and the ellipsoidal particles that were formed were more rounded. While oriented attachment is still possible in the 1.7 µL droplets, there is a change in mesocrystals morphology as droplet volume is increased. As discussed in Chapter 4, an increase in droplet volume increased the mass transfer rate of sodium hydroxide into the droplet. The larger droplet volumes, however, required a longer time than the smaller spherical droplets to reach the same conversion values. The results shown in Chapter 4

indicate that when the volume was increased, a longer time was required to fully react all the zinc acetate in the slug volume as compared to the smaller 0.21 µL droplet. The presence of unreacted zinc acetate for a longer time in the slug volume may interfere with the oriented attachment of zinc oxide nanoparticles that had already formed in the slug.

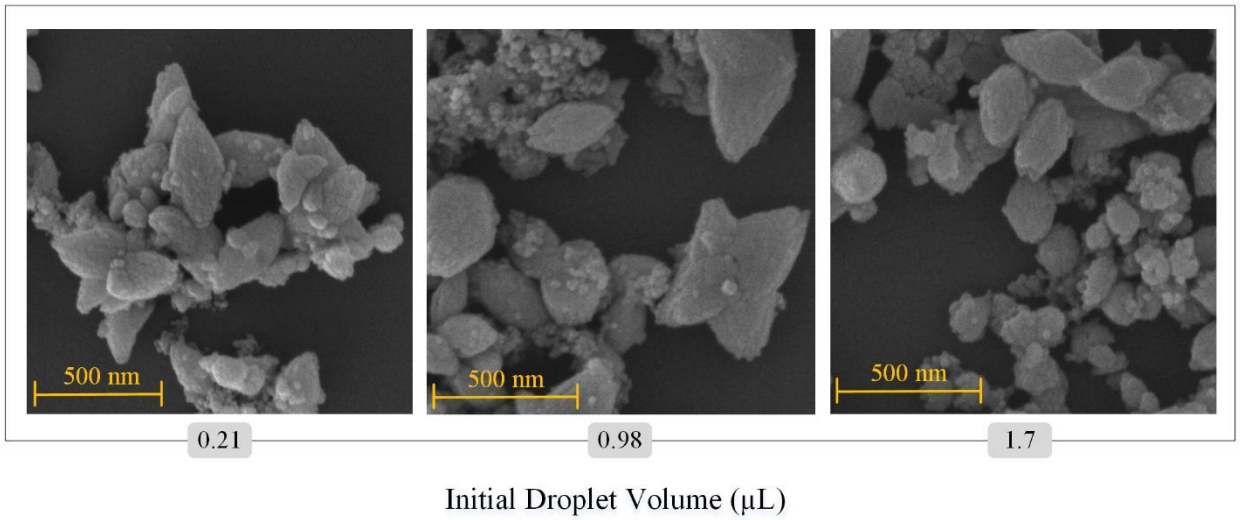

Figure 6.6: SEM micrographs showing the initial droplet volume on mesocrystal formation. Inlet sodium hydroxide concentration was 0.025 M, zinc acetate concentration was 6.3 mM, reaction temperature was 60˚C and residence time was 10 min.

6.4 Effect of Reaction Temperature

Reaction temperature is a key parameter for any reacting system and the ability to produce desired products at lower temperatures is beneficial from both an energy and safety perspective. Operating the interfacial droplet reactor at a temperature of 25˚C produced an amorphous product. The XRD spectrum from this trial, shown in Figure 6.8, shows no strong diffraction peaks. Figure 6.7 shows that the morphology of the solids produced at this temperature were agglomerated particles and sheets. When the reaction temperature was increased to 40˚C, well defined ellipsoidal mesocrystals were produced. The morphology of the mesocrystals produced from operating the

reactor at 60˚C did not have significant differences from the products of a 40˚C reaction temperature. The products of the 40˚C trial, however, show more branching at the midsection of the ellipsoids than the products of the 60˚C trial. These reaction temperatures can produce the stable primary nanoparticles that are the building blocks of the larger, ordered mesocrystals [105]. A reaction temperature of 25˚C does not produce the stable, individual, primary nanoparticles that can assemble through oriented attachment into a larger mesocrystal structure.

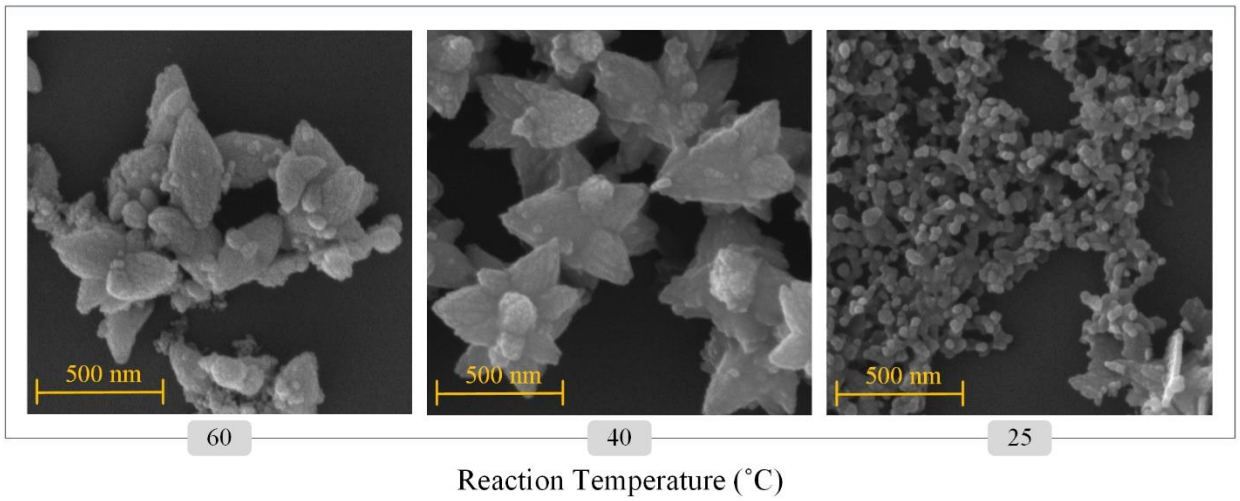

Figure 6.7: SEM micrographs showing the effect of reaction temperature on mesocrystal formation. The zinc acetate concentration was 6.3 mM, inlet sodium hydroxide concentration was 0.025 M, reaction temperature was 60˚C and residence time was 10 min.

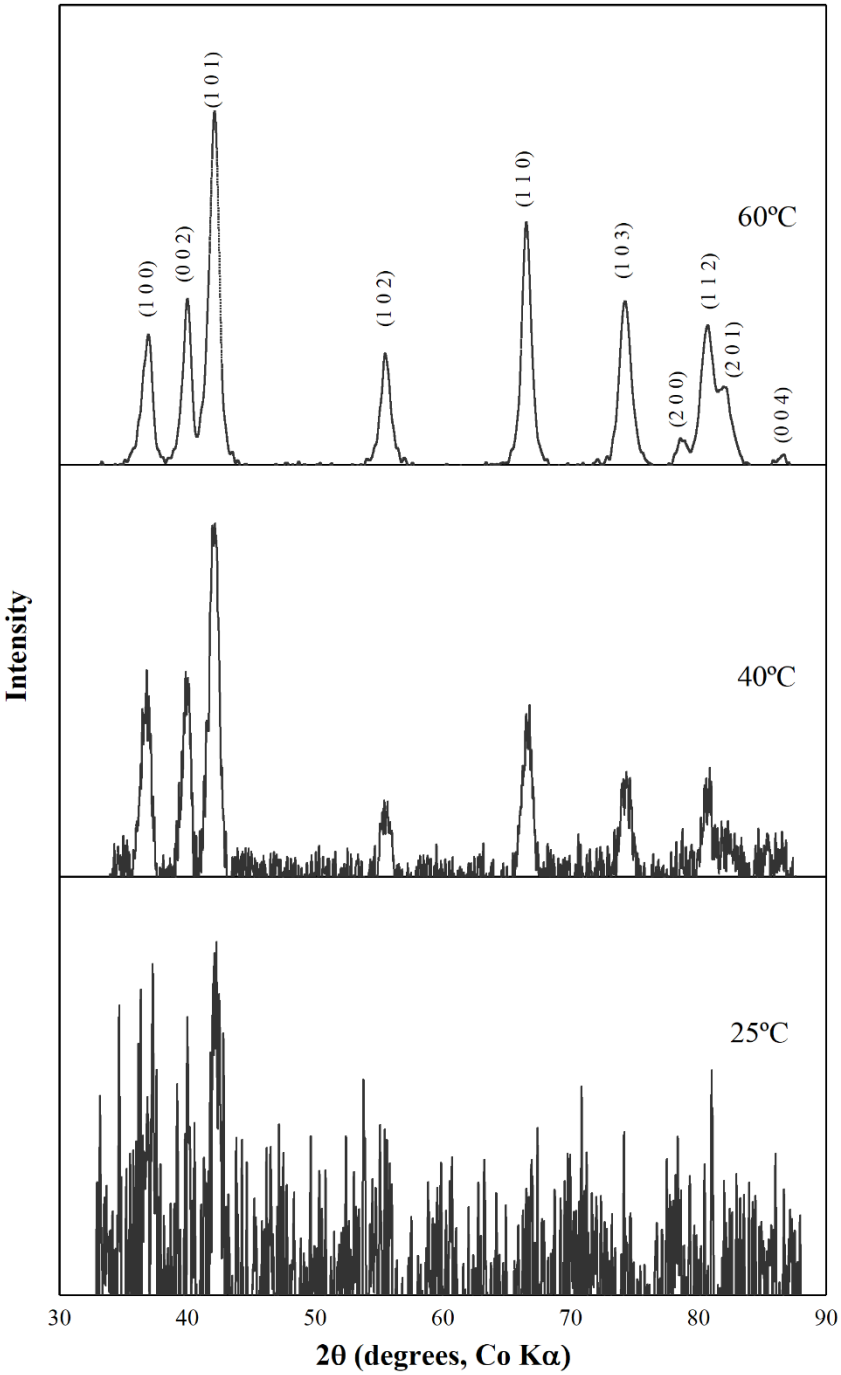

Figure 6.8: XRD data for samples produced at reaction temperatures of 25, 40, and 60˚C.

6.5 Effect of Residence Time

The oriented attachment process that produces zinc oxide mesocrystals can occur rapidly once nanoparticle synthesis is initiated. The foundations of larger zinc oxide mesocrystals have been isolated from a batch reactor within 10 s of the reaction starting [120]. Ellipsoidal ZnO mesocrystals have also been formed in under 1 minute by using the electrochemical dissolution of zinc plates in water [83]. The effect of residence time on the formation of zinc oxide mesocrystals in the interphase droplet reactor was investigated by using three different lengths of tubing to control the residence time. This allowed for the flow rates to be held constant for all three trials, maintaining similar fluid dynamics for each trial. As seen in Figure 6.9, with a 2-minute residence time, zinc oxide mesocrystals had already formed in the droplets. There are both mesocrystals with an essentially fully formed ellipsoidal morphology and smaller structures with only a rough ellipsoidal shape. The mesocrystals formed from a 10-minute residence time have a more tapered morphology, but the ellipsoidal shape persists. The oriented attachment process that produces the ellipsoidal mesocrystal structure is rapid and demonstrates the high rate of heat transfer and mass transfer that occurs within the interphase droplet reactor. The XRD data in Figure 6.10, shows that a 2-minute residence time was enough to produce almost entirely zinc oxide.

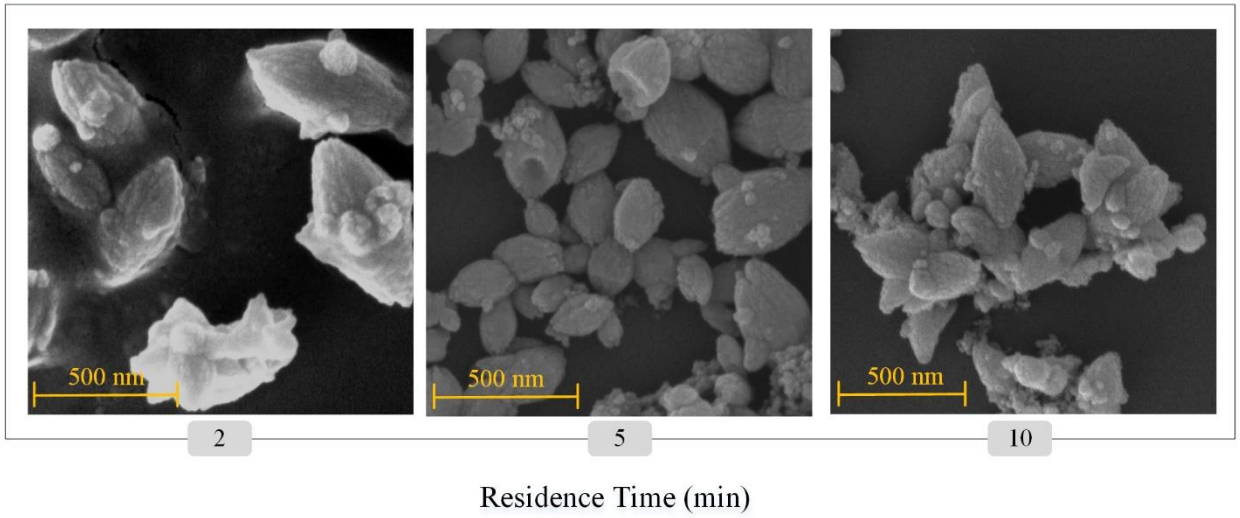

Figure 6.9: SEM micrographs showing the effect of residence time on mesocrystal formation. Inlet sodium hydroxide concentration was 0.025 M, zinc acetate concentration was 6.3 mM, and reaction temperature was 60˚C.

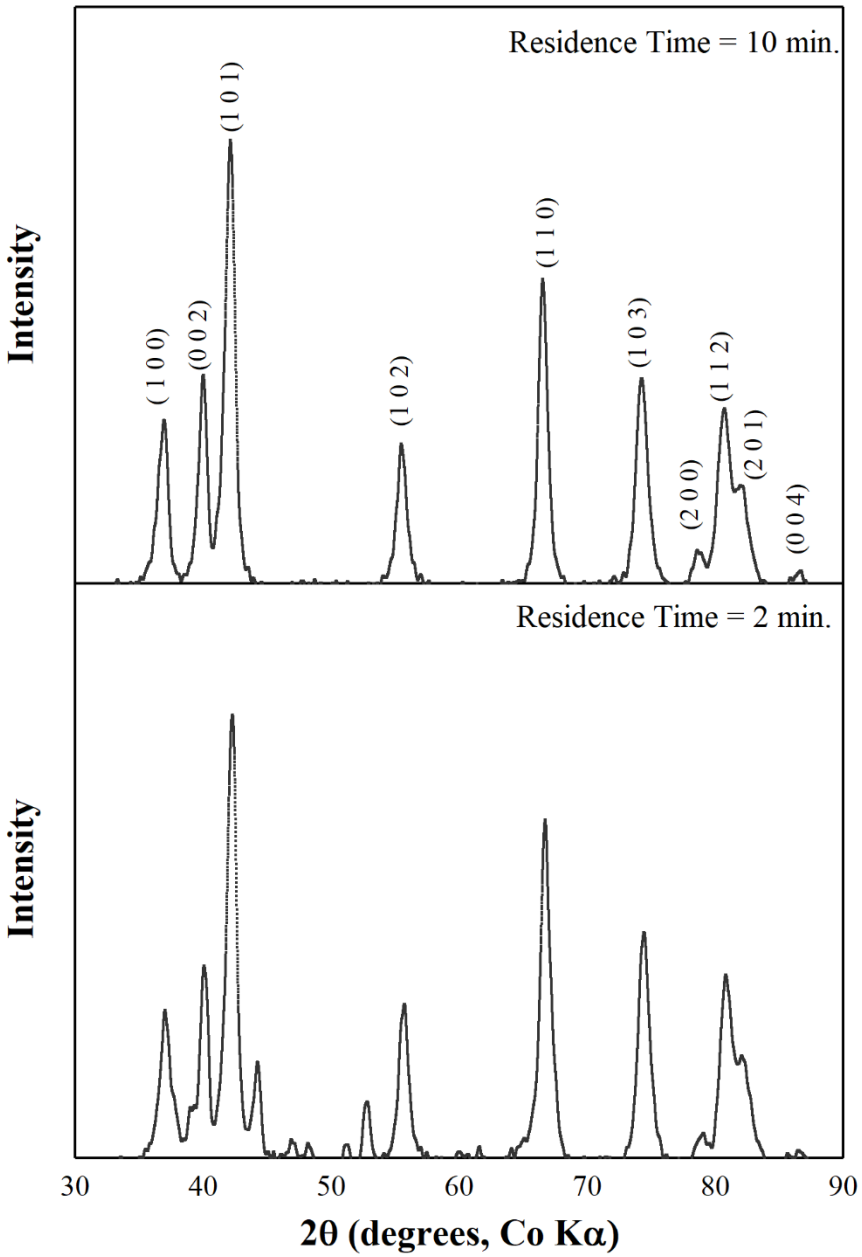

Figure 6.10: XRD data for the 2-minutes and 10-minutes residence time trials.

6.6 Mesocrystal Formation Mechanism

As mentioned previously, zinc oxide mesocrystals arise from the ordered arrangement of primary zinc oxide nanoparticles. The arrangement of ZnO nanoparticles into a larger superstructure is driven by the polarity of zinc oxide's wurtzite crystal structure, the (0001) plane

is zinc terminated and the $(000\bar{1})$ is oxygen terminated [93]. Alignment of the primary ZnO nanoparticles occurs preferentially along the *c*-axis in order to minimize the surface charge of the two polar planes. To a lesser extent, alignment also occurs along the *a*- and *b*-axis [144] which creates the large ellipsoidal mesocrystals seen in this work. While the overall description of the oriented attachment process for zinc oxide mesocrystals formation is widely used, the specific order of the attachment varies in many published experiments.

In one proposed mechanism, the ellipsoidal structure is the starting morphology and growth of the ellipsoid continues outward based on the alignment rates for the *a*-, *b*- and *c*- axes [144]. In a similar mechanism, both spherical particles and rods are initially formed and aggregate into a rough ellipsoidal morphology. The nanoparticles then fill in the gaps between oriented rods and the surface is closed by Ostwald ripening [88,120]. Another mechanism proposes that the first structure to form through oriented attachment of primary nanoparticles is cone shaped and then two cones attach at their bases to form an ellipsoidal structure [69,83]. The growth of secondary cones then tends to occur at the junction of the two bases due to the presence of higher surface energy at that location. One other growth mechanism states a single cone is the first structure to form and then from the base of that cone, another cone begins to grow in the opposite direction [120,189].

Without the ability to extract products from the droplets just as the reaction is initiating in the interphase droplet reactor, it is difficult to definitively identify which formation mechanism is occurring for the results presented here. Based on the SEM micrographs for the trials previously discussed, a likely candidate mechanism can be proposed. Figure 6.2 showed how increasing the zinc acetate concentration begins to interrupt the ability to form mesocrystals. While a zinc acetate concentration of 12.5 mM began to interrupt the ability for the nanoparticles to aggregate,

ellipsoidal structures are still visible. Decreasing the zinc acetate concentration to 8.3 mM allowed ellipsoidal mesocrystals to develop. Alongside the large ellipsoids in the micrograph for the 8.3 mM zinc acetate trials are smaller ellipsoids. This suggests that the structure formed at the beginning of the oriented attachment process is ellipsoidal, as described by Sun et al. [144].

6.7 Effect of Surfactants

Surfactants are a common addition in both droplet based systems and nanoparticle synthesis reactions. In droplet based systems, surfactants are commonly used to prevent droplet coalescence [7]. The presence of surfactants during nanoparticle synthesis can affect the growth and aggregation of nanoparticles due to the tendency of surfactant molecules to adsorb onto the surface of nanoparticles [138]. In order to determine how surfactants affect zinc oxide nanoparticle synthesis and the oriented attachment process in an interphase droplet reactor, two common surfactants were used: Triton X-100 and sodium dodecyl sulfate (SDS). Triton X-100 is a large, non-polar surfactant molecule while SDS is a smaller anionic surfactant.

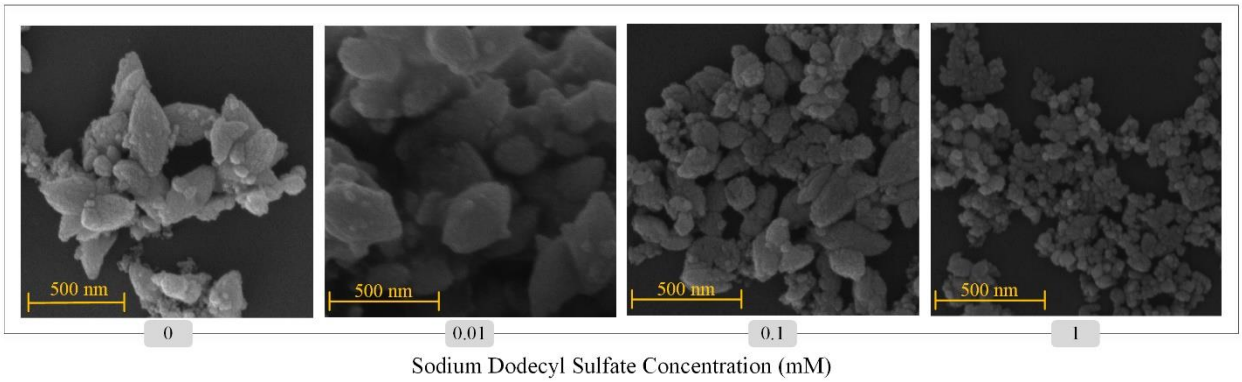

Figure 6.11: SEM micrographs showing the effect of sodium dodecyl sulfate concentration on mesocrystal formation. The zinc acetate concentration was 6.3 mM, inlet sodium hydroxide concentration was 0.025 M, reaction temperature was 60˚C and residence time was 10 min.

When a concentration of 0.01 mM SDS was added to the droplet solution, as seen in Figure 6.11, little impact on the morphology of the mesocrystals was observed. As the concentration was

increased to 0.1 mM, the structure of the mesocrystals became less defined. The zinc oxide nanoparticles displayed a more limited oriented attachment into larger structures, the structures visible lack the clear ellipsoidal morphology of the trial synthesized with 0.01 mM SDS or in the clean results discussed earlier. When the concentration of SDS was increased to 1 mM, the oriented attachment process was interrupted, only small individual zinc oxide nanoparticles were produced. SDS is a negatively charged surfactant molecule and will preferentially adsorb onto the polar (0001) plane of zinc oxide nanoparticles [138]. The polar nature of the (0001) is also the driving force behind the oriented attachment process for zinc oxide [105]. The charge of this plane is minimized by aggregating the particles into larger order structures. The presence of higher concentrations of SDS on the surface of the zinc oxide particles interrupts the formation of mesocrystals through the oriented attachment process.

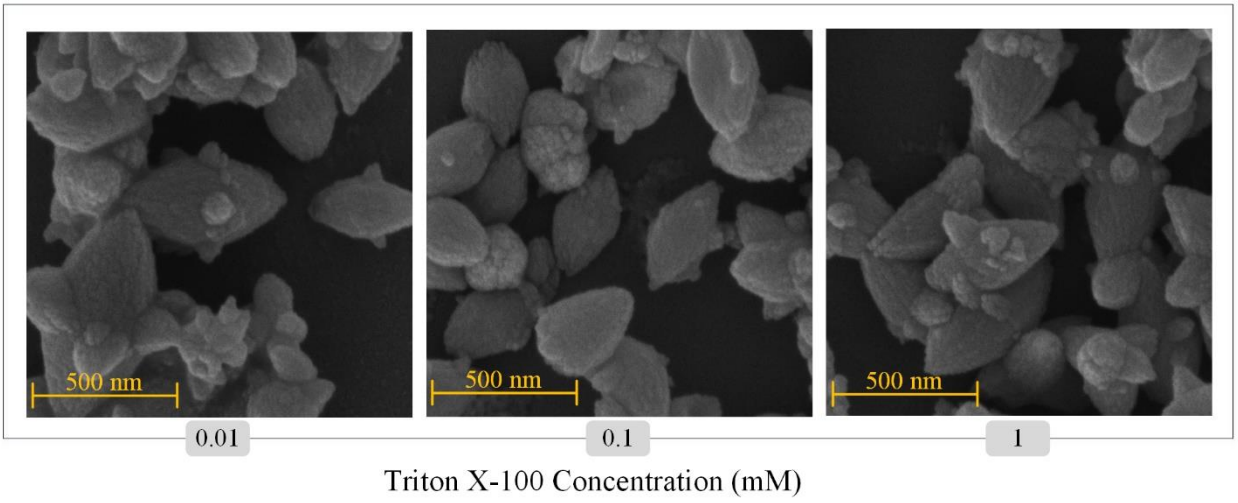

Figure 6.12: SEM micrographs showing the effect of Triton X-100 concentration on mesocrystal formation. The zinc acetate concentration was 6.3 mM, inlet sodium hydroxide concentration was 0.025 M, reaction temperature was 60˚C and residence time was 10 min.

In contrast to the addition of SDS, the addition of TX-100 does not interrupt the oriented attachment process. Across the three TX-100 concentrations used in Figure 6.12, zinc oxide particles still formed ellipsoidal mesocrystals. TX-100 is a non-polar surfactant molecule which

will adsorb onto zinc oxide, but it will not display any specific plane preference. The presence of TX-100 in the droplet phase was also shown in Chapter 4 to affect the rate of mass transfer. Triton X-100 concentrations of 0.1 mM and 1 mM increased the rate of mass transfer when compared to a clean system. The formation of the ellipsoidal mesocrystals does not appear to be sensitive to the increase in mass transfer caused by the presence of Triton X-100. A few explanations are possible as to why TX-100 does not interrupt the oriented attachment process. In the concentration range investigated, the non-preferential adsorption of TX-100 is not enough to interfere with the oriented attachment process. Organic molecules have been shown to aid in the formation of mesocrystals [105]. It may be possible that concentrations used in Figure 6.12 are too low to produce TX-100 surface coverages that would prevent oriented attachment. Unfortunately, increasing the TX-100 concentration much further past 1 mM caused precipitation to occur at the droplet interface and interfered with the droplets ability to smoothly translate through the reactor.

6.8 Controlling Particle Morphology in the Interphase Droplet Reactor

As shown in the work presented in this chapter, low zinc acetate and low sodium hydroxide concentrations favor the oriented attachment of ZnO particles in the interphase droplet reactor. Increasing the concentration of either reagent favors the formation of spherical nanoparticles due to the inhibition of oriented attachment between zinc oxide nanoparticles. Figure 6.13 shows a phase diagram with the concentration dependent morphology trends seen in the interphase droplet reactor, presented in the previous chapter and in this chapter. As discussed earlier, zinc oxide mesocrystals formed when low zinc acetate concentrations were used because the acetate ion concentration was too low to inhibit oriented attachment. A lower acetate ion concentration in the droplet solution provides fewer acetate ions to adsorb onto the zinc oxide surface, stabilizing the nanoparticles.

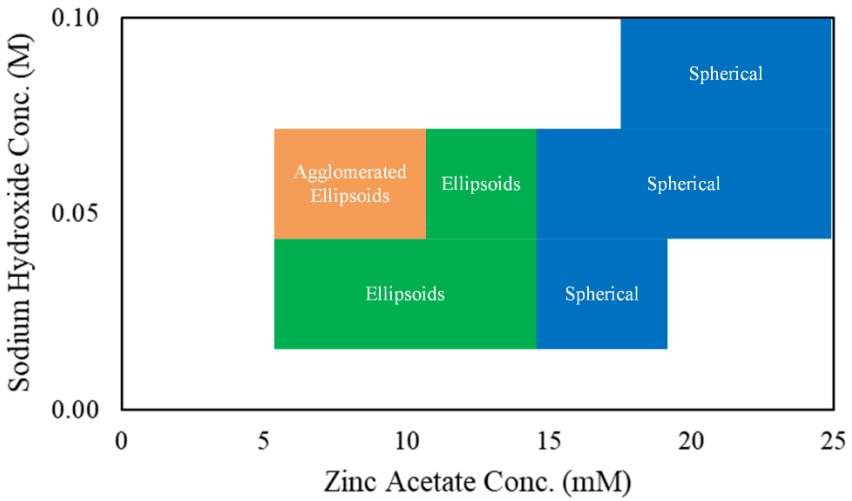

Figure 6.13: Phase diagram identifying the particle morphologies produced with different sodium hydroxide and zinc acetate concentrations in the interphase droplet reactor.

The low concentration range where zinc oxide mesocrystals can form in the interphase droplet appears to contrast with published reports on zinc oxide mesocrystal formation in other reactor systems. Table 6.1 shows a survey of published works that used aqueous zinc acetate to form ordered nanostructures that appeared to arise through the oriented attachment process. Oriented attachment has been observed in systems using zinc acetate concentrations as high as 0.22 M in a hydrothermal reactor [185]. Hydrothermal systems are pressurized reactors allowing them to operate at or above the boiling point of water, as seen by the reaction temperatures reported in Table 6.1. High reaction temperatures can reduce the energy barrier for oriented attachment, however this trend is stronger for high aspect ratio particles [53]. There is, also, more thermal energy present which would promote particle-particle interactions. Carboxylic acid ligands have, however, been shown to have very stable bonds to nanoparticle surfaces at elevated temperatures [25]. The specific behavior of acetate ions on zinc oxide surfaces at elevated temperatures does

not appear to be fully understood. Their behavior at the high temperatures present in hydrothermal reactors may explain the ability of oriented attachment to occur.

Table 6.1: Survey of aqueous based zinc oxide nanoparticle synthesis methods using zinc acetate as the reaction's zinc source.

Solvent	**Temp (˚C)**	**Reactor Type**	**[Zn^{2+}]**	**Base**	**Morphology**	**Ref.**
Water	120	Hydrothermal	0.22 M	2.2 M NaOH	Flower	[185]
Water	120	Hydrothermal	0.063 M	0.4 M	Spherical sheets	[179]
Water	95	Hydrothermal on a silicon wafer	0.17 M	pH 9, NH_4OH	Branched Ellipsoid	[58]
Water	180	Hydrothermal	0.02 M	0.04 M KOH	Initially twin cones	[36]
Water	80	Sonicator	0.05 M	0.05 M TEA	Ellipsoid	[173]
Water	RT	Sonicator	0.01 M	pH 8	Flower	[75]
Water	RT	Sonicator	0.068 M	pH 12 NH_4OH	Branched Ellipsoidal	[89]
Water	60	Batch	0.01 M	350 µL NH_3	Star	[159]
Water	85	Batch	0.2 M	1.2 M, NaOH	Star	[79]
Water	90	Batch	0.02 M	0.03 M Na_2O_2	Star	[18]
Water	90-150	Millifluidic Slug Reactor	0.05 M	0.5 M NaOH	Star	[80]

Mesocrystal formation has been achieved in sonicator based reactors, where mixing is conducted by an ultrasonic transducer. It has been proposed that the cavitation induced during sonication promotes the adsorption of hydroxide ions over acetate ions, allowing oriented attachment to occur [75]. Whether or not this mechanism is accurate, the authors did show that regular stirring resulted in only small spherical particles being produced. Non-hydrothermal aqueous batch reactor synthesis has also been used to synthesize zinc oxide mesocrystals. Synthesis of zinc oxide nanostructures through oriented attachment has been achieved using zinc acetate concentrations as high as 0.2 M [79]. Interestingly, when zinc acetate concentrations of 0.05 M or 0.01 M were used in other aqueous batch reactor systems, only spherical particles were formed [75,118].

Formation of zinc oxide mesocrystals in continuous droplet reactors using zinc acetate has also been reported [80]. A premixed stream of aqueous zinc acetate and sodium hydroxide were used to form droplets in an inert continuous phase. Flower shaped structures were formed using zinc acetate concentrations as high 0.075 M at a reaction temperature of 90˚C. The high temperature dependent behavior may be at work in the droplet reactor as in the hydrothermal systems, allowing the star structures to form. In the droplet reactor, the aqueous streams of zinc acetate and sodium hydroxide are mixed at room temperature prior to droplet formation. This brief room temperature mixing may form sheet structures that could be acting as templates [166] for the formation of the star structures as the droplets are heated downstream in the reactor tubing.

As can be seen in the numerous published reports on zinc oxide nanoparticle synthesis, the pathways towards the formation of complex structures can be complex and the exact details remain to be fully understood. The presence of the acetate ion clearly impacts nanoparticle growth and aggregation, seen when different zinc salts are used under the exact same reaction conditions [75,118]. There appears to be much left to understand about the exact interactions between the acetate ion and the zinc oxide surface at different reaction conditions. The formation of zinc oxide mesocrystals in the interphase droplet reactor, discussed in this chapter, showed a higher sensitivity to zinc acetate concentration than published aqueous synthesis methods using zinc acetate. Further investigation is needed to determine the mechanism behind the inability to form mesocrystals at higher reagent concentrations in the interphase droplet reactor.

Chapter 7: Reactor Scale Down

One of the key arguments for conducting nanoparticle synthesis in droplet reactors is the small droplet volume creates a more homogeneous reaction environment than a batch reactor can. Due to the smaller length scales and recirculating flow patterns in a droplet reactor, mixing and mass and heat transfer in the droplet are more rapid. These processes can also be increased by decreasing the droplet volume. Both heat and mass transfer coefficients have been shown to increase with decreasing channel size [39,156]. Due to the sensitivity of nanoparticle synthesis to parameters such as reaction rate and the rate of reagent addition [75,101,154], the effect of changing the interphase droplet reactor diameter was investigated. The tubing diameter was decreased from 800 μm to 400 μm, while holding the Reynolds number constant. A residence time of 10 minutes and a reaction temperature of 60˚C were used. In an attempt to decrease the droplet volume further, microfluidic reactors with channel widths of 300 μm and heights of approximately 60 μm were constructed. These channels, however, were found to not be suitable for nanoparticle synthesis. The issues encountered during the construction and use of the microfluidic reactors are also presented here.

7.1 Effect of Reactor Scale Down on Mesocrystal Formation

For the trials presented in this chapter, the inlet droplet volume was decreased along with the reactor tubing diameter to maintain the spherical droplet shape, $\kappa \sim 1$. The production of smaller droplet volumes was accomplished by using T-junction to form droplets into a 400 μm channel, as seen in Figure 7.1(b). The larger droplets in Figure 7.1(a) are typical of the droplets used for the trials conducted in the 800 μm diameter tubing. The droplets in Figure 7.1(a) had a volume of 0.21

µL while the droplets in Figure 7.1(b) had a volume of 0.016 µL. To maintain similar fluid dynamics between the trials conducted in the 800 µm tubing and the trials conducted in the 400 µm tubing, the Reynolds number was held constant at 0.49 for both reactor diameters. This required decreasing the total flow rate from 0.165 mL/min to 0.077 mL/min.

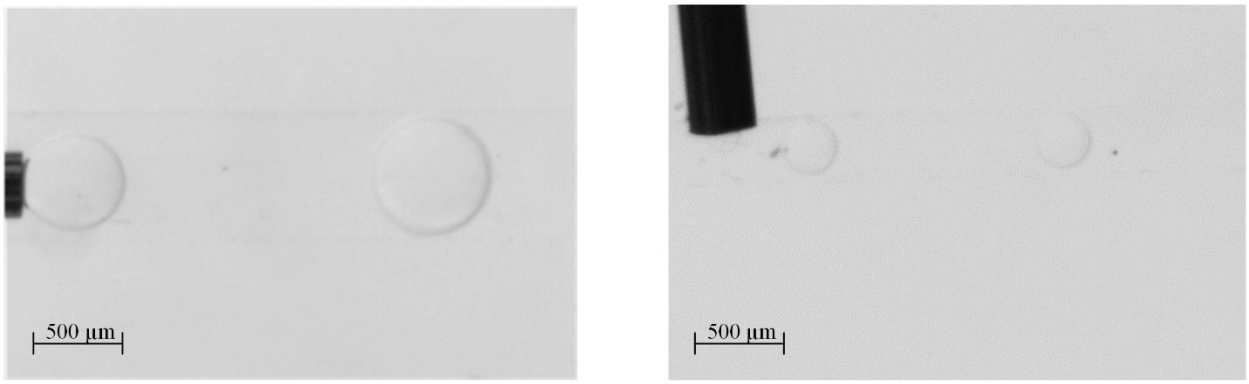

Figure 7.1: (a) Aqueous droplets forming in a continuous flow of 1-octanol in an 800 µm diameter PDMS channel. (b) Aqueous droplets forming in a continuous flow of 1-octanol in a 400 µm diameter PDMS channel.

As previously discussed, low inlet sodium hydroxide and zinc acetate concentrations are necessary for the formation of zinc oxide mesocrystals. Figure 7.2 shows the effect of decreasing the reactor diameter on the formation of ordered zinc oxide structures when an inlet sodium hydroxide concentration of 0.025 M was used. A zinc acetate concentration of 6.3 mM produced similar ellipsoidal structures when either reactor diameter was used. The formation of zinc oxide mesocrystals in the 400 µm diameter reactor was more sensitive to higher zinc acetate concentrations than when the reaction was conducted in the 800 µm diameter reactor. While a zinc acetate concentration of 8.3 mM in the 400 µm diameter reactor was able to produce ellipsoidal structures, the primary morphology visible in the SEM micrographs for that trial was smaller spherical aggregates. A zinc acetate concentration of 8.3 mM in the 800 µm diameter reactor still

primarily produced ellipsoidal mesocrystals. When the zinc acetate concentration was increased to 12.5 mM in the 400 µm diameter reactor, only smaller spherical aggregates are visible.

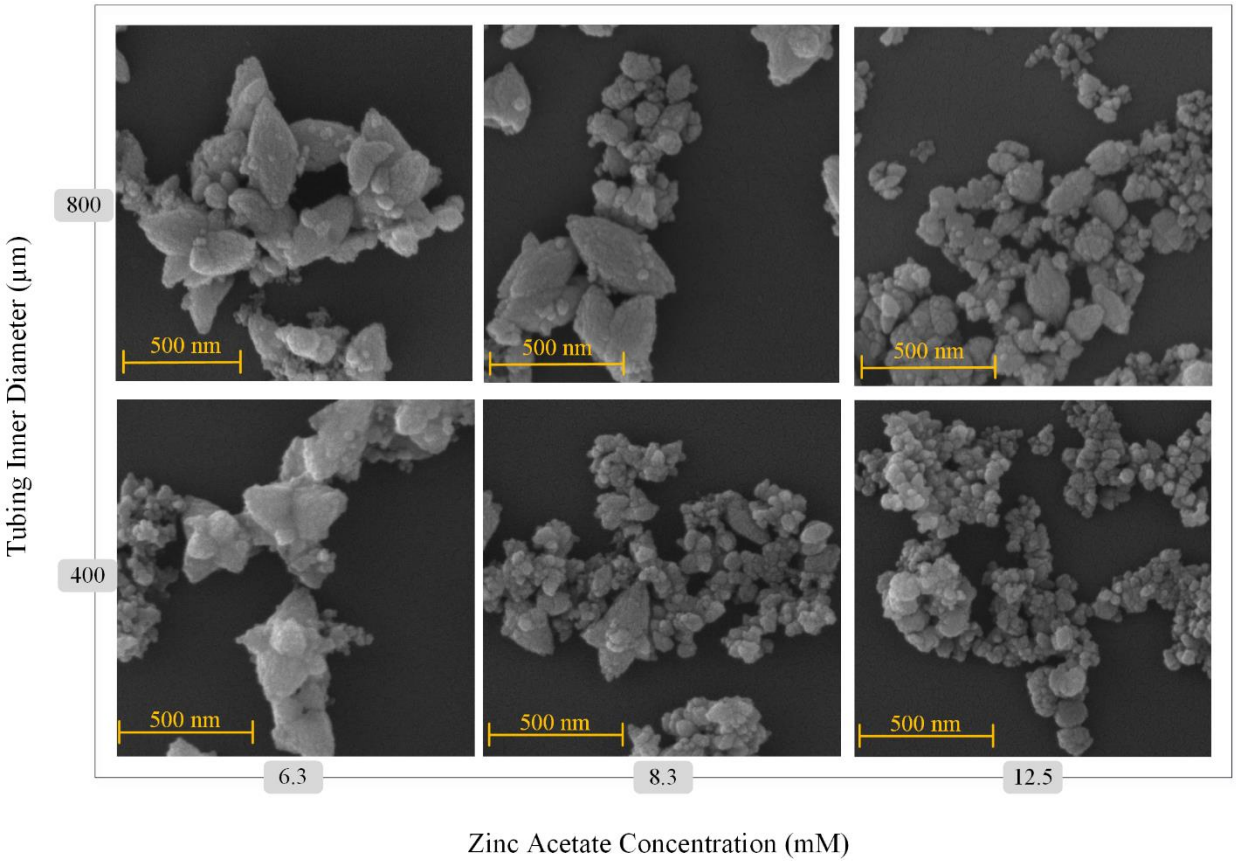

Figure 7.2: SEM micrographs for the zinc oxide products produced using different zinc acetate concentrations in both an 800 µm diameter reactor and a 400 µm diameter reactor. Inlet sodium hydroxide concentration was 0.025 M, reaction temperature was 60 ˚C, and residence time was 10 min for all trials.

Similar behavior was observed for the range of zinc acetate concentrations used with an inlet sodium hydroxide concentration of 0.05 M. Figure 7.3 shows that when an 800 µm reactor diameter was used, ellipsoidal mesocrystals were formed with a zinc acetate concentration of 12.5 mM. When the same concentration was used in the 400 µm, the oriented attachment of zinc oxide into a mesocrystal structure was greatly inhibited. The higher zinc acetate concentrations of 16.7 and 25 mM produced similar small spherical morphologies in both reactors. The overall behavior

seen in both reactor diameters was consistent, increasing zinc acetate and sodium hydroxide concentrations inhibited the formation of mesocrystals. As discussed earlier, this can primarily be attributed to the increase in zinc acetate concentration producing more acetate ligands which stabilize the zinc oxide nanoparticles against ordered aggregation. When the reactor diameter is decreased to 400 µm, however, the ability to form zinc oxide mesocrystals is more sensitive to the initial zinc acetate concentration.

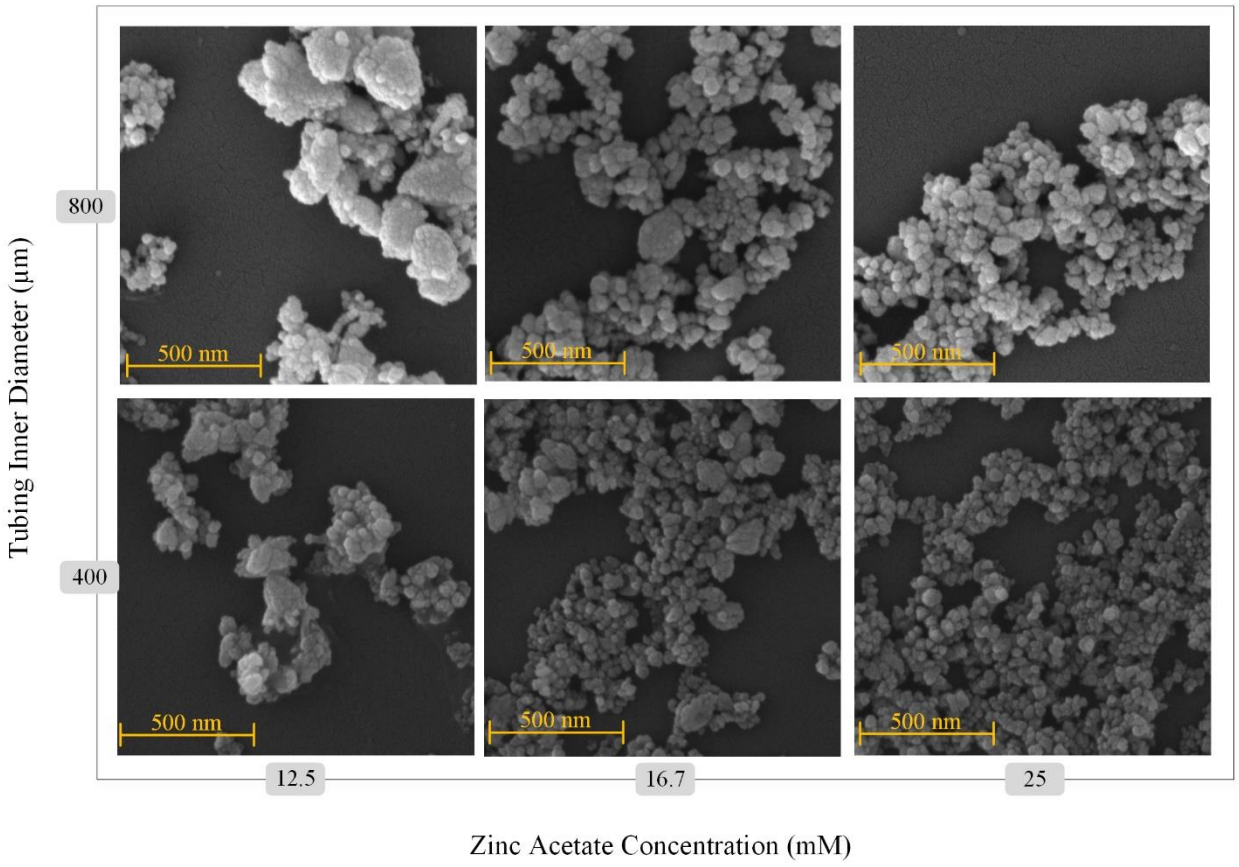

Figure 7.3: SEM micrographs for the zinc oxide products produced using different zinc acetate concentrations in both an 800 µm diameter reactor and a 400 µm diameter reactor. Inlet sodium hydroxide concentration was 0.05 M, reaction temperature was 60 ˚C, and residence time was 10 min for all trials.

As discussed previously in Chapter 6, the formation of zinc oxide mesocrystals in the interphase droplet reactor was more sensitive to reagent concentration than published experiments

using single phase batch reactors. As the reactor diameter was decreased to 400 µm and droplet volumes of 0.016 µL were used, the ability for zinc oxide mesocrystals to form was more sensitive to zinc acetate concentration. As the droplet volume and channel size is decreased, mass transfer and heat transfer should increase due to the smaller lengths involved and an enhancement in mixing. This should tend to favor a more rapid conversion of zinc acetate, leading to more rapid nucleation which should produce smaller primary nanoparticles [104]. If more rapid nucleation producing smaller nanoparticles was impacting the oriented attachment process, it should have been seen in the 6.3 mM zinc acetate / 0.025 M sodium hydroxide trial. Instead, that trial in the 400 µm diameter reactor was still able to form mesocrystals. When the tubing diameter is decreased, mixing is enhanced due to changes in the internal flow patterns of a translating droplet [91,131]. In single phase aqueous synthesis of zinc oxide in a continuous millifluidic reactor, the presence of Dean vortices was observed to impact the aggregation behavior of zinc oxide nanoparticles [19]. The transition from elongated aggregates to spherical aggregates was attributed to the increase in Dean vortices present in the reactor. While recirculating flow patterns are naturally present in droplet flow, the morphology changes observed in the 400 µm diameter reactor may be reflecting the changing flow patterns in the smaller droplets.

7.2 Scale Down with Higher Reagent Concentrations

In both the 800 and 400 µm diameter reactors, the use of higher zinc acetate concentrations with an inlet sodium hydroxide concentration of 0.1 M produced spherical nanoparticles. This is due to the ability of the acetate ions to adsorb onto the surface of zinc oxide, stabilizing the nanoparticles against oriented attachment. The size of the spherical nanoparticles is affected by decreasing the reactor diameter and the droplet volume. Table 7.1 shows the measured nanoparticle sizes when a zinc acetate concentration of 0.033 M and an inlet sodium hydroxide concentration

of 0.1 M was used in both reactor diameters. Smaller nanoparticles were produced in the 400 µm diameter reactor. Figure 7.4 shows the SEM micrographs of the zinc oxide nanoparticles produced from both reactor diameters using an inlet sodium hydroxide concentration of 0.1 M and a zinc acetate concentration range of 0.025 to 0.05 M.

Reaction conditions that promote rapid nucleation of nanoparticles can result in the formation of smaller sized particles. A high supersaturation ratio is needed to induce rapid nucleation, which requires a high reaction rate [101,151]. Rapid nucleation produces a large amount of small nanoparticles and consumes the reaction precursors in solution that could otherwise lead to subsequent growth of the precipitated nanoparticles [104]. For zinc oxide in particular, the rate of the formation and decomposition of the aqueous zinc hydroxide complexes that result from the reaction between Zn^{2+} and OH^- would control this process [101]. The scaling and transport changes that occurred when the reactor diameter was decreased from 800 µm to 400 µm were beneficial towards more rapid nucleation. Decreasing particle size with decreasing reactor diameter has been seen in the droplet flow synthesis of zeolite particles. Yu et al. decreased the droplet reactor diameter from 2 mm to 1 mm [181] and Pan et al. used three different diameters, 3, 1.5, and 1 mm [112]. The authors of both works attributed the decrease in particle size to the increase in internal circulation in the droplets induced by the smaller reactor diameter. In the droplet reactors used for zeolite synthesis and in the interphase droplet reactor used for this work, as the reactor diameter was decreased, the mixing in both the continuous and droplet phases were enhanced which would have produced better mass and heat transfer. The decrease in the droplet volume from 0.21 to 0.016 µL also decreased the moles of Zn^{2+} ions contained in a single droplet, which also would have decreased the time required for complete consumption of the Zn^{2+} ions.

Table 7.1: Average nanoparticle size produced using a zinc acetate concentration of 0.033 M and an inlet sodium hydroxide concentration of 0.1 M in the 400 µm diameter reactor and the 800 µm diameter reactor.

Reactor Diam. (µm)	Mean (nm)	Std. Dev. (nm)	CV
400	43	7	0.17
800	54	10	0.18

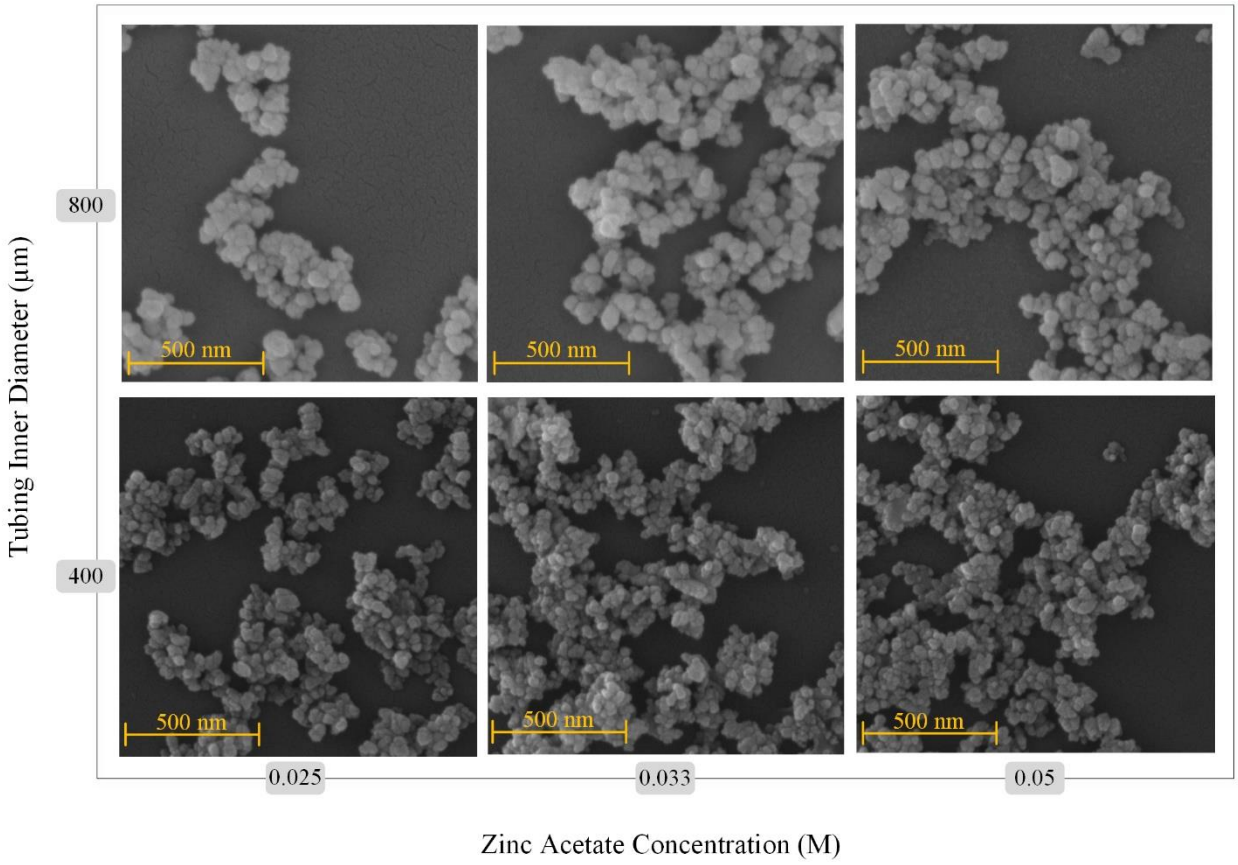

Figure 7.4: SEM micrographs for the zinc oxide products produced using different zinc acetate concentrations in both an 800 µm diameter reactor and a 400 µm diameter reactor. Inlet sodium hydroxide concentration was 0.1 M, reaction temperature was 60 ˚C, and residence time was 10 min for all trials.

As mentioned previously, for the trials presented in Figures 7.2, 7.3, and 7.4, the Reynolds number used in the two reactor diameters was kept constant at 0.49. This was done in an attempt to keep the transport behavior similar in both the reactor diameters. Decreasing the reactor

diameter while maintaining a constant Reynolds number, however, requires increasing the average fluid velocity. The increase in the average fluid velocity would affect the mixing in the droplet. The work presented in Chapter 5 showed a small decrease in average particle size as the fluid velocity was increased. More work will need to be done to determine the degree to which increasing fluid velocity versus decreased channel size plays a role in the particle morphology and size changes presented in this chapter.

7.3 Construction of Microfluidic Reactors for Nanoparticle Synthesis

Microfluidic reactors were constructed in an attempt to further investigate the effect of decreasing the interphase droplet reactor channel size on the synthesis of zinc oxide nanoparticles. Using the methods outlined in Chapter 3, microchannels with heights of approximately 60 µm and widths of 250 µm were constructed. As seen in Figure 7.5, these microchannels were able to form water droplets in a stream of 1-octanol. Based on the dimensions of the channel and the length of the droplet formed in Figure 7.5, the volume of the droplet in the image was approximately 3 nL [103]. Successful operation of a microfluidic interphase droplet reactor would have allowed the use of droplets at least an order of magnitude smaller than those shown previously in this chapter. Unfortunately, the materials available for constructing the microchannels did not produce a microreactor that was capable of stable operation when reagents were used. The proceeding work details the attempts made in the construction of an interphase droplet microfluidic reactor.

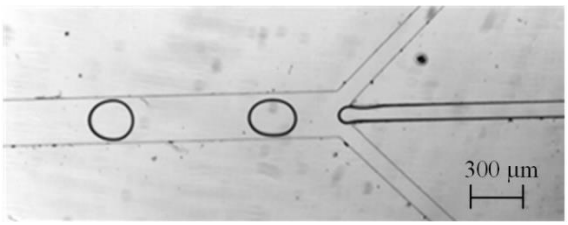

Figure 7.5: Pure water droplets formed in a stream of 1-octanol.

7.4 PDMS-Glass Channels

The optical clarity and ease of fabrication of PDMS makes it an ideal material for many microfluidic applications. The ease with which PDMS can bond to glass makes glass a common material for sealing PDMS channels [3]. After exposure to the oxygen plasma during the bonding step, both glass and PDMS are rendered hydrophilic. For stable aqueous droplet formation to occur, both materials must be hydrophobic to prevent the droplets from adhering to the walls of the channels. A facile way of reversing the hydrophilicity is to heat the sealed channel at 95˚C for 12 hours. For both PDMS and glass the heating step causes hydrophobic recovery to occur, though through different mechanisms for each material [55,62]. As seen in Figure 7.6(a), the heat treatment of the microchannel rendered both the PDMS and the glass hydrophobic enough to support the stable formation of water droplets in a pure stream of 1-octanol. When a stream of sodium hydroxide in 1-octanol was used instead of pure 1-octanol, the droplets quickly wet the channel walls after being formed, as seen in Figure 7.6(b). Figure 7.6(b) shows that droplets were able to initially form, indicating that the sodium hydroxide in 1-octanol stream did not modify the hydrophobicity of the channel. Instead, the wetting behavior was seen downstream from where the droplets were being formed. Fouling from sodium hydroxide precipitating from the continuous phase were most likely inducing the wetting behavior observed.

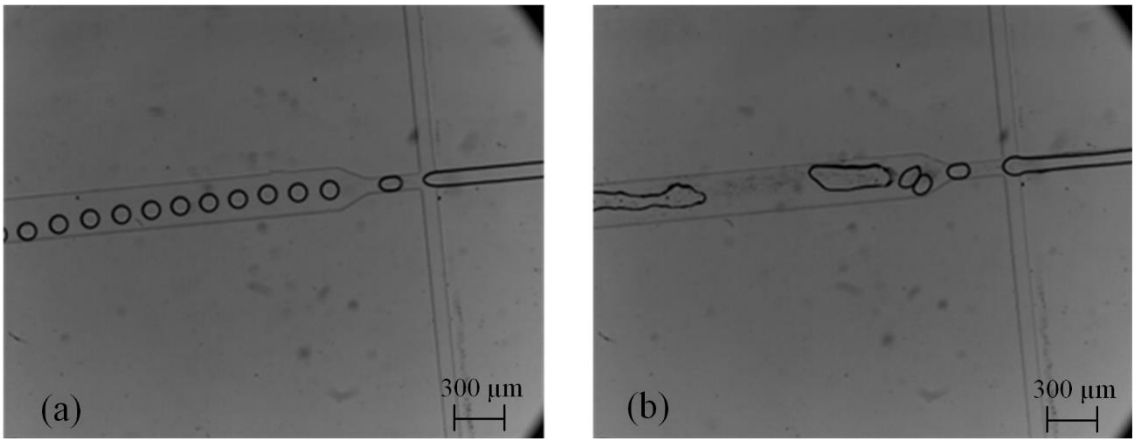

Figure 7.6: (a) PDMS-glass microchannel forming stable water droplets in octanol after heat treatment. (b) PDMS-glass microchannel showing droplet wetting of the channel after the introduction of the sodium hydroxide in 1-octanol.

Rain-X is a commercially available liquid for rendering glass hydrophobic and is used in microfluidics for that purpose as well [66]. The channels constructed from Rain-X treated glass were able to form water droplets in pure 1-octanol. When a stream of sodium hydroxide in 1-octanol was used as the continuous phase, the water stream began to wet the channel walls, as shown in Figure 7.7. Silicone oil infused PDMS was also tested as a surface modification method. Silicone oil infused PDMS has been shown to maintain hydrophobicity of the PDMS surface and also decrease the friction of the surface [95]. Since the wetting issues shown previously were possibly attributed to solid sodium hydroxide adhering to the microchannel walls, infusing the PDMS with silicone oil was a possible remedy. When the PDMS was infused with 10 cSt silicone oil prior to oxygen plasma exposure, bonding with the glass slide was completely prevented. When the PDMS was infused with 10 cSt silicone oil after bonding with the glass slide, the PDMS microchannel delaminated from the glass slide. This is most likely due to the large swelling that PDMS can undergo when infused with silicone oil [97] and the inability of the glass to deform to accommodate the swelling.

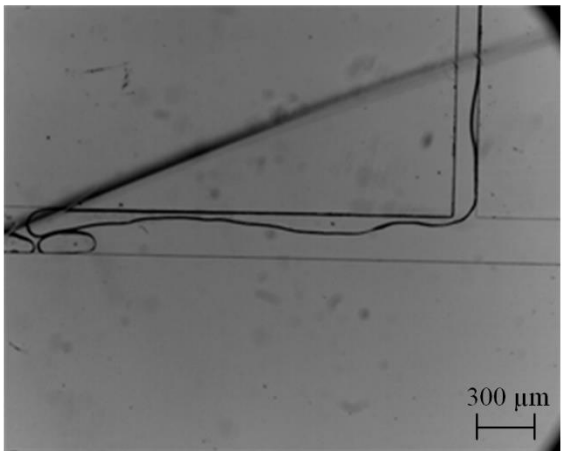

Figure 7.7: Rain-X treated microchannel showing the water stream wetting the walls of the microchannel.

7.5 PDMS-PDMS Channels

To determine if the wetting issue in the microchannels sealed using a glass slide was due to glass being used to seal the channels, PDMS microchannels were sealed with a flat slab of PDMS, using the procedure outlined in Chapter 3. Surface modification methods were then tested on the PDMS-PDMS microchannels. When Rain-X was used as a surface modification method, fouling and droplet wetting were still observed in the PDMS-PDMS microchannels.

Oil infusion of the PDMS-PDMS microchannels was accomplished by immersing the bonded channels in 10 cSt silicone oil. Stable droplet formation of water droplets in pure octanol was observed at the inlet of the droplet reactor in Figure 7.8(a). This demonstrates that the PDMS walls were hydrophobic, preventing the droplets from wetting the walls. As the droplets traveled downstream through the reactor, they passed the sodium hydroxide in 1-octanol inlet, seen in Figure 7.8(b). While there was a streak of solids fouling the centerline of the channel, the droplets did not appear to interact with the wall. Downstream of the sodium hydroxide inlet and near the outlet of the reactor, Figure 7.8(c), stable droplets were still observed. On the right side of the

image, however, channel leaking can be observed. To account for poor bonding at this location, two more droplet reactor chips were made and tested and showed similar leaking. The silicone oil infusion may have weakened the bonding between the two PDMS layers or the accumulation of solids in the channel created a pressure build up, causing a leak to occur.

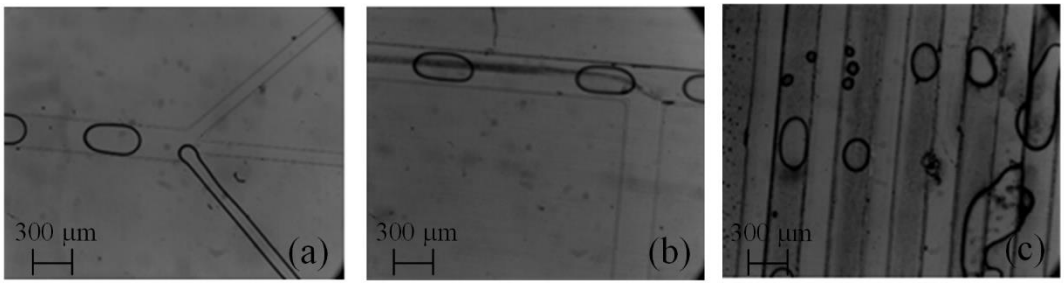

Figure 7.8: (a) Pure water droplet formation in a stream of pure 1-octanol. (b) Water droplets passing the inlet for the sodium hydroxide in 1-octanol stream. (c) Channels near the outlet of the reactor, showing leaking on the right side.

7.6 Polyester Microchannels

Polyester is a thermoset polymer that can be used as an alternative material of construction to PDMS. It is commercially available as a resin that is cured with a MEKP catalyst. Polyester has good properties for a microfluidic droplet reactor: it is natively hydrophobic [37], has good solvent resistance [38], is optically clear, and cures slow enough for any bubble present in the liquid resin to rise to the surface. Polyester microchannels were successfully fabricated using the methods described in Chapter 3.

As seen in Figure 7.9(a), stable droplet formation was possible in the polyester microchannel. When the droplets approached the inlet of the sodium hydroxide in 1-octanol stream, however, they instantly wetted the channel wall. Figure 7.9(b) shows the wetting behavior, making native polyester an unsuitable material to construct the microfluidic droplet reactor out of. To prevent the wetting behavior seen in Figure 7.9(b), the microfluidic droplet reactor was treated

with Rain-X. Residual Rain-X in the channel, however, appeared to react with the water and octanol, leaving solid deposits on the channel wall. The Rain-X also appeared to interfere with the epoxy used to glue the tubing into the inlets of the microchannels. Every inlet of the microfluidic reactor leaked after Rain-X treatment, rendering the channel inoperable. In contrast, the same epoxy was used on the native polyester channel in Figure 7.9 and no leaking was observed.

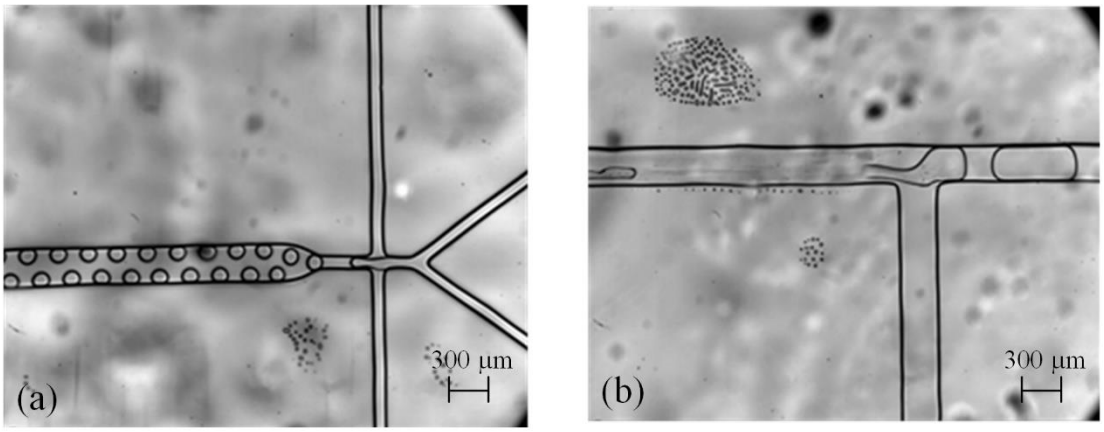

Figure 7.9: (a) Stable formation of pure water droplets in pure 1-octanol at the inlet of the polyester microfluidic reactor. (b) Wetting of the channel walls by water droplets as they approach the inlet of the sodium hydroxide in 1-octanol stream.

7.7 Polyurethane Microfluidic Droplet Reactor

Polyurethane is a polymer that has also been reported as an alternative to constructing microchannels from PDMS. The properties of polyurethane make it suitable for many microfluidic applications. It is natively hydrophobic, it can be optically clear, and it has been reported that polyurethane can be plasma bonded [32]. Optically clear polyurethane that is commercially available and used in previously reported polyurethane microfluidic devices, Clear Flex 50 (Smooth-On), uses phenylmercury neodecanoate as a curing catalyst. Due to the health concerns of using polyurethane containing phenylmercury neodecanoate [20], an alternative polyurethane, Econ 60 (Smooth-On), was used. Econ 60 is an amber colored polyurethane but is translucent enough to see the casted microchannels when using a microscope.

While it was possible to cast microfluidic channels into the Econ 60 polyurethane, as seen in Figure 7.10, there was no success in making fully sealed microfluidic reactors with this material. All the microfluidic reactors made with the Econ 60 polyurethane leaked between the two pieces of polyurethane. Table 7.2 lists all the bonding steps that were used when attempting to create a sealed polyurethane microfluidic reactor. Due to every microchannel leaking, no droplet formation tests could be performed. Beyond the leaking issue, Econ 60 cures too rapidly to degas or to allow any air bubbles to naturally rise to the surface. The air bubbles introduced into the liquid pre-polymer during mixing remained trapped in the cured polymer. This both obscures viewing the channel on a microscope and impairs the integrity of the channels if the air bubbles are trapped on the surface of the mold. If, in the future, there is a bonding method found that will work for these polyurethane channels, this material may still be worth investigating.

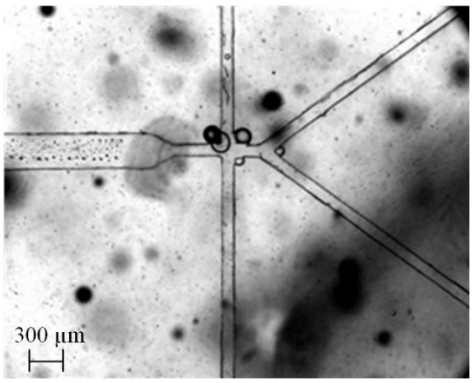

Figure 7.10: Inlet region of the polyurethane microfluidic reactor.

Table 7.2: Attempted bonding steps for polyurethane microfluidic channels.

Bonding Step	Post Bonding Step	Result
Oxygen plasma, 15 s exposure	1 hour, room temperature	Leak
Oxygen plasma, 30 s exposure	1 hour, room temperature	Leak
Oxygen plasma, 30 s exposure	12 hours, 65˚C	Leak
Joining pieces after partially curing for 40 minutes	12 hours, room temperature	Leak
Joining pieces after partially curing for 40 minutes	12 hours, 65˚C	Leak

Chapter 8: Synthesis of Copper Oxide

Copper oxide was synthesized using the interphase droplet reactor to demonstrate the reactor's ability to produce other metal oxides. To produce copper oxide, a copper salt is hydrolyzed by a base to first form copper hydroxide which then proceeds to copper oxide, as described in Eqns. (8.1) – (8.3) [71]. When hydroxide ions are present, $Cu(OH)_2$ rapidly dissolves forming $Cu(OH)_4^{2-}$. The decomposition of $Cu(OH)_4^{2-}$ through the loss of the hydroxyl groups, then produces copper oxide [22].

$$Cu^{2+}(aq) + 2OH^{-}(aq) \rightarrow Cu(OH)_2\ (s) \tag{8.1}$$

$$Cu(OH)_2\ (s) + 2OH^{-}(aq) \rightarrow [Cu(OH)_4]^{2-}(aq) \tag{8.2}$$

$$[Cu(OH)_4]^{2-}(aq) \rightarrow CuO(s) + 2OH^{-}(aq) + H_2O\ (l) \tag{8.3}$$

Studies on the aqueous synthesis of copper oxide nanoparticles has shown that large excesses of hydroxide ions are not needed to produce copper oxide. Reaction solutions with a neutral pH or a 1:1 stoichiometric ratio between Cu^{2+} and OH^- have been shown to produce copper oxide [145,191]. When reactions have been conducted at high temperatures, acetic acid was added to the copper acetate solution to prevent the hydrolysis of the copper acetate before the addition of a base. Acetate ions can also adsorb onto the surface of copper oxide, inhibiting growth and attachment processes [71].

In this chapter, the synthesis of copper oxide nanostructures using the interphase droplet reactor is investigated. The effects of total reagent concentration, the presence of acetic acid, sodium hydroxide concentration and zinc acetate formation on the synthesis of copper oxide were investigated. The reaction parameters for all experiments discussed here were a temperature of

60˚C, a total flow rate of 0.165 mL/min, and a residence time of 10 minutes. The initial aqueous droplet solution was the characteristic blue of copper solutions. When the droplets exited the reactor they contained black solids, the typical color of copper (II) oxide.

8.1 Effect of Total Concentration

The formation of ordered copper oxide structures is known to be dependent on the reagent concentrations used during synthesis. Both hydroxide and acetate ions can adsorb onto copper oxide, impacting the attachment process [71,178]. To investigate the effects of total reagent concentration on the synthesis of copper oxide in the interphase droplet reactor, two trials were conducted with a constant ratio between the inlet sodium hydroxide concentration and the initial copper acetate concentration. Figure 8.1 shows the comparison between the products formed using 2.5 mM copper acetate and an inlet sodium hydroxide concentration of 0.025 M and a trial using a copper acetate concentration of 5 mM and an inlet sodium hydroxide concentration of 0.05 M. Both trials produced plate structures, with no significant differences in morphology.

Close examination of the plate structures show that they consist of aggregated copper oxide nanowires. The ordered attachment of the nanowires occurred parallel to the long axis of the plates. Copper oxide plate mesocrystals have been observed in batch synthesis reactions [16,178]. The proposed mechanism for the formation of the plate structures begins with the growth of nanowires [178]. The nanowires grow in the [010] direction, which increases the size of the polar (001) and (100) surfaces. The nanowires attach along the (100) surfaces in order to decrease the surface energy. Attachment along the (001) surface is inhibited due to the tendency of hydroxide ions to selectively adsorb onto the (001) surface. The inability for attachment to occur on the (001) surface leads to the creation of the flat plate copper oxide mesocrystal.

Decreasing the inlet sodium hydroxide concentration to 0.025 M would have decreased the rate of mass transfer into the droplets by decreasing the driving force. It also would have decreased the reaction kinetics, since the formation of copper oxide from copper hydroxide is enhanced by high hydroxide ion concentrations. Figure 8.1, however, does not show that the lower 0.025 M sodium hydroxide concentration affected the morphology of the copper oxide plates. The ratio between the sodium hydroxide and copper acetate is high enough to promote anisotropic growth in both trials. Concurrently, either the concentrations of the hydroxyl or acetate ions were still high enough in the 2.5 mM trial to stabilize the exposed planes of the copper oxide to prevent 3D aggregation. 3D attachment of copper oxide is suppressed by the adsorption of hydroxyl ions on the (001) surface of the 2D plate. Adsorption of acetate ions on the (001) surface would also be favored due to the high surface density of copper atoms [100,183,186].

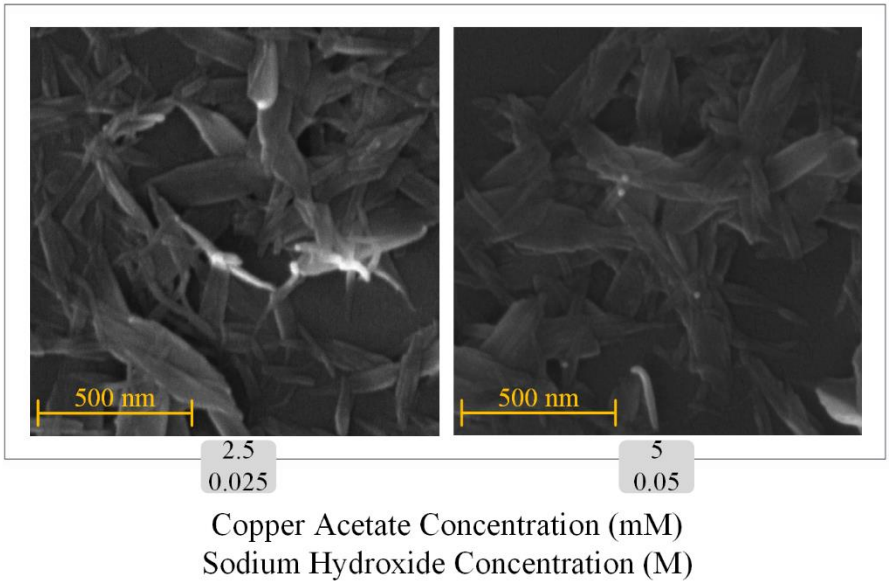

Figure 8.1: SEM micrographs showing the effect of total reagent concentration of mesocrystal formation. Reaction temperature was 60˚C and residence time was 10 min.

Figure 8.2 shows the XRD spectra for the product of the 5 mM copper acetate trial, showing that the product is copper (II) oxide. There are three stable forms of copper oxide, CuO, Cu_2O, and Cu_4O_3 [99]. CuO was the expected product based on the reaction conditions used in the interphase droplet reactor. Since copper acetate was used as the copper salt for these trials, the Cu^{2+} ion was in solution. To form either Cu_2O or Cu_4O_3, a reducing agent would have been needed to reduce the Cu^{2+} ions.

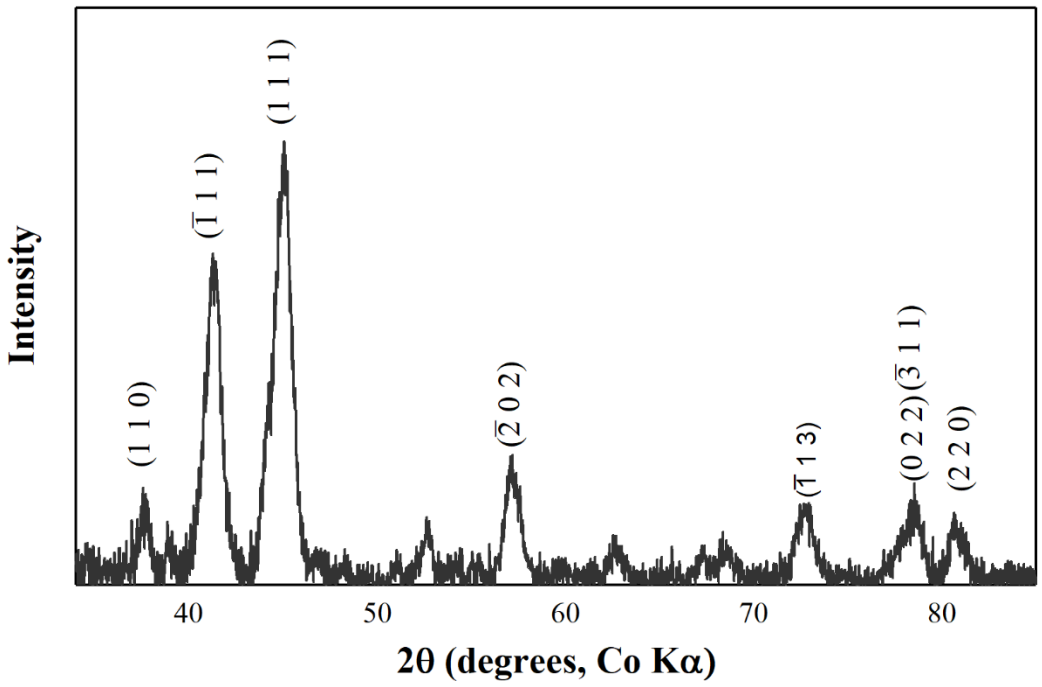

Figure 8.2: XRD data for copper oxide produced from trial using 5 mM copper acetate solution.

8.2 Effect of Acetic Acid

Acetic acid has been used in reported synthesis of copper oxide nanoparticles to prevent the hydrolysis of copper acetate at elevated temperatures in the absence of an added base [191]. When acetic acid dissociates in solution, an acetate and hydrogen ion are formed. Acetate ions are

known to adsorb onto the surface of copper oxide, affecting growth and attachment processes [71]. The addition of acetic acid to the droplet phase was investigated due to its potential impact on the morphology of the copper oxide mesocrystals. Figure 8.3 shows the copper oxide structures formed with and without the presence of acetic acid. When acetic acid is present in the initial droplet solution, there is a limited amount of attachment into a plate morphology but the primary morphology is the nanowire shape. When the same copper acetate and sodium hydroxide concentrations are used without the addition of acetic acid, copper oxide plates are formed. The ordered aggregation of the copper oxide nanowires occurs due to attachment of the (100) planes. The (100) surface also has a high density of surface copper atoms which can coordinate with acetate ions [186]. The presence of the acetate ions on this surface would inhibit the attachment of the nanowires. Growth can still occur along the [010] direction due to the lower density of surface copper atoms of (010) having a decreased ability to coordinate with acetate ions, allowing the nanowire morphology to still form.

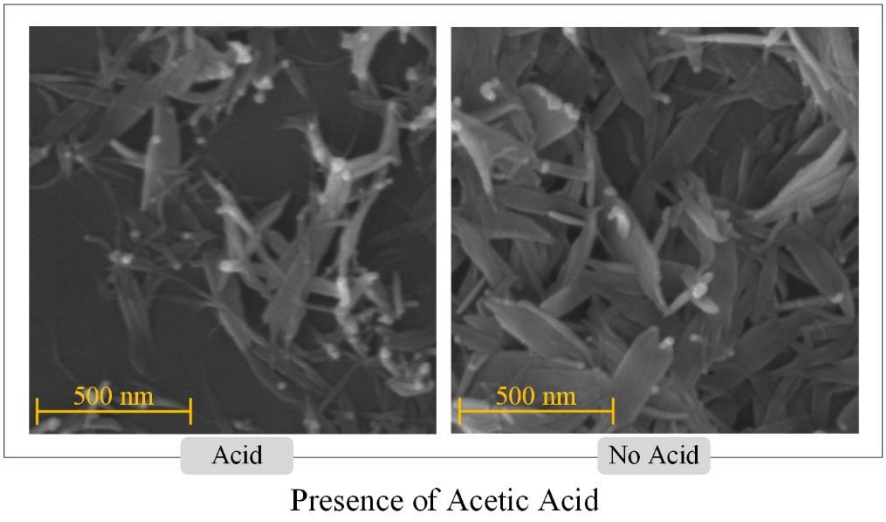

Figure 8.3: SEM micrographs of presence of acetic acid affecting the formation of mesocrystals. Inlet sodium hydroxide concentration was 0.05 M, initial copper acetate concentration was 0.01 M. Acetic acid concentration, when used, was 0.029 M. Reaction temperature was 60˚C and residence time was 10 min.

8.3 Effect of Sodium Hydroxide Concentration

The effect of increasing sodium hydroxide concentration was investigated with a droplet phase containing constant copper acetate and acetic acid concentrations. Figure 8.4 shows the effect of two different inlet sodium hydroxide concentrations with a constant copper acetate concentration on the morphology of the copper oxide nanoparticles. The products synthesized using an inlet sodium hydroxide concentration of both 0.05 and 0.1 M showed the nanowire morphology. The nanowires produced from the 0.05 M trial, however, showed a degree of ordered attachment into a plate or sheet shape. The nanowires produced from using an inlet sodium hydroxide concentration of 0.1 M did not show the same tendency toward ordered attachment. While the nanowires are aggregated, there is not a visible order present in the aggregates. Hydroxide ions are known to adsorb onto the surface of copper oxide and can interfere with the oriented attachment of copper oxide nanoparticles. As can be seen in Figure 8.4, the nanowires overlapped each other when deposited on the SEM stub. The high degree of overlapping made it difficult to measure the lengths of a large number of nanowires in order to produce an accurate measure of the average lengths and widths. The nanowires produced from the 0.05 M sodium hydroxide trial had an average length of approximately 286 nm and an average width of approximately 20 nm. The 0.1 M sodium hydroxide trials had an average length of approximately 221 nm and an average width of approximately 27 nm.

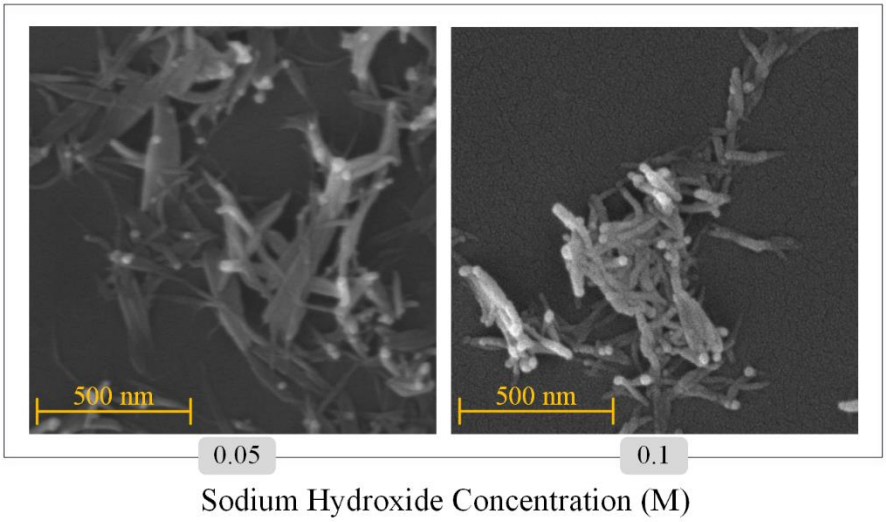

Figure 8.4: SEM micrographs showing the effect of inlet sodium hydroxide concentration on particle morphology. Initial copper acetate concentration was 0.01 M and acetic acid concentration was 0.029 M. Reaction temperature was 60˚C and residence time was 10 min.

8.4 Effect of Copper Acetate Concentration

The effect of copper acetate on the synthesis of copper oxide was investigated by using two different copper acetate concentrations, 0.01 M and 0.02 M, with a constant inlet sodium hydroxide concentration of 0.1 M. Acetic acid was also used in the two trials shown in Figure 8.5, the 0.01 M copper acetate trial contained 0.029 M acetic acid while the 0.02 M copper acetate trial contained 0.058 M acetic acid. In Figure 8.6, both 0.01 and 0.02 M copper acetate concentrations produced nanowire morphologies. As with Figure 8.4, the nanowires do not attach into ordered structures for either concentration. The overlapping of the nanowires seen in Figure 8.5 prevented measurement of the lengths and widths of a large number of nanowires. The 0.01 M copper acetate trial, as stated in Section 8.3, produced nanowires with approximate average lengths and widths of 221 nm and 27 nm respectively. The 0.02 M copper acetate trial produced nanowires with approximate average lengths and widths of 308 nm and 27 nm respectively. Figure 8.6 shows the EDS spectrum for the 0.01 M copper acetate trial and Table 8.1 shows the elemental composition

calculated from the EDS spectrum. The silicon peak in Figure 8.6 is from the silicon wafer substrate used for imaging the samples in the SEM. For copper (II) oxide the ratio between copper and oxygen should be 1:1, however, Table 8.1 shows a small excess of oxygen. The excess oxygen may be present in the form of surface hydroxyl groups or in the surface oxide layer of the silicon substrate. Figure 8.7 shows the XRD spectrum for the 0.02 M copper acetate trial. The characteristic ($\bar{1}11$) and (111) peaks of copper (II) oxide are seen. The lack of clear peaks at higher values of 2θ was due to the small sample mass that was available for the analysis.

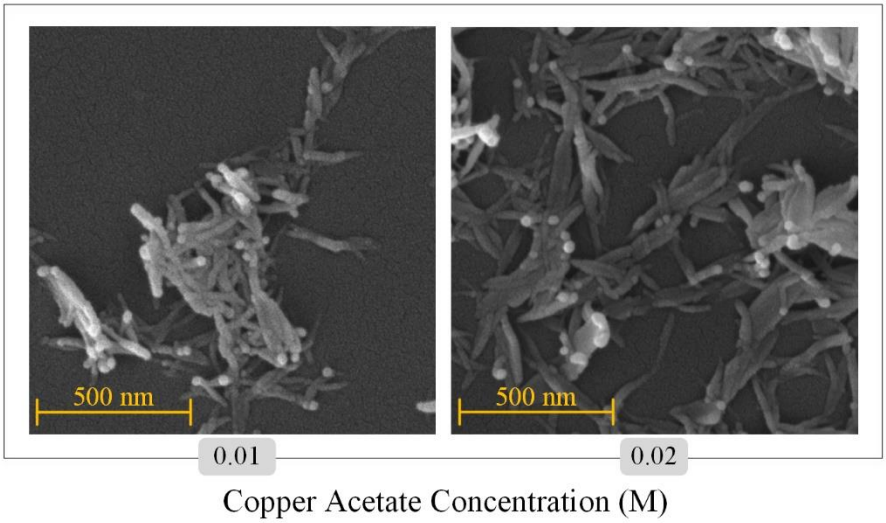

Figure 8.5: SEM micrograph showing the effect of copper acetate concentration on particle morphology. For the 0.01 M trial, acetic acid concentration was 0.029 M. For the 0.02 M trial, acetic acid concentration was 0.058 M. The inlet sodium hydroxide concentration was 0.1 M, reaction temperature was 60˚C and residence time was 10 min.

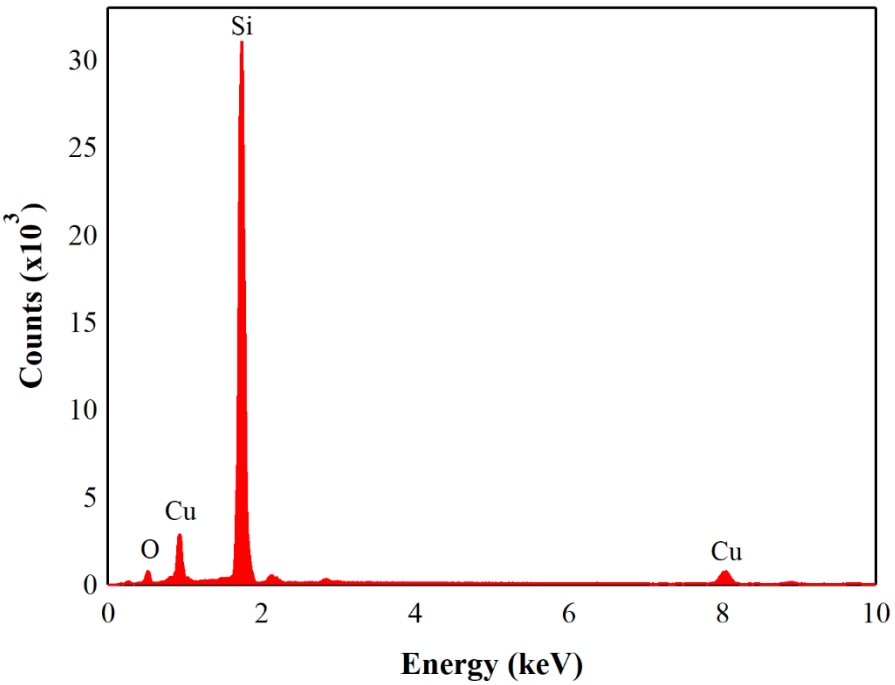

Figure 8.6: EDS spectrum for the 0.01 M copper acetate trial.

Table 8.1: EDS elemental composition results for the 0.01 M copper acetate trial.

Element	Atomic %	Error %
O	51.64	10.19
Cu	48.36	3.67

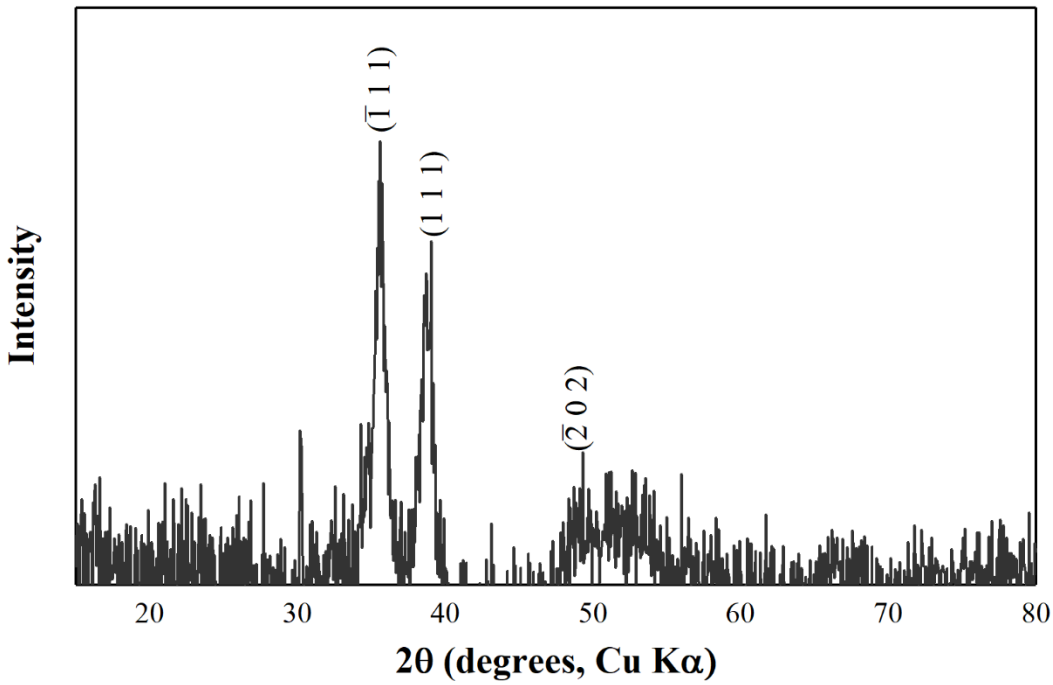

Figure 8.7: XRD data for the 0.02 M copper acetate trial.

Interestingly, the 0.02 M copper acetate trial still forms nanowires despite the presence of a higher concentration of acetate ions. Zhu et al. reported the synthesis of ellipsoidal copper oxide structures using a copper acetate concentration of 0.02 M and a 0.058 M acetic acid concentration [191]. The ellipsoidal structures were obtained by adding the sodium hydroxide to the solution at room temperature and then increasing the reaction temperature to 100˚C. The authors stated this was a mild reaction condition, favoring lower nucleation rates which promoted the formation of the copper oxide mesocrystals. Konar et al. reported the ability of acetate ions to strongly inhibit growth and attachment of copper oxide nanoparticles when compared to other organic acids [71]. Small spherical copper oxide nanoparticles were formed using a 0.1 M copper acetate concentration and a 0.2 M acetic acid concentration. The synthesis was initiated by the addition of sodium hydroxide solution to the 100˚C acidic copper acetate solution. When Zhu et al. added sodium hydroxide to 100˚C acidic copper acetate solution, small spherical copper oxide

nanoparticles were formed as well. Both the reaction rate and presence of acetate ions affects the morphology of the resulting copper oxide nanoparticles. The trials conducted using the interphase droplet reactor at 60˚C favor the formation of the nanowire morphology. The concentration of the reagents at this temperature control the ability of the nanowires to aggregate into plate mesocrystals.

Chapter 9: Summary

The work presented in this dissertation demonstrated the synthesis of metal oxide nanoparticles in an interphase droplet reactor. The droplet merging and mass transfer behavior of the reactor was characterized. Zinc oxide nanoparticles were synthesized using the interphase droplet reactor and the effect of reaction temperature, reagent concentration, flow rate, residence, and droplet volume, on particle size and morphology was studied. The diameter of the interphase droplet reactor was decreased to study how reactor scale affected the size and morphology of the particles produced. The ability of the interphase droplet reactor to synthesize other metal oxide nanoparticles was demonstrated through the synthesis of copper oxide.

The mass transfer behavior of the interphase droplet reactor was characterized by using an acid-base titration. Aqueous droplets of hydrochloric acid were formed in the reactor and contained the pH indicator methyl orange. The transfer of sodium hydroxide from the continuous phase to the droplet phase neutralized the hydrochloric acid in the droplets and increased the droplet pH. When the pH increased to 4.4, the methyl orange indicator changed from red to yellow. The time required for the color change to occur was measured for different system parameters. Increasing the total flow rate was found to decrease the time required for the color change to occur. Increasing the droplet volume, at a constant flow rate, was found to increase the time required for the color change to occur. When the droplet volume was accounted for, the rate of sodium hydroxide into the droplets was found to increase with increasing droplet volume. The surfactants Triton X-100 and sodium dodecyl sulfate were used to investigate the effect of surfactants on the rate of mass transfer. When Triton X-100 was used, a concentration of 0.01 mM was found to slightly decrease the rate of mass transfer, compared to a clean system. Triton X-100 concentrations of 0.1 and 1

mM were found to increase the rate of mass transfer. The use of a sodium dodecyl sulfate concentration of 0.1 mM decreased the rate of mass transfer while a concentration of 1 mM produced the same mass transfer rate as the clean system.

The synthesis of zinc oxide nanoparticles in the interphase droplet reactor was investigated using an inlet sodium hydroxide concentration ranging from 0.1 to 0.5 M with a zinc acetate concentration ranging from 0.025 to 0.075 M. The effect of reaction temperature on the size and morphology of the zinc oxide nanoparticles was investigated using reaction temperatures from 25 to 80˚C. A reaction temperature of 25˚C produced aggregated zinc oxide sheets. Increasing the reaction temperature to 40˚C transitioned the morphology to spherical nanoparticles with a mean size of 45.4 nm. Reaction temperatures of 60 and 80˚C yielded spherical nanoparticles with 54 and 52 nm mean sizes respectively. The effect of zinc acetate concentration on the size of zinc acetate concentration was investigated using an inlet sodium hydroxide concentration of 0.1 M with zinc acetate concentrations from 0.025 M to 0.075 M. At all concentrations spherical zinc oxide nanoparticles were produced, with 0.025 M and 0.075 M zinc acetate yielding 50 nm and 61 nm mean particle sizes respectively. The effect of inlet sodium hydroxide concentration with a constant zinc acetate concentration on particle morphology was investigated. Both the 0.3 M and 0.5 M sodium hydroxide trials produced agglomerated plate-like particles.

The effect of residence time on particle size was studied by using 5, 10 and 20-minute residence times. The 5 min, 10 min, and 20 min trials produced 42, 54, and 50 nm mean particle sizes respectively. The effect of total flow was investigated by doubling the total flow through the reactor while using an inlet sodium hydroxide concentration of 0.1 M and a zinc acetate concentration of 0.033M. Increasing the total flow rate produced a small decrease in the mean particle size from 54 nm to 52 nm. Three different initial droplet volumes were used to study how

droplet volume affected the mean particle size. Using a constant flow rate, trials using 0.044, 0.25, and 1.13 µL droplet volumes were conducted and produced mean particles sizes of 46, 54, and 48 nm respectively. A trial was also conducted using the addition of 1 mM sodium dodecyl sulfate to the droplet phase to study the effect of a surfactant on the particle size and morphology. The trial still produced spherical particles but the mean particle size was reduced from 54 nm to 43 nm.

The particles produced using the interphase droplet reactor were also compared against the products from a single phase aqueous batch reactor. Both the batch and droplet flow reactor trials used initial sodium hydroxide concentrations of 0.1 M and zinc acetate concentrations of 0.025, 0.033 and 0.05 M. The reactions were conducted at 60˚C and with a residence time of 10 minutes. Across all three zinc acetate concentrations, the droplet flow reactor produced particles with a narrower particle size distribution compared to the batch reactor. The interphase droplet reactor also produced a uniform spherical particle morphology, while the batch reactor produced a mix of particles and plates.

The conditions necessary for zinc oxide mesocrystal formation using the interphase droplet reactor were identified. Using an inlet sodium hydroxide concentration of 0.025 M and zinc acetate concentrations of 6.3 and 8.3 mM, ellipsoidal zinc oxide mesocrystals were formed through oriented attachment. Increasing the zinc acetate concentration to 12.5 mM began to inhibit the ability for the mesocrystals to form and a 16.7 mM concentration completely prevented the oriented attachment process. When the inlet sodium hydroxide concentration was increased to 0.05 M, a zinc acetate concentration of 12.5 mM still produced some ellipsoidal mesocrystals. When the zinc acetate concentration was decreased to 8.3 and 6.3 mM, highly agglomerated ellipsoidal mesocrystals were formed, indicating that the structures had possibly began to dissolve. The dissolution and agglomeration behavior seen in the 8.3 mM zinc acetate trial occurred at $[Zn^{2+}]$:

$[OH^-]$ = 1:6. Similar behavior was seen when $[Zn^{2+}]$: $[OH^-]$ = 1:6 was used with sodium hydroxide concentrations of 0.1 and 0.3 M. Zinc acetate concentrations of 16.7 and 25 mM produced smaller spherical nanoparticles. The effect of reaction temperature was investigated by operating the interphase droplet reactor at 25, 40, and 60˚C. A reaction temperature of 25˚C produced an amorphous solid that did not form any mesocrystals. Reaction temperatures of 40 and 60˚C were high enough to for the oriented attachment process to form ellipsoidal mesocrystals.

The effect of residence time on the formation of zinc oxide mesocrystals was investigated using 2, 5, and 10-minute residence times. The 2-minute residence time showed that ellipsoidal mesocrystals were able to form rapidly in the interphase droplet reactor. There were not significant morphology changes when the residence time was increased from 5 to 10 minutes. The mass transfer behavior of the reactor was changed by using three different initial droplet volumes, 0.21, 0.98, and 1.7 µL. Mesocrystals were able to form in all three droplet volumes, however, the structures formed in the 1.7 µL droplets were smaller and more spherical. The effect of surfactant concentration in the droplet phase on the ability of mesocrystals to form was studied using two different surfactants, Triton X-100 and SDS, with concentrations of 0.01, 0.1 and 1 mM. Across all the Triton X-100 concentrations used, mesocrystals were still able to form. A SDS concentration of 0.1 mM began to interfere with the oriented attachment of the nanoparticles and a concentration of 1 mM completely inhibited the formation of mesocrystals.

The effect of reactor diameter was studied by decreasing the reactor diameter from 800 to 400 µm. The Reynolds number of 0.49 was the same for both reactor diameters. Synthesis trials were conducted in the 400 µm reactor using inlet sodium hydroxide concentrations of 0.025, 0.05 and 0.1 M. When the sodium hydroxide concentration of 0.025 M was used with a zinc acetate concentration of 6.3 mM, ellipsoidal particles were formed. When the zinc acetate concentration

was increased to 8.3 mM, however, smaller spherical aggregates were more prevalent then the larger ellipsoidal mesocrystals. The trial conducted using a zinc acetate concentration of 12.5 mM did not produce ellipsoidal mesocrystals. When the sodium hydroxide concentration was increased to 0.05 M and a zinc acetate concentration of 12.5 mM was used, the ability to form mesocrystals was also greatly inhibited. The trials using a zinc acetate concentration of 16.7 and 25 mM produced primarily spherical particles. In the trials using 0.025 and 0.05 M sodium hydroxide in the 400 µm diameter reactor, mesocrystal formation showed a greater sensitivity to reagent concentration than in the 800 µm reactor. A comparison between the mean particle size produced in the 800 µm diameter reactor and the 400 µm reactor was made. The trials in both reactors that used a sodium hydroxide concentration of 0.1 M and zinc acetate concentration of 0.033 M was used for the comparison. The 800 µm diameter reactor produced a mean particle size of 54 nm while the 400 µm reactor produced a mean particle size of 43 nm. Attempts were made to scale the interphase droplet reactor down further using microfluidic reactors. No material of construction, however, was found to be suitable for the reactor.

Copper (II) oxide was synthesized to demonstrate the ability of the interphase droplet reactor to synthesize other metal oxide nanostructures. Copper oxide nanosheet mesocrystals were formed using a sodium hydroxide concentration of 0.025 M and a copper acetate concentration of 2.5 mM as well as a sodium hydroxide concentration of 0.05 M with a copper acetate concentration of 5 mM. The presence of acetic acid in the droplet phase was found to inhibit the formation of the copper oxide nanosheets. When a sodium hydroxide concentration of 0.1 M was used with a copper acetate concentration of 0.01 and 0.02 M and the addition of acetic acid, copper oxide nanowires were formed.

9.1 Future Work

Methods of preventing droplet merging in the droplet reactor should be investigated. Maintaining a monodisperse droplet volume will help to produce a uniform nanoparticle product from the reactor. These methods may include changing droplet spacing, modifying flow rates, or the use of different surfactants.

The ability of surfactants to affect the rate of mass transfer in an interphase droplet reactor should be investigated further. The majority of the published work in this area is for either stationary droplets or for droplets undergoing buoyancy driven motion. There remains more to learn about the behavior of surfactants in pressure driven droplet flow with mass transfer occurring.

As shown in this work, when the reactor diameter was decreased the sensitivity of the oriented attachment process to reagent concentration increased. Computational fluid dynamic and molecular dynamics simulations may be required to fully understand the mechanism behind this observation.

The use of different inorganic hydroxides such as potassium hydroxide and lithium hydroxide should be investigated. These reagents will have different mass transfer behavior and the cations will have different interactions with zinc oxide nanoparticles. The use of these reagents may offer another parameter for tuning nanoparticle size. Organic bases such triethylamine or hexamethylenetetramine should also be investigated. These reagents have been shown to help direct anisotropic growth of zinc oxide nanoparticles.

The synthesis of doped metal oxide nanoparticles in the interphase droplet reactor should be investigated. The properties of metal oxide nanoparticles can be enhanced or new properties

produced through doping. The continuous synthesis of doped metal oxide nanoparticles in the interphase droplet reactor would be a useful development for many applications.

Constructing microfluidic interphase droplet reactors out of Teflon sheets should be investigated. The work presented in this demonstration has shown that PTFE is a suitable material for the interphase droplet reactor. Microfluidic channels can be constructed from Teflon sheets using hot embossing methods. Teflon microreactors may avoid the issues presented in Chapter 7, and allow the further investigation of the effects of reactor scaling on nanoparticle synthesis in an interphase droplet reactor.

References

[1] D. Agble, M.A. Mendes-Tatsis, The effect of surfactants on interfacial mass transfer in binary liquid–liquid systems, Int. J. Heat Mass Transf. 43 (2000) 1025–1034.

[2] M.R. Alenezi, S.J. Henley, N.G. Emerson, S.R.P. Silva, From 1D and 2D ZnO nanostructures to 3D hierarchical structures with enhanced gas sensing properties, Nanoscale. 6 (2014) 235–247.

[3] J.R. Anderson, D.T. Chiu, H. Wu, O.J. Schueller, G.M. Whitesides, Fabrication of microfluidic systems in poly (dimethylsiloxane), Electrophoresis. 21 (2000) 27–40.

[4] P.O. Anikeeva, J.E. Halpert, M.G. Bawendi, V. Bulović, Quantum Dot Light-Emitting Devices with Electroluminescence Tunable over the Entire Visible Spectrum, Nano Lett. 9 (2009) 2532–2536.

[5] A.I. Ayesh, Metal/Metal-Oxide Nanoclusters for Gas Sensor Applications, J. Nanomater. 2016 (2016) 1–17.

[6] T. Ban, F. Kawaizumi, S. Nii, K. Takahashi, Study of drop coalescence behavior for liquid–liquid extraction operation, Chem. Eng. Sci. 55 (2000) 5385–5391.

[7] C.N. Baroud, F. Gallaire, R. Dangla, Dynamics of microfluidic droplets, Lab. Chip. 10 (2010) 2032.

[8] P. Bénézeth, D.A. Palmer, D.J. Wesolowski, The solubility of zinc oxide in 0.03 m NaTr as a function of temperature, with in situ pH measurement, Geochim. Cosmochim. Acta. 63 (1999) 1571–1586.

[9] I. Benjamin, Polarity of the water/octanol interface, Chem. Phys. Lett. 393 (2004) 453–456.

[10] N. Bremond, A.R. Thiam, J. Bibette, Decompressing Emulsion Droplets Favors Coalescence, Phys. Rev. Lett. 100 (2008).

[11] J.R. Burns, C. Ramshaw, The intensification of rapid reactions in multiphase systems using slug flow in capillaries, Lab. Chip. 1 (2001) 10.

[12] A.-M. Cao, J.-S. Hu, H.-P. Liang, L.-J. Wan, Self-Assembled Vanadium Pentoxide (V2O5) Hollow Microspheres from Nanorods and Their Application in Lithium-Ion Batteries, Angew. Chem. Int. Ed. 44 (2005) 4391–4395.

[13] R.M. Carroll, N.R. Gupta, Inertial and surfactant effects on the steady droplet flow in cylindrical channels, Phys. Fluids. 26 (2014) 122102.

[14] W. Chamsa-ard, S. Brundavanam, C. Fung, D. Fawcett, G. Poinern, Nanofluid Types, Their Synthesis, Properties and Incorporation in Direct Solar Thermal Collectors: A Review, Nanomaterials. 7 (2017) 131.

[15] W.-C. Chang, H.-S. Chen, W.-C. Yu, Flower-shaped ZnO nanocrystallite aggregates synthesized through a template-free aqueous solution method for dye-sensitized solar cells, Appl. Phys. Lett. 106 (2015) 013908.

[16] Z. Cheng, X. Chu, J. Xu, H. Zhong, L. Zhang, Synthesis of various CuO nanostructures via a Na 3 PO 4 –assisted hydrothermal route in a CuSO 4 –NaOH aqueous system and their catalytic performances, Ceram. Int. 42 (2016) 3876–3881.

[17] J.-P. Chevaillier, E. Klaseboer, O. Masbernat, C. Gourdon, Effect of mass transfer on the film drainage between colliding drops, J. Colloid Interface Sci. 299 (2006) 472–485.

[18] S. Cho, J.-W. Jang, J.S. Lee, K.-H. Lee, Exposed Crystal Face Controlled Synthesis of 3D ZnO Superstructures, Langmuir. 26 (2010) 14255–14262.

[19] C.-H. Choi, Y.-W. Su, C. Chang, Effects of fluid flow on the growth and assembly of ZnO nanocrystals in a continuous flow microreactor, CrystEngComm. 15 (2013) 3326.

[20] Committee for Risk Assessment, Committe for Socio-economic Analysis, Background document to the Opinions on the Annex XV dossier proposing restrictions on five Phenylmercury compounds, European Chemicals Agency, n.d.
[21] A. Corma, H. Garcia, Supported gold nanoparticles as catalysts for organic reactions, Chem. Soc. Rev. 37 (2008) 2096.
[22] Y. Cudennec, A. Lecerf, The transformation of Cu(OH)2 into CuO, revisited, Solid State Sci. 5 (2003) 1471–1474.
[23] Y. Cui, N.R. Gupta, Numerical study of surfactant effects on the buoyancy-driven motion of a drop in a tube, Chem. Eng. Sci. 144 (2016) 48–57.
[24] M. De, P.S. Ghosh, V.M. Rotello, Applications of Nanoparticles in Biology, Adv. Mater. 20 (2008) 4225–4241.
[25] J. De Roo, K. De Keukeleere, Z. Hens, I. Van Driessche, From ligands to binding motifs and beyond; the enhanced versatility of nanocrystal surfaces, Dalton Trans. 45 (2016) 13277–13283.
[26] F. Demoisson, R. Piolet, F. Bernard, Hydrothermal Synthesis of ZnO Crystals from Zn(OH) $_2$ Metastable Phases at Room to Supercritical Conditions, Cryst. Growth Des. 14 (2014) 5388–5396.
[27] A.-L. Dessimoz, L. Cavin, A. Renken, L. Kiwi-Minsker, Liquid–liquid two-phase flow patterns and mass transfer characteristics in rectangular glass microreactors, Chem. Eng. Sci. 63 (2008) 4035–4044.
[28] D.K. Devendiran, V.A. Amirtham, A review on preparation, characterization, properties and applications of nanofluids, Renew. Sustain. Energy Rev. 60 (2016) 21–40.
[29] N. Di Miceli Raimondi, L. Prat, C. Gourdon, P. Cognet, Direct numerical simulations of mass transfer in square microchannels for liquid–liquid slug flow, Chem. Eng. Sci. 63 (2008) 5522–5530.
[30] N. Di Miceli Raimondi, L. Prat, C. Gourdon, J. Tasselli, Experiments of mass transfer with liquid–liquid slug flow in square microchannels, Chem. Eng. Sci. 105 (2014) 169–178.
[31] I. Dimov, S. Fidanova, I. Lirkov, eds., Numerical Methods and Applications, Springer International Publishing, Cham, 2015.
[32] K. Domansky, D.C. Leslie, J. McKinney, J.P. Fraser, J.D. Sliz, T. Hamkins-Indik, G.A. Hamilton, A. Bahinski, D.E. Ingber, Clear castable polyurethane elastomer for fabrication of microfluidic devices, Lab. Chip. 13 (2013) 3956.
[33] J.-Y. Dong, W.-H. Lin, Y.-J. Hsu, D.S.-H. Wong, S.-Y. Lu, Ultrafast formation of ZnO mesocrystals with excellent photocatalytic activities by a facile Tris-assisted antisolvent process, CrystEngComm. 13 (2011) 6218.
[34] B. Duncan, C. Kim, V.M. Rotello, Gold nanoparticle platforms as drug and biomacromolecule delivery systems, J. Controlled Release. 148 (2010) 122–127.
[35] D. Erdemir, A.Y. Lee, A.S. Myerson, Nucleation of Crystals from Solution: Classical and Two-Step Models, Acc. Chem. Res. 42 (2009) 621–629.
[36] B. Fan, Y. Zhang, R. Yan, J. Fan, Multistage growth of monocrystalline ZnO nanowires and twin-nanorods: oriented attachment and role of the spontaneous polarization force, CrystEngComm. 18 (2016) 6492–6501.
[37] G.S. Fiorini, G.D.M. Jeffries, D.S.W. Lim, C.L. Kuyper, D.T. Chiu, Fabrication of thermoset polyester microfluidic devices and embossing masters using rapid prototyped polydimethylsiloxane molds, Lab. Chip. 3 (2003) 158.

[38] G.S. Fiorini, R.M. Lorenz, J.S. Kuo, D.T. Chiu, Rapid Prototyping of Thermoset Polyester Microfluidic Devices, Anal. Chem. 76 (2004) 4697–4704.
[39] M. Fischer, D. Juric, D. Poulikakos, Large Convective Heat Transfer Enhancement in Microchannels With a Train of Coflowing Immiscible or Colloidal Droplets, J. Heat Transf. 132 (2010) 112402.
[40] K.L. Foo, M. Kashif, U. Hashim, M.E. Ali, Sol–gel derived ZnO nanoparticulate films for ultraviolet photodetector (UV) applications, Opt. - Int. J. Light Electron Opt. 124 (2013) 5373–5376.
[41] M. Fricke, A. Voigt, P. Veit, K. Sundmacher, Miniemulsion-Based Process for Controlling the Size and Shape of Zinc Oxide Nanoparticles, Ind. Eng. Chem. Res. 54 (2015) 10293–10300.
[42] P. Gabbott, Principles and Applications of Thermal Analysis, John Wiley & Sons, 2008.
[43] A. Ghaini, M.N. Kashid, D.W. Agar, Effective interfacial area for mass transfer in the liquid–liquid slug flow capillary microreactors, Chem. Eng. Process. Process Intensif. 49 (2010) 358–366.
[44] C. Girabawe, S. Fraden, An image-driven drop-on-demand system, Sens. Actuators B Chem. 238 (2017) 532–539.
[45] E.G. Goh, X. Xu, P.G. McCormick, Effect of particle size on the UV absorbance of zinc oxide nanoparticles, Scr. Mater. 78–79 (2014) 49–52.
[46] J.L. Gomez, O. Tigli, Zinc oxide nanostructures: from growth to application, J. Mater. Sci. 48 (2013) 612–624.
[47] D.P.N. Gonçalves, R.D. Rodriguez, T. Kurth, L.J. Bray, M. Binner, C. Jungnickel, F.N. Gür, S.W. Poser, T.L. Schmidt, D.R.T. Zahn, A. Androutsellis-Theotokis, M. Schlierf, C. Werner, Enhanced targeting of invasive glioblastoma cells by peptide-functionalized gold nanorods in hydrogel-based 3D cultures, Acta Biomater. 58 (2017) 12–25.
[48] M. Grad, C.C. Tsai, M. Yu, D.-L. Kwong, C.W. Wong, D. Attinger, Transient sensing of liquid films in microfluidic channels with optofluidic microresonators, Meas. Sci. Technol. 21 (2010) 075204.
[49] L.E. Greene, B.D. Yuhas, M. Law, D. Zitoun, P. Yang, Solution-Grown Zinc Oxide Nanowires, Inorg. Chem. 45 (2006) 7535–7543.
[50] Y.-B. Hahn, Zinc oxide nanostructures and their applications, Korean J. Chem. Eng. 28 (2011) 1797–1813.
[51] X. Han, Q. Kuang, M. Jin, Z. Xie, L. Zheng, Synthesis of Titania Nanosheets with a High Percentage of Exposed (001) Facets and Related Photocatalytic Properties, J. Am. Chem. Soc. 131 (2009) 3152–3153.
[52] M. Haruta, S. Tsubota, T. Kobayashi, H. Kageyama, M. Genet, B. Delmon, Low Temperature Oxidation of CO Over Gold Supported alpha-Fe2O3 and Co3O4, J. Catal. 144 (n.d.) 175–192.
[53] W. He, An insight into the Coulombic interaction in the dynamic growth of oriented-attachment nanorods, CrystEngComm. 16 (2014) 1439–1442.
[54] S. Hemmati, D.P. Barkey, L. Eggleston, B. Zukas, N. Gupta, M. Harris, Silver Nanowire Synthesis in a Continuous Millifluidic Reactor, ECS J. Solid State Sci. Technol. 6 (2017) P144–P149.
[55] H. Hillborg, U.W. Gedde, Hydrophobicity recovery of polydimethylsiloxane after exposure to corona discharges, Polymer. 39 (1998) 1991–1998.

[56] R. Hong, G. Han, J.M. Fernández, B. Kim, N.S. Forbes, V.M. Rotello, Glutathione-Mediated Delivery and Release Using Monolayer Protected Nanoparticle Carriers, J. Am. Chem. Soc. 128 (2006) 1078–1079.
[57] R.Y. Hong, J.H. Li, L.L. Chen, D.Q. Liu, H.Z. Li, Y. Zheng, J. Ding, Synthesis, surface modification and photocatalytic property of ZnO nanoparticles, Powder Technol. 189 (2009) 426–432.
[58] J.-M. Jang, S.-D. Kim, H.-M. Choi, J.-Y. Kim, W.-G. Jung, Morphology change of self-assembled ZnO 3D nanostructures with different pH in the simple hydrothermal process, Mater. Chem. Phys. 113 (2009) 389–394.
[59] C.-J. Jia, F. Schüth, Colloidal metal nanoparticles as a component of designed catalyst, Phys. Chem. Chem. Phys. 13 (2011) 2457.
[60] J.H. Jun, H. Seong, K. Cho, B.-M. Moon, S. Kim, Ultraviolet photodetectors based on ZnO nanoparticles, Ceram. Int. 35 (2009) 2797–2801.
[61] H. Kahlert, G. Meyer, A. Albrecht, Colour maps of acid–base titrations with colour indicators: how to choose the appropriate indicator and how to estimate the systematic titration errors, ChemTexts. 2 (2016).
[62] S. Kaneda, K. Ono, T. Fukuba, T. Nojima, T. Yamamoto, T. Fujii, Modification of the glass surface property in PDMS-glass hybrid microfluidic devices, Anal. Sci. 28 (2012) 39–39.
[63] Y.V. Kaneti, Z. Zhang, J. Yue, Q.M.D. Zakaria, C. Chen, X. Jiang, A. Yu, Crystal plane-dependent gas-sensing properties of zinc oxide nanostructures: experimental and theoretical studies, Phys Chem Chem Phys. 16 (2014) 11471–11480.
[64] H.W. Kang, J. Leem, S.Y. Yoon, H.J. Sung, Continuous synthesis of zinc oxide nanoparticles in a microfluidic system for photovoltaic application, Nanoscale. 6 (2014) 2840.
[65] M.N. Kashid, A. Gupta, A. Renken, L. Kiwi-Minsker, Numbering-up and mass transfer studies of liquid–liquid two-phase microstructured reactors, Chem. Eng. J. 158 (2010) 233–240.
[66] A. Kasukurti, C.D. Eggleton, S.A. Desai, D.I. Disharoon, D.W.M. Marr, A simple microfluidic dispenser for single-microparticle and cell samples, Lab Chip. 14 (2014) 4673–4679.
[67] R. Khokhra, B. Bharti, H.-N. Lee, R. Kumar, Visible and UV photo-detection in ZnO nanostructured thin films via simple tuning of solution method, Sci. Rep. 7 (2017).
[68] Y.H. Kim, L. Zhang, T. Yu, M. Jin, D. Qin, Y. Xia, Droplet-Based Microreactors for Continuous Production of Palladium Nanocrystals with Controlled Sizes and Shapes, Small. 9 (2013) 3462–3467.
[69] M. Klaumünzer, M. Distaso, J. Hübner, M. Mačković, E. Spiecker, C. Kryschi, W. Peukert, ZnO superstructures via oriented aggregation initiated in a block copolymer melt, CrystEngComm. 16 (2014) 1502–1513.
[70] A. Kołodziejczak-Radzimska, T. Jesionowski, Zinc Oxide—From Synthesis to Application: A Review, Materials. 7 (2014) 2833–2881.
[71] S. Konar, H. Kalita, N. Puvvada, S. Tantubay, M.K. Mahto, S. Biswas, A. Pathak, Shape-dependent catalytic activity of CuO nanostructures, J. Catal. 336 (2016) 11–22.
[72] J.G. Kralj, M.A. Schmidt, K.F. Jensen, Surfactant-enhanced liquid–liquid extraction in microfluidic channels with inline electric-field enhanced coalescence, Lab. Chip. 5 (2005) 531.

[73] A. Kubacka, M. Fernández-García, G. Colón, Advanced Nanoarchitectures for Solar Photocatalytic Applications, Chem. Rev. 112 (2012) 1555–1614.
[74] A.A. Kulkarni, V. Sebastian Cabeza, Insights in the Diffusion Controlled Interfacial Flow Synthesis of Au Nanostructures in a Microfluidic System, Langmuir. 33 (2017) 14315–14324.
[75] N. Kumar, H. Mittal, L. Reddy, P. Nair, J.C. Ngila, V. Parashar, Morphogenesis of ZnO nanostructures: role of acetate ($COOH^-$) and nitrate (NO_3^-) ligand donors from zinc salt precursors in synthesis and morphology dependent photocatalytic properties, RSC Adv. 5 (2015) 38801–38809.
[76] C.A. Launiere, A.V. Gelis, High Precision Droplet-Based Microfluidic Determination of Americium(III) and Lanthanide(III) Solvent Extraction Separation Kinetics, Ind. Eng. Chem. Res. 55 (2016) 2272–2276.
[77] Y.-L. Lee, Surfactants effects on mass transfer during drop-formation and drop falling stages, AIChE J. 49 (2003) 1859–1869.
[78] L. Li, J.Q. Boedicker, R.F. Ismagilov, Using a Multijunction Microfluidic Device To Inject Substrate into an Array of Preformed Plugs without Cross-Contamination: Comparing Theory and Experiments, Anal. Chem. 79 (2007) 2756–2761.
[79] P. Li, B. Lu, Z. Luo, Hydrothermal growth of wheatear-shaped ZnO microstructures and their photocatalytic activity, Bull. Mater. Sci. 40 (2017) 1069–1074.
[80] S. Li, G.A. Gross, P.M. Günther, J.M. Köhler, Hydrothermal micro continuous-flow synthesis of spherical, cylinder-, star- and flower-like ZnO microparticles, Chem. Eng. J. 167 (2011) 681–687.
[81] S. Li, S. Meierott, J.M. Köhler, Effect of water content on growth and optical properties of ZnO nanoparticles generated in binary solvent mixtures by micro-continuous flow synthesis, Chem. Eng. J. 165 (2010) 958–965.
[82] S. Li, J. Xu, Y. Wang, G. Luo, Controllable Preparation of Nanoparticles by Drops and Plugs Flow in a Microchannel Device, Langmuir. 24 (2008) 4194–4199.
[83] T. Li, Z. Cao, H. You, M. Xu, X. Song, J. Fang, Controllable growth of ZnO mesocrystals using a facile electrochemical approach, Chem. Phys. Lett. 555 (2013) 154–158.
[84] Y. Li, E. Boone, M.A. El-Sayed, Size effects of PVP- Pd nanoparticles on the catalytic Suzuki reactions in aqueous solution, Langmuir. 18 (2002) 4921–4925.
[85] C.-F. Lin, P.-F. Chung, M.-J. Chen, W.-F. Su, Nanoparticle-modified metal–oxide–silicon structure enhancing silicon band-edge electroluminescence to near-lasing action, Opt. Lett. 27 (2002) 713–715.
[86] Linear Technology Corporation, LTC 1050 Precision Zero Drift Operational Amplifier with Internal Capacitors, (1991).
[87] J. Liu, X. Huang, Y. Li, Q. Zhong, L. Ren, Preparation and photoluminescence of ZnO complex structures with controlled morphology, Mater. Lett. 60 (2006) 1354–1359.
[88] J. Liu, X. Huang, K.M. Sulieman, F. Sun, X. He, Solution-Based Growth and Optical Properties of Self-Assembled Monocrystalline ZnO Ellipsoids, J. Phys. Chem. B. 110 (2006) 10612–10618.
[89] F.I. Lizama-Tzec, R. García-Rodríguez, G. Rodríguez-Gattorno, E.J. Canto-Aguilar, A.G. Vega-Poot, B.E. Heredia-Cervera, J. Villanueva-Cab, N. Morales-Flores, U. Pal, G. Oskam, Influence of morphology on the performance of ZnO-based dye-sensitized solar cells, RSC Adv. 6 (2016) 37424–37433.

[90] S.E. Lohse, J.R. Eller, S.T. Sivapalan, M.R. Plews, C.J. Murphy, A Simple Millifluidic Benchtop Reactor System for the High-Throughput Synthesis and Functionalization of Gold Nanoparticles with Different Sizes and Shapes, ACS Nano. 7 (2013) 4135–4150.
[91] N. Lorber, F. Sarrazin, P. Guillot, P. Panizza, A. Colin, B. Pavageau, C. Hany, P. Maestro, S. Marre, T. Delclos, C. Aymonier, P. Subra, L. Prat, C. Gourdon, E. Mignard, Some recent advances in the design and the use of miniaturized droplet-based continuous process: Applications in chemistry and high-pressure microflows, Lab Chip. 11 (2011) 779–787.
[92] C.-H. Lu, C.-H. Yeh, Emulsion precipitation of submicron zinc oxide powder, Mater. Lett. 33 (1997) 129–132.
[93] B. Ludi, M. Niederberger, Zinc oxide nanoparticles: chemical mechanisms and classical and non-classical crystallization, Dalton Trans. 42 (2013) 12554.
[94] M.-G. Ma, H. Cölfen, Mesocrystals — Applications and potential, Curr. Opin. Colloid Interface Sci. 19 (2014) 56–65.
[95] N. MacCallum, C. Howell, P. Kim, D. Sun, R. Friedlander, J. Ranisau, O. Ahanotu, J.J. Lin, A. Vena, B. Hatton, T.-S. Wong, J. Aizenberg, Liquid-Infused Silicone As a Biofouling-Free Medical Material, ACS Biomater. Sci. Eng. 1 (2015) 43–51.
[96] S. Marre, K.F. Jensen, Synthesis of micro and nanostructures in microfluidic systems, Chem. Soc. Rev. 39 (2010) 1183.
[97] D.E. Mathison, B. Yates, M.I. Darby, Absorption of silicone fluid in a silicone elastomer, J. Mater. Sci. 26 (1991) 6–10.
[98] R.A. McBride, J.M. Kelly, D.E. McCormack, Growth of well-defined ZnO microparticles by hydroxide ion hydrolysis of zinc salts, J. Mater. Chem. 13 (2003) 1196–1201.
[99] B.K. Meyer, A. Polity, D. Reppin, M. Becker, P. Hering, P.J. Klar, T. Sander, C. Reindl, J. Benz, M. Eickhoff, C. Heiliger, M. Heinemann, J. Bläsing, A. Krost, S. Shokovets, C. Müller, C. Ronning, Binary copper oxide semiconductors: From materials towards devices, Phys. Status Solidi B. 249 (2012) 1487–1509.
[100] T. Milek, D. Zahn, Molecular modeling of $(10\bar{1}0)$ and $(000\bar{1})$ zinc oxide surface growth from solution: islands, ridges and growth-controlling additives, CrystEngComm. 17 (2015) 6890–6894.
[101] A. Moezzi, M. Cortie, A. McDonagh, Aqueous pathways for the formation of zinc oxide nanoparticles, Dalton Trans. 40 (2011) 4871.
[102] A. Moezzi, A.M. McDonagh, M.B. Cortie, Zinc oxide particles: Synthesis, properties and applications, Chem. Eng. J. 185–186 (2012) 1–22.
[103] M. Musterd, V. van Steijn, C.R. Kleijn, M.T. Kreutzer, Calculating the volume of elongated bubbles and droplets in microchannels from a top view image, RSC Adv. 5 (2015) 16042–16049.
[104] T.-D. Nguyen, From formation mechanisms to synthetic methods toward shape-controlled oxide nanoparticles, Nanoscale. 5 (2013) 9455.
[105] M. Niederberger, H. Cölfen, Oriented attachment and mesocrystals: Non-classical crystallization mechanisms based on nanoparticle assembly, Phys Chem Chem Phys. 8 (2006) 3271–3287.
[106] A.M. Nightingale, J.C. deMello, Segmented Flow Reactors for Nanocrystal Synthesis, Adv. Mater. 25 (2013) 1813–1821.
[107] A.M. Nightingale, S.H. Krishnadasan, D. Berhanu, X. Niu, C. Drury, R. McIntyre, E. Valsami-Jones, J.C. deMello, A stable droplet reactor for high temperature nanocrystal synthesis, Lab Chip. 11 (2011) 1221–1227.

[108] G. Niu, A. Ruditskiy, M. Vara, Y. Xia, Toward continuous and scalable production of colloidal nanocrystals by switching from batch to droplet reactors, Chem Soc Rev. 44 (2015) 5806–5820.
[109] A.P.A. Oliveira, J.-F. Hochepied, F. Grillon, M.-H. Berger, Controlled Precipitation of Zinc Oxide Particles at Room Temperature, Chem. Mater. 15 (2003) 3202–3207.
[110] B. Palmer, L. DeLouise, Nanoparticle-Enabled Transdermal Drug Delivery Systems for Enhanced Dose Control and Tissue Targeting, Molecules. 21 (2016) 1719.
[111] L.-J. Pan, J.-W. Tu, H.-T. Ma, Y.-J. Yang, Z.-Q. Tian, D.-W. Pang, Z.-L. Zhang, Controllable synthesis of nanocrystals in droplet reactors, Lab. Chip. 18 (2018) 41–56.
[112] Y. Pan, J. Yao, L. Zhang, N. Xu, Preparation of Ultrafine Zeolite A Crystals with Narrow Particle Size Distribution Using a Two-Phase Liquid Segmented Microfluidic Reactor, Ind. Eng. Chem. Res. 48 (2009) 8471–8477.
[113] N. Paul, M. Kraume, S. Schön, R. von Klitzing, Transport processes at single droplets in micellar liquid/liquid systems, AIChE J. 61 (2015) 1092–1104.
[114] N. Paul, P. Schrader, S. Enders, M. Kraume, Effects of phase behaviour on mass transfer in micellar liquid/liquid systems, Chem. Eng. Sci. 115 (2014) 148–156.
[115] N. Paul, J.M. Schulz, M. Kraume, Fluid Dynamics of Droplets as a Useful Tool to Determine Coverage and Adsorption Kinetics of Surfactants, Chem. Eng. Technol. 38 (2015) 1979–1984.
[116] T.W. Phillips, I.G. Lignos, R.M. Maceiczyk, A.J. deMello, J.C. deMello, Nanocrystal synthesis in microfluidic reactors: where next?, Lab. Chip. 14 (2014) 3172.
[117] A.M. Pourrahimi, D. Liu, R.L. Andersson, V. Ström, U.W. Gedde, R.T. Olsson, Aqueous Synthesis of $(2\bar{1}0)$ Oxygen-Terminated Defect-Free Hierarchical ZnO Particles and Their Heat Treatment for Enhanced Reactivity, Langmuir. 32 (2016) 11002–11013.
[118] A.M. Pourrahimi, D. Liu, L.K.H. Pallon, R.L. Andersson, A. Martínez Abad, J.-M. Lagarón, M.S. Hedenqvist, V. Ström, U.W. Gedde, R.T. Olsson, Water-based synthesis and cleaning methods for high purity ZnO nanoparticles – comparing acetate, chloride, sulphate and nitrate zinc salt precursors, RSC Adv. 4 (2014) 35568.
[119] X. Pu, G. Li, Y. Song, M. Shang, Y. Su, Droplet Coalescence Phenomena during Liquid–Liquid Heterogeneous Reactions in Microreactors, Ind. Eng. Chem. Res. 56 (2017) 12316–12325.
[120] X. Pu, D. Zhang, X. Yi, X. Shao, W. Li, M. Sun, L. Li, X. Qian, Rapid chemical synthesis and optical properties of ZnO ellipsoidal nanostructures, Adv. Powder Technol. 21 (2010) 344–349.
[121] K. Pushpanathan, S. Sathya, M.J. Chithra, S. Gowthami, R. Santhi, Influence of Reaction Temperature on Crystal Structure and Band Gap of ZnO Nanoparticles, Mater. Manuf. Process. 27 (2012) 1334–1342.
[122] A. Ratkovich, R.L. Penn, Zinc oxide nanoparticle growth from homogenous solution: Influence of Zn:OH, water concentration, and surfactant additives, Mater. Res. Bull. 44 (2009) 993–998.
[123] E. Redel, P. Mirtchev, C. Huai, S. Petrov, G.A. Ozin, Nanoparticle Films and Photonic Crystal Multilayers from Colloidally Stable, Size-Controllable Zinc and Iron Oxide Nanoparticles, ACS Nano. 5 (2011) 2861–2869.
[124] B. Riechers, F. Maes, E. Akoury, B. Semin, P. Gruner, J.-C. Baret, Surfactant adsorption kinetics in microfluidics, Proc. Natl. Acad. Sci. 113 (2016) 11465–11470.

[125] J. Saien, S. Akbari, Interfacial Tension of Toluene + Water + Sodium Dodecyl Sulfate from (20 to 50) °C and pH between 4 and 9, J. Chem. Eng. Data. 51 (2006) 1832–1835.
[126] J. Saien, S. Akbari, Interfacial Tension of Hydrocarbon + Different pH Aqueous phase Systems in the Presence of Triton X-100, Ind. Eng. Chem. Res. 49 (2010) 3228–3235.
[127] J. Saien, S. Daliri, Mass Transfer Coefficient in Liquid−Liquid Extraction and the Influence of Aqueous Phase pH, Ind. Eng. Chem. Res. 47 (2008) 171–175.
[128] J. Saien, S. Rezabeigy, Alternative Influence of Binary Surfactant Mixtures on the Rate of Mass Transfer in a Liquid–Liquid Extraction Process, Ind. Eng. Chem. Res. 50 (2011) 6925–6932.
[129] S. Sakthivel, B. Neppolian, M.V. Shankar, B. Arabindoo, M. Palanichamy, V. Murugesan, Solar photocatalytic degradation of azo dye: comparison of photocatalytic efficiency of ZnO and TiO 2, Sol. Energy Mater. Sol. Cells. 77 (2003) 65–82.
[130] N. Samaele, P. Amornpitoksuk, S. Suwanboon, Effect of pH on the morphology and optical properties of modified ZnO particles by SDS via a precipitation method, Powder Technol. 203 (2010) 243–247.
[131] F. Sarrazin, T. Bonometti, L. Prat, C. Gourdon, J. Magnaudet, Hydrodynamic structures of droplets engineered in rectangular micro-channels, Microfluid. Nanofluidics. 5 (2008) 131–137.
[132] M. Sattari-Najafabadi, M.N. Nasr Esfahany, Intensification of liquid-liquid mass transfer in a circular microchannel in the presence of sodium dodecyl sulfate, Chem. Eng. Process. Process Intensif. 117 (2017) 9–17.
[133] A. Schejn, M. Fregnaux, J.-M. Commenge, L. Balan, L. Falk, R. Schneider, Size Controlled synthesis of ZnO quantum dots in microreactors, Nanotechnology. 25 (2014) 145606.
[134] D. Segets, R. Marczak, S. Schäfer, C. Paula, J.-F. Gnichwitz, A. Hirsch, W. Peukert, Experimental and Theoretical Studies of the Colloidal Stability of Nanoparticles−A General Interpretation Based on Stability Maps, ACS Nano. 5 (2011) 4658–4669.
[135] P. Selvakumar, S. Suresh, Convective performance of CuO/water nanofluid in an electronic heat sink, Exp. Therm. Fluid Sci. 40 (2012) 57–63.
[136] A. Shafaei, M. Nikazar, M. Arami, Photocatalytic degradation of terephthalic acid using titania and zinc oxide photocatalysts: Comparative study, Desalination. 252 (2010) 8–16.
[137] J. Shi, Y. Liu, Q. Peng, Y. Li, ZnO hierarchical aggregates: Solvothermal synthesis and application in dye-sensitized solar cells, Nano Res. 6 (2013) 441–448.
[138] B. Singh, S. Singh, J. Singh, G.S.S. Saini, D.S. Mehta, G. Singh, S.K. Tripathi, A. Kaura, Understanding the adsorption behavior of surface active molecules on ZnO nanostructures by experimental and first-principles calculations, Phys. Chem. Chem. Phys. 17 (2015) 30450–30460.
[139] J. Sivasamy, Y.C. Chim, T.-N. Wong, N.-T. Nguyen, L. Yobas, Reliable addition of reagents into microfluidic droplets, Microfluid. Nanofluidics. 8 (2010) 409–416.
[140] M. Søndergaard, E.D. Bøjesen, M. Christensen, B.B. Iversen, Size and Morphology Dependence of ZnO Nanoparticles Synthesized by a Fast Continuous Flow Hydrothermal Method, Cryst. Growth Des. 11 (2011) 4027–4033.
[141] H. Song, J.D. Tice, R.F. Ismagilov, A microfluidic system for controlling reaction networks in time, Angew. Chem. 115 (2003) 792–796.
[142] L. Spanhel, Colloidal ZnO nanostructures and functional coatings: A survey, J. Sol-Gel Sci. Technol. 39 (2006) 7–24.

[143] W.J. Stark, P.R. Stoessel, W. Wohlleben, A. Hafner, Industrial applications of nanoparticles, Chem. Soc. Rev. 44 (2015) 5793–5805.
[144] S. Sun, X. Zhang, J. Zhang, X. Song, Z. Yang, Unusual Designated-Tailoring on Zone-Axis Preferential Growth of Surfactant-Free ZnO Mesocrystals, Cryst. Growth Des. 12 (2012) 2411–2418.
[145] S. Sun, X. Zhang, J. Zhang, L. Wang, X. Song, Z. Yang, Surfactant-free CuO mesocrystals with controllable dimensions: green ordered-aggregation-driven synthesis, formation mechanism and their photochemical performances, CrystEngComm. 15 (2013) 867–877.
[146] Y. Sun, L. Wang, X. Yu, K. Chen, Facile synthesis of flower-like 3D ZnO superstructures via solution route, CrystEngComm. 14 (2012) 3199.
[147] S. Suresh, K.P. Venkitaraj, P. Selvakumar, M. Chandrasekar, A comparison of thermal characteristics of Al2O3/water and CuO/water nanofluids in transition flow through a straight circular duct fitted with helical screw tape inserts, Exp. Therm. Fluid Sci. 39 (2012) 37–44.
[148] M. Takagi, T. Maki, M. Miyahara, K. Mae, Production of titania nanoparticles by using a new microreactor assembled with same axle dual pipe, Chem. Eng. J. 101 (2004) 269–276.
[149] D.V. Talapin, J.-S. Lee, M.V. Kovalenko, E.V. Shevchenko, Prospects of Colloidal Nanocrystals for Electronic and Optoelectronic Applications, Chem. Rev. 110 (2010) 389–458.
[150] W. Tanthapanichakoon, N. Aoki, K. Matsuyama, K. Mae, Design of mixing in microfluidic liquid slugs based on a new dimensionless number for precise reaction and mixing operations, Chem. Eng. Sci. 61 (2006) 4220–4232.
[151] N.T.K. Thanh, N. Maclean, S. Mahiddine, Mechanisms of Nucleation and Growth of Nanoparticles in Solution, Chem. Rev. 114 (2014) 7610–7630.
[152] J.D. Tice, H. Song, A.D. Lyon, R.F. Ismagilov, Formation of Droplets and Mixing in Multiphase Microfluidics at Low Values of the Reynolds and the Capillary Numbers, Langmuir. 19 (2003) 9127–9133.
[153] J.D. Tice, H. Song, A.D. Lyon, R.F. Ismagilov, Formation of Droplets and Mixing in Multiphase Microfluidics at Low Values of the Reynolds and the Capillary Numbers, Langmuir. 19 (2003) 9127–9133.
[154] A. Top, H. Çetinkaya, Zinc oxide and zinc hydroxide formation via aqueous precipitation: Effect of the preparation route and lysozyme addition, Mater. Chem. Phys. 167 (2015) 77–87.
[155] V. Trivedi, A. Doshi, G.K. Kurup, E. Ereifej, P.J. Vandevord, A.S. Basu, A modular approach for the generation, storage, mixing, and detection of droplet libraries for high throughput screening, Lab. Chip. 10 (2010) 2433.
[156] D. Tsaoulidis, P. Angeli, Effect of channel size on mass transfer during liquid–liquid plug flow in small scale extractors, Chem. Eng. J. 262 (2015) 785–793.
[157] C. Tsouris, L.L. Tavlarides, Mass-transfer effects on droplet phenomena and extraction column hydrodynamics revisited, Chem. Eng. Sci. 48 (1993) 1503–1515.
[158] E. Uchaker, G. Cao, Mesocrystals as electrode materials for lithium-ion batteries, Nano Today. 9 (2014) 499–524.
[159] S. Ueno, S. Fujihara, Controlled synthesis of star-shaped zinc oxide particles at low temperatures and their quantum size effect, J. Alloys Compd. 541 (2012) 338–345.
[160] P. Urbant, A. Leshansky, Y. Halupovich, On the forced convective heat transport in a droplet-laden flow in microchannels, Microfluid. Nanofluidics. 4 (2008) 533–542.

[161] H. Usui, The effect of surfactants on the morphology and optical properties of precipitated wurtzite ZnO, Mater. Lett. 63 (2009) 1489–1492.
[162] H. Usui, Surfactant concentration dependence of structure and photocatalytic properties of zinc oxide rods prepared using chemical synthesis in aqueous solutions, J. Colloid Interface Sci. 336 (2009) 667–674.
[163] M.A. Vergés, A. Mifsud, C.J. Serna, Formation of rod-like zinc oxide microcrystals in homogeneous solutions, J. Chem. Soc. Faraday Trans. 86 (1990) 959–963.
[164] F. Vidor, T. Meyers, U. Hilleringmann, Inverter Circuits Using ZnO Nanoparticle Based Thin-Film Transistors for Flexible Electronic Applications, Nanomaterials. 6 (2016) 154.
[165] S.A. Vorobyova, A.I. Lesnikovich, V.V. Mushinskii, Interphase synthesis and characterization of zinc oxide, Mater. Lett. 58 (2004) 863–866.
[166] R. Wahab, S.G. Ansari, Y.S. Kim, M. Song, H.-S. Shin, The role of pH variation on the growth of zinc oxide nanostructures, Appl. Surf. Sci. 255 (2009) 4891–4896.
[167] J. Wang, M. Zheng, W. Wang, Z. Li, Optimal protocol for moulding PDMS with a PDMS master, Chips Tips. (2010).
[168] M. Wang, Y. Zhang, Y. Zhou, F. Yang, E.J. Kim, S.H. Hahn, S.G. Seong, Rapid room-temperature synthesis of nanosheet-assembled ZnO mesocrystals with excellent photocatalytic activity, CrystEngComm. 15 (2013) 754–763.
[169] Y. Wang, J. He, C. Liu, W.H. Chong, H. Chen, Thermodynamics versus Kinetics in Nanosynthesis, Angew. Chem. Int. Ed. 54 (2015) 2022–2051.
[170] M. Wegener, A.R. Paschedag, The effect of soluble anionic surfactants on rise velocity and mass transfer at single droplets in systems with Marangoni instabilities, Int. J. Heat Mass Transf. 55 (2012) 1561–1573.
[171] C.D. Wick, T.-M. Chang, Computational Observation of Pockets of Enhanced Water Concentration at the 1-Octanol/Water Interface, J. Phys. Chem. B. 118 (2014) 7785–7791.
[172] M. Winkelmann, E.-M. Grimm, T. Comunian, B. Freudig, Y. Zhou, W. Gerlinger, B. Sachweh, H. Petra Schuchmann, Controlled droplet coalescence in miniemulsions to synthesize zinc oxide nanoparticles by precipitation, Chem. Eng. Sci. 92 (2013) 126–133.
[173] R. Xie, D. Li, H. Zhang, D. Yang, M. Jiang, T. Sekiguchi, B. Liu, Y. Bando, Low-Temperature Growth of Uniform ZnO Particles with Controllable Ellipsoidal Morphologies and Characteristic Luminescence Patterns, J. Phys. Chem. B. 110 (2006) 19147–19153.
[174] C. Xu, T. Xie, Review of Microfluidic Liquid–Liquid Extractors, Ind. Eng. Chem. Res. 56 (2017) 7593–7622.
[175] J.H. Xu, J. Tan, S.W. Li, G.S. Luo, Enhancement of mass transfer performance of liquid–liquid system by droplet flow in microchannels, Chem. Eng. J. 141 (2008) 242–249.
[176] M. Xu, F. Wang, B. Ding, X. Song, J. Fang, Electrochemical synthesis of leaf-like CuO mesocrystals and their lithium storage properties, RSC Adv. 2 (2012) 2240.
[177] X. Xu, H. Pang, Z. Zhou, X. Fan, S. Hu, Y. Wang, Preparation of multi-interfacial ZnO particles and their growth mechanism, Adv. Powder Technol. 22 (2011) 634–638.
[178] X. Xu, H. Yang, Y. Liu, Self-assembled structures of CuO primary crystals synthesized from Cu(CH3COO)2–NaOH aqueous systems, CrystEngComm. 14 (2012) 5289.
[179] Y. Xu, J. Jin, X. Li, Y. Han, H. Meng, T. Wang, X. Zhang, Simple synthesis of ZnO nanoflowers and its photocatalytic performances toward the photodegradation of metamitron, Mater. Res. Bull. 76 (2016) 235–239.

[180] C. Yang, F. Xiao, J. Wang, X. Su, 3D flower- and 2D sheet-like CuO nanostructures: Microwave-assisted synthesis and application in gas sensors, Sens. Actuators B Chem. 207 (2015) 177–185.
[181] L. Yu, Y. Pan, C. Wang, L. Zhang, A two-phase segmented microfluidic technique for one-step continuous versatile preparation of zeolites, Chem. Eng. J. 219 (2013) 78–85.
[182] Q. Yu, C. Yu, W. Fu, M. Yuan, J. Guo, M. Li, S. Liu, G. Zou, H. Yang, Synthesis, Optical Properties, and Ethanol-Sensing Properties of Bicone-like ZnO Microcrystals via a Simple Solution Method, J. Phys. Chem. C. 113 (2009) 12016–12021.
[183] J. Zhang, Y. Cui, Q. Qin, G. Zhang, W. Luo, W. Zheng, Nanoporous CuO mesocrystals: Low-temperature synthesis and improved structure-performance relationship for energy storage system, Chem. Eng. J. 331 (2018) 326–334.
[184] L. Zhang, Y. Wang, L. Tong, Y. Xia, Synthesis of Colloidal Metal Nanocrystals in Droplet Reactors: The Pros and Cons of Interfacial Adsorption, Nano Lett. 14 (2014) 4189–4194.
[185] Y. Zhang, J. Mu, Controllable synthesis of flower- and rod-like ZnO nanostructures by simply tuning the ratio of sodium hydroxide to zinc acetate, Nanotechnology. 18 (2007) 075606.
[186] Z. Zhang, H. Sun, X. Shao, D. Li, H. Yu, M. Han, Three-Dimensionally Oriented Aggregation of a Few Hundred Nanoparticles into Monocrystalline Architectures, Adv. Mater. 17 (2005) 42–47.
[187] C.-X. Zhao, L. He, S.Z. Qiao, A.P.J. Middelberg, Nanoparticle synthesis in microreactors, Chem. Eng. Sci. 66 (2011) 1463–1479.
[188] C.-X. Zhao, A.P.J. Middelberg, Two-phase microfluidic flows, Chem. Eng. Sci. 66 (2011) 1394–1411.
[189] S. Zhao, B. You, L. Jiang, Oriented Assembly of Zinc Oxide Mesocrystal in Chitosan and Applications for Glucose Biosensors, Cryst. Growth Des. 16 (2016) 3359–3365.
[190] W. Zheng, X. Li, G. He, X. Yan, R. Zhao, C. Dong, A highly responsive UV photodetector based on hierarchical TiO $_2$ nanorod/nanoparticle composite, RSC Adv. 4 (2014) 21340–21346.
[191] J. Zhu, D. Li, H. Chen, X. Yang, L. Lu, X. Wang, Highly dispersed CuO nanoparticles prepared by a novel quick-precipitation method, Mater. Lett. 58 (2004) 3324–3327.
[192] B.G. Zukas, N.R. Gupta, Interphase Synthesis of Zinc Oxide Nanoparticles in a Droplet Flow Reactor, Ind. Eng. Chem. Res. 56 (2017) 7184–7191.
[193] Processing Guidlines for SU-8 2100 and SU-8 2150, (n.d.).